UNIVERSITY OF OKLAHOMA
GRADUATE COLLEGE

EVOLUTION OF CHARGE AND LIGHTNING THROUGHOUT AN OBSERVED AND SIMULATED SUPERCELL STORM

A DISSERTATION
SUBMITTED TO THE GRADUATE FACULTY
in partial fulfillment of the requirements for the
Degree of
DOCTOR OF PHILOSOPHY

By

KRISTIN MARIE KUHLMAN
Norman, Oklahoma
2010

EVOLUTION OF CHARGE AND LIGHTNING THROUGHOUT AN OBSERVED AND SIMULATED SUPERCELL STORM

A DISSERTATION APPROVED FOR THE
SCHOOL OF METEOROLOGY

By

Dr. Donald R. MacGorman

Dr. Michael Biggerstaff

Dr. William H. Beasley

Dr. David Dowell

Dr. Stewart Ryan

Dr. Jerry M. Straka

Acknowledgements

I do not believe anyone completes a scientific dissertation locked alone in an office (or a dungeon), it is culmination of multiple years of work with collaborations alongside multiple scientists and faculty members. First of all, I must thank and acknowledge my advisor, Dr. Donald MacGorman. I have learned a great deal working with him, not only about the scientific process and storm electrification, but also how to become a better scientific writer. He has patiently worked with me these many years, from the data collection during TELEX in 2003 and 2004 through the writing of this dissertation and associated publications.

I also want to thank Dr. David Dowell, who provided the inspiration for this work during a presentation at the AMS Severe Local Storms Conference in Hyannis, MA in October 2004. He worked with me early on to better understand and complete the data assimilation process; without David's help, I'm not sure I could have even begun the project. Along those same lines, I have been lucky enough to work Dr. Ted Mansell since the beginning of my Masters degree. He has answered countless questions I've had about his electrification and lightning parameterizations and quickly fixed things I may have broken in the code. My masters' advisor, Dr. Conrad Ziegler, has continued to support my work and provide detailed feedback–particularly with the dual-Doppler analyses in this dissertation. His keen eye has allowed me to be a better communicator of my results, specifically within my figures.

My committee chair, Dr. Michael Biggerstaff, provided the SMART-radar data from 29 May 2004; I would have had to complete a very different project without it. Dr. Biggerstaff and Dan Betten also provided feedback and suggestions during that tedious radar editing process. Those members serving on my committee, Drs. W. Beasley, J. Straka, and S. Ryan, have shown continued patience through the years as I have kept changing the date of my defense. I am extremely grateful they have stayed with me and for the feedback they have provided along the way.

During the last two years of this work, I have maintained a job with CIMMS in the Warning Research Division of NSSL and I work with a great group of people. In particular, Travis Smith has been a joy to work for and I am grateful for his support as I've continued this research and writing the dissertation.

Friends and significant others have not only listened to me question, complain and just talk through my work for the last 6 (cough) years, but have also helped provide solutions when I needed them most. They have been vital to my sanity and my progress. In particular I need to thank: Stephanie Weiss, who is always available to give me a sanity check and be there with an sympathetic ear; Eric Bruning, who has provided numerous scripts and know-how from day 1 in the field with TELEX; and Patrick Calhoun, who continues to be endlessly patient on a daily basis, gets me through computer errors and scripts that have me befuddled, and most importantly, provides me with love and understanding.

Of course, ultimately it is my parents who have helped me become the person I am today, and it is their support that helped carry me as I pushed my way through this. Though I'm sure they would be proud whether I completed a Ph.D. or became an oceanside bar owner in the Bahamas, I am certain they are quite glad I have finally completed this dissertation.

Finally, this work was supported for by the National Science Foundation, Grant ATM-0233268. Also, this dissertation was typeset with LaTeX by the author using the OU dissertation package developed by Dr. Brian Fiedler–this has made my life a hell of a lot easier than trying to write something like this in MS Word.

Contents

List Of Tables

List Of Figures

Abstract

A high-precipitation tornadic supercell storm was observed by multiple platforms on 29 May 2004 during the Thunderstorm Electrification and Lightning Experiment (TELEX). Observational systems included the Oklahoma Lightning Mapping Array (LMA), mobile balloon-borne soundings, and two mobile SMART-R (SR) C-Band radars. This dissertation utilizes data from these platforms to relate the spatial distribution and evolution of lightning to storm kinematics and microphysics, especially to regions of microphysical charging and the location and geometry of those charge regions. One example is the relationship of the observed transient lightning hole and of large lightning densities to kinematic properties inferred from dual-Doppler analyses of the SR data.

The lightning flashes near the core of this storm, although extraordinarily frequent, tended to have shorter duration and smaller horizontal extent than typical flashes in other storms having less frequent lightning. This is due, at least in part, to many small pockets of charge lying in close proximity to small pockets of the opposite polarity of charge. Thus, each polarity of lightning leader propagates only a relatively short distance before reaching regions of unfavorable electrical potential. In the anvil, however, lightning extended tens of kilometers from the reflectivity cores in roughly horizontal layers, consistent with the charge spreading through the anvil in broad sheets.

Previous studies of lightning in anvil clouds have reported that flashes began in or near the storm core and propagated downwind into the anvil, and many flashes followed that pattern in this storm. However, this dissertation presents the first observations of flashes that began in the anvil 30-100 km from the cores of the storms and propagated upwind back toward the cores. It had been thought that flashes could not be initiated far downwind in the anvil, because anvil charge was thought to be produced mainly in the storm's deep updraft and to decrease with distance into the anvil. Interaction between charge regions in the two converging anvils of adjoining storms appeared to cause some of the distant flash initiations, but a local charging mechanism in the anvil likely also contributed to the flash initiations.

The observations cited above are compared with results from simulations using the Collaborative Model for Multiscale Atmospheric Simulation (COMMAS) with two-moment microphysics, seven hydrometeor categories, and parameterizations for electrification and lightning and employing an ensemble Kalman filter for mobile radar data assimilation. The simulated precipitation and wind fields were similar to those of the observed storm. Simulated lightning flash rates were very large, as was observed, and the distribution of charge in the main body of the storm revealed in the simulation details the lightning dependence on storm kinematics that could not be directly observed. The simulation produced observed lightning holes and the high-altitude lightning seen in the observations. However, the simulation failed to produce the observed lightning initiations (or even lightning channels) in the distant downstream anvil; instead, the simulated lightning was confined to the main body of the storm.

Chapter 1

Introduction

Storm electrification and lightning are intimately linked to storm kinematics, microphysics, and dynamics. The Thunderstorm Electrification and Lightning Experiment (TELEX) was established in central Oklahoma to further the understanding those relationships (MacGorman et al. 2008b). On 29 May 2004, a line of convective cells formed along a dryline near Elk City, OK; one intensified to a heavy-precipitation (HP) supercell (Doswell and Burgess 1993; Moller et al. 1994) north of Weatherford, OK as it moved into the TELEX domain. The data set established through this field campaign allows for a comprehensive study of this HP supercell, and, in fact, this is one of the first HP supercells ever observed by the OK Lightning Mapping Array (LMA). In addition to the LMA, the storm was observed by two C-band mobile radars providing rapid, high resolution volume scans, two S-band WSR-88D radars (including one with polarimetric capabilites), the National Lightning Detection Network (NLDN), and balloon-borne electric-field-meter soundings through the storm. (Fig. 1.1 contains a timeline of the observations of this storm). These observational platforms documented the storm for over three hours, capturing the mature stage of the storm, including two F2 tornadoes near Geary, OK.

This storm exhibited a variety of lightning behaviors related to supercell storm characteristics. Some of these behaviors, such as lightning holes just above the bounded weak echo region and a reversal of in the dominant polarity of ground flashes in the storm core, are similar to behaviors that have been documented in other supercell storms (e.g., Wiens et al. 2005; MacGorman et al. 2005; Curran and Rust 1992). Other behaviors, such as initiation of negative ground flashes tens of kilometers away from the core of the storm in the downshear anvil, are unusual, even for supercell storms. The comprehensive data set available for this storm will enable the documentation of the relationship of these lightning behaviors to other storm characteristics and, therefore, provide the ability to test and revise hypotheses that have been offered to explain some of the lightning behaviors.

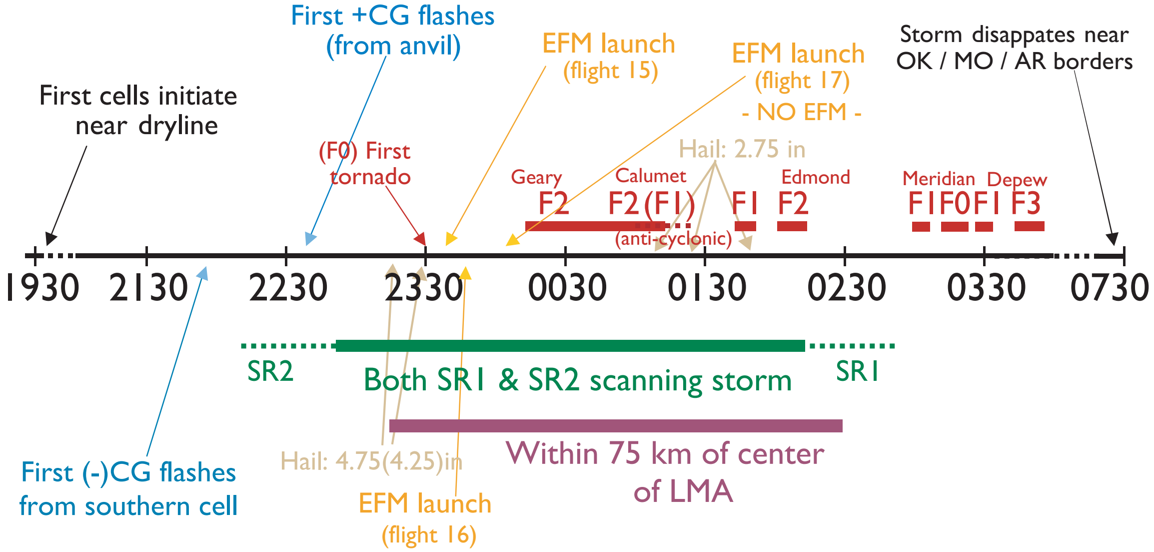

Figure 1.1: Timing of storm evolution and observational networks on 29 May 2004.

1.1 Motivation for this research

The data set provided by the TELEX field experiment for the 29 May 2004 storm provides a unique opportunity to study relationships of lightning and electrification to other storm properties in more detail than previously possible for a tornadic HP supercell storm. Microphysical and kinematic structures of storms are known to greatly influence the resulting distribution of charge and the lightning activity through the dependence of both electrification and lightning on noninductive charging. The riming rate (influenced by the cloud water content, discussed in more detail below) affects the polarity of charge gained by graupel, and this, along with the trajectories of oppositely charged graupel and cloud ice particles as they are advected by the wind and separated through gravitational sedimentation, governs the overall charge structure of a storm. Some of these basic relationships for supercell storms will be explored through analysis of the data from 29 May 2004.

1.1.1 Electrification of Thunderstorms

The dominant charging process in thunderstorms is believed to be the noninductive charging process, which involves rebounding collisions of graupel and ice crystals in the presence of supercooled water droplets. The polarity and amount of charge transferred per collision (Fig. 1.2) is dependent upon the diffusional growth rate of the two ice surfaces at collision, which itself depends on multiple factors including the effective liquid water content, fall velocity, and temperature as well as the size (and shape) of the ice crystals (e.g., Takahashi 1978; Saunders 1993; Brooks et al. 1997; Saunders and Peck 1998; Saunders et al. 2006). Overall thunderstorm charge is determined by the separation of these charged particles through differential sedimentation and the convective flow of a storm. In addition to noninductive charging, inductive charging could play a role in thunderstorm electrification. Inductive charging occurs in the presence of an electric field when a rebounding collision occurs between two polarized particles. Though inductive charging cannot account for charging in the early stages of thunderstorm electification, it is possible that it works in conjunction with the noninductive process (Saunders 1993).

The simplest conceptual model of the gross electrical structure of thunderstorms is typically described as either dipolar or tripolar, with the main charges being a middle-level negative charge and an upper level positive charge. A small, sporadic positive charge has sometimes been found beneath the negative charge to form a

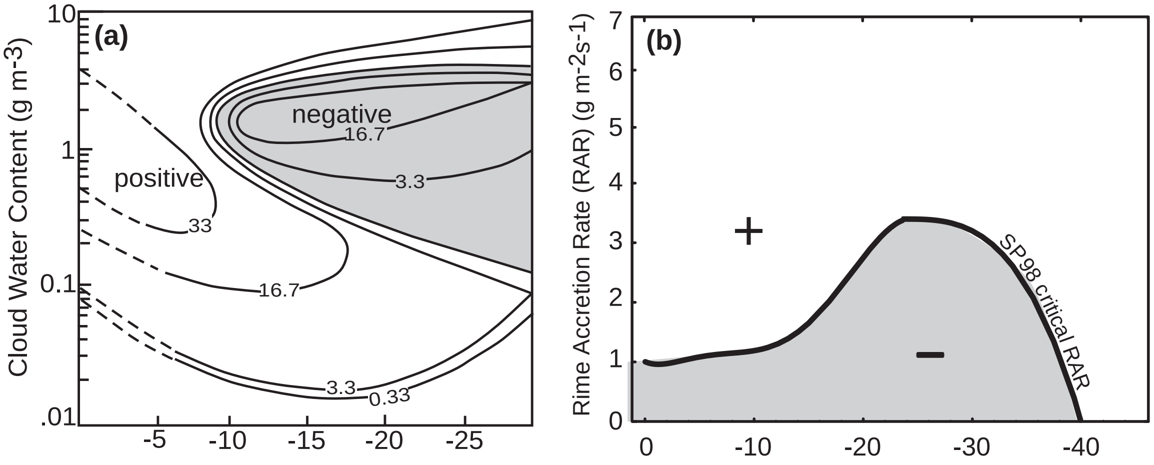

Figure 1.2: (a) The polarity of charge gained by graupel as a function of temperature and cloud water content, adapted from Takahashi (1978), note exponential scale. (b) The polarity of charge gained by graupel as a function of temperature and RAR according to the laboratory experiments of Saunders and Peck (1998). Graupel gains positive charge above the curve at higher rime accretion rates and negative charge below the curve.

tripolar structure (e.g., Williams et al. 1989), and a negative screening-layer charge also is often found near the upper cloud boundary.

Several studies have suggested that dipole or even tripole models are not sufficient to describe how charge is distributed in all thunderstorms. Rust and Marshall (1996) argued that the tripole model was too simplistic to apply to all mature thunderstorms and mesoscale convective systems. Additional analyses of in-situ balloon borne electrical measurements were synthesized to depict a more complex charge structure consisting of four main charge regions near the updraft and six charge regions outside the updraft in the convective precipitation region (Stolzenburg et al. 1998). Additional field measurements of thunderstorms in various regions of the United States, combined with new storm analysis techniques using the LMA and storm modeling have found various configurations of charge in different storms (Fig. 1.3).

The existence of an inverted-polarity storm (a main positive charge between an upper and lower negative) was first suggested by Marshall et al. (1995) based on an

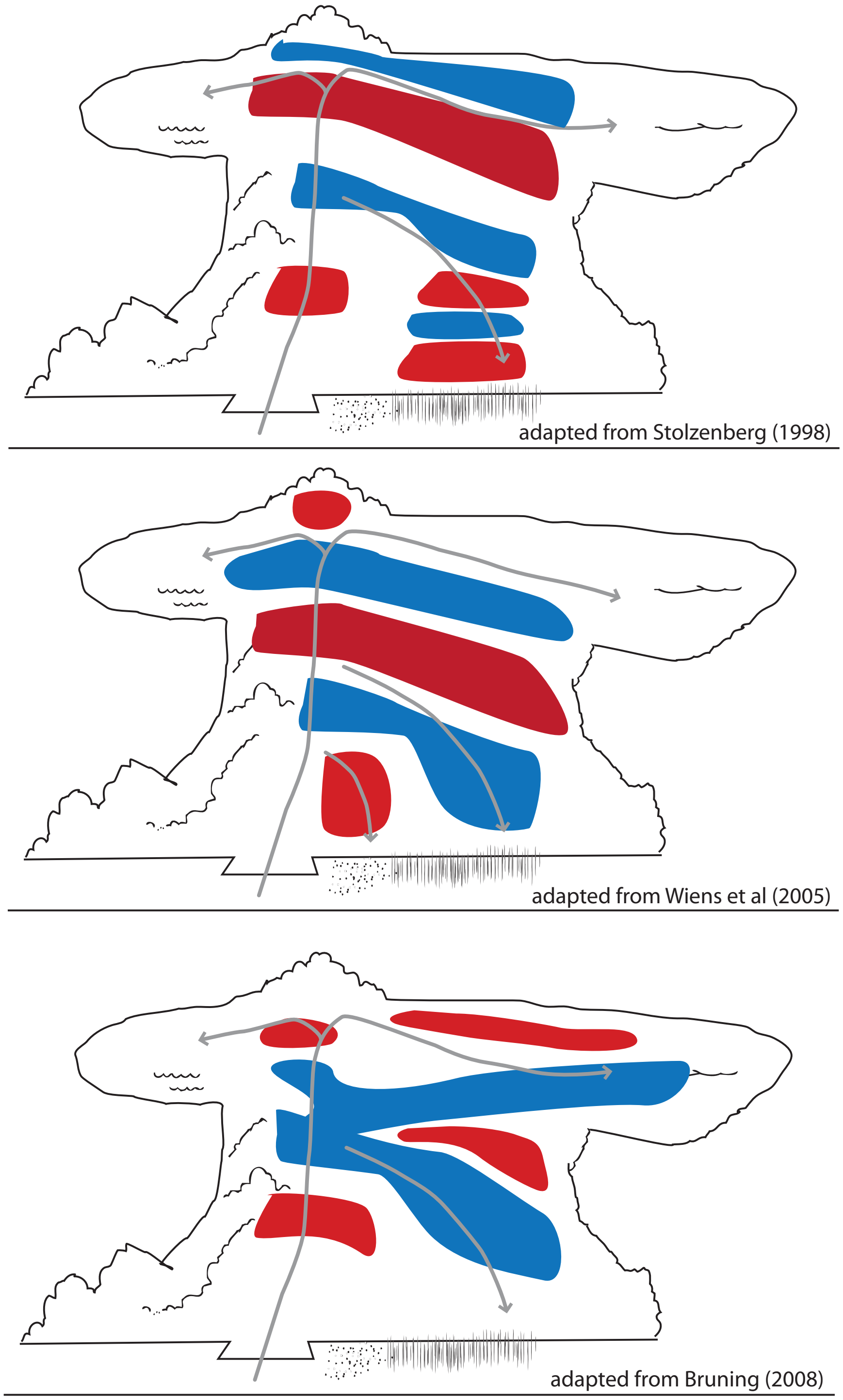

Figure 1.3: Observational charge structure of thunderstorms adapted from analyses by (a) Stolzenberg et al. (1998), (b) Wiens et al. (2005) of 29 June 2000, and (c) Bruning (2008) of 26 May 2004.

in-situ electric field sounding of a strong storm near Dalhart, Texas. Marshall et al. suggested that the + CG flashes in the Dalhart storm immediately following the sounding may have resulted from the inverted charge structure of the storm. More definitive evidence for storms sometimes having inverted-polarity electrical structure were provided by data from the Severe Thunderstorm Electrification and Precipitation Study (STEPS), studied by Rust and MacGorman (2002), Rust et al. (2005), MacGorman et al. (2005), Wiens et al. (2005), Tessendorf et al. (2007a), and Weiss et al. (2008).

It has been suggested, by both recent observations and modeling studies, that the inverted tripole structure is due in part to the positive charging of graupel and negative charging of smaller ice hydrometeors in the core of the updraft where the enviroment is abundant with supercooled liquid water. This would yield a main region of positive charge at middle altitudes of the storm and an upper region of negative charge. Collisions on the periphery of the updraft, a region of relatively lower levels of supercooled liquid water where ice crystals are likely to be growing faster, would result in the graupel charging negatively, possibly providing the lowest negative charge region of the storm (MacGorman et al. 2005; Wiens et al. 2005; Kuhlman et al. 2006b; Saunders et al. 2006).

In analyzing multiple regions of a storm at different stages of developement, Wiens et al. (2005), Weiss et al. (2008) and Bruning (2008) all found that charge was often quite localized and dependent on the characteristics of the main updraft region (Fig. 1.3). Through the course of its evolution the same storm could be predominantly dipolar, tripolar, or could have a more complex structure. The complexity of the storm charge structure typically depends on storm maturity, with longer lived storms having more complex structures. Also noted in all of these studies was the presence of opposite polarity charge layers present at the same altitude; some areas of the storm contained a normal polarity charge structure and other areas were best depicted by an inverted polarity structure as inferred from LMA data.

1.1.2 Supercells and Total Lightning

A supercell is commonly defined as a convective storm containing a persistent mesocyclone present through a significant portion of its depth (Klemp 1987; Brooks and Saunders 1994; Moller et al. 1994). In general, supercells have been noted for having much larger flash rates compared to other thunderstorms (e.g., MacGorman 1993; Wiens et al. 2005; Goodman et al. 2005). Three categories of supercells have been put forth in the literature based on the spatial distribution and amount of precipitation relative to the updraft and mesocylone (Moller et al. 1994; Rasmussen and Straka 1998). These include the low-precipitation (LP), classic, and high precipitation (HP) supercell.

An LP supercell, quite often described as a "skeleton of a supercell," produces little rainfall through the updraft and has no strong downdraft due to a lack of evaporational cooling, but commonly produces hail (Bluestein and Parks 1983). These supercells are most common in the high plains east of the Rocky Mountains and in western portions of the central plains typically near the dryline. LP supercells rarely produce tornadoes and severe weather is typically limited to large hail. Lightning flash rates appear to be smaller in LP supercells than in other types of supercells; in particular, they usually produce few, if any, CG flashes. However, LP storms have shown a tendency to have their CG activity dominated by +CG flashes more frequently than other types of storms (Branick and Doswell 1992; Curran and Rust 1992; MacGorman 1993; MacGorman and Burgess 1994; McCaul et al. 2002).

The classic supercell, as conceptualized by Browning (1964) and Lemon and Doswell (1979), is typically an isolated storm, occurring in the central to southern plains region and responsible for the majority of severe weather phenomena including most significant tornadoes. Typically, a classic supercell storm has a precipitation-free updraft region, although hail and large raindrops may be falling in this area, and has an area of heavier precipitation downshear from the updraft. The radar signature includes the well-known hook echo, which typically has reflectivities slightly less than the precipitation core (Doswell and Burgess 1993), as well as a bounded weak echo region (BWER) (Moller et al. 1994).

Lightning activity in a classic supercell is characterized by relatively high flash rates, often around 300 per min (Wiens et al. 2005). CG activity in classic supercells can be dominated by either negative CG flashes (Shafer et al. 2000), positive CG flashes (Wiens et al. 2005), or a transition from predominately positive to negative CG flashes (MacGorman and Burgess 1994; Perez et al. 1997; Smith et al. 2000; Carey et al. 2003a). The predominate polarity of CG flashes is controlled by the charge structure of the storm, which is dependent on the region of the country and mesoscale environment (Carey et al. 2003b). Often as a supercell storm makes the transition from LP (near the dryline) to classic, a switch in the predominate polarity of ground flashes will occur, changing from positive to negative (Curran and Rust 1992; Branick and Doswell 1992; MacGorman and Burgess 1994).

The HP supercell is believed to be the most common type of supercell storm (Moller et al. 1994; Rasmussen and Straka 1998). These storms are most common in the southeastern United States and in other areas where high levels of precipitable water are present in the atmosphere or from neighboring storms which can augment the precipitation of the supercell. The HP storm is distinguished by the mesocyclone being embedded in heavy precipitation, especially on the west and southwest sides of the meocyclone. These storms tend to be larger than classic supercells and can have higher reflectivities in the hook echo than in the precipitation core (Moller et al. 1994; Finley et al. 2001). Due to their high precipitation rates, HP supercells have commonly produced flash floods. They also often produce large hail, damaging wind, and tornadoes (Moller et al. 1994; Rasmussen and Straka 1998). Often, supercells will make the transition from classic to HP in the latter stages of development.

There is little documentation of total lightning from HP supercells. Because they are often larger storms with more ice and precipitation, one would expect higher flash rates than with LP and classic supercells. Observations of HP supercells in northern Alabama have shown flash rates ranging from 150 to 800 per min, as determined from LMA data (Bridenstine et al. 2005; Goodman et al. 2005). HP supercells are most commonly associated with predominately −CG flashes, as are most storms in the southeastern United States (Branick and Doswell 1992; MacGorman and Burgess 1994).

1.2 Questions addressed by this work

1.2.1 How is charge generation reflected by the magnitudes and trends of flash rate during the evolution of the 29 May 2004 HP supercell?

In a supercell storm, one would expect that charge generation is quasi-steady state, but at the same time could show some dependency on changes in storm strength. The charge transfer must be large enough to maintain the extremely high flash rates that are observed through its mature stage. Deierling et al. (2005) investigated the relationship between lightning frequency, downward flux of precipitation (graupel) and upward mass flux of ice crystals. They investigated how these microphysical fields, i.e., either the graupel or the cloud ice concentrations, controlled the rate of regeneration of the electric field and thus the lightning frequency. Deierling et al. (2005) proposed that the graupel concentrations ultimately limited the regeneration of the electric field. However, this was only speculation; there was insufficient observational evidence. Williams (2001) and Williams et al. (2005) have shown that abrupt increases in the total lightning flash rate are likely associated with a rapid development of the updraft, presumably aiding the production of ice and, thus, enhancing noninductive charging. Numerical simulations by Baker et al. (1995) and Solomon and Baker (1998) examined the flash rate relative to updraft speed, as well as precipitation rate, and ice concentration; however, their results may be limited by the simplicity of their 1.5 dimensional model.

In the study of the 29 June 2000 STEPS supercell, Wiens et al. (2005) found that the best correlations of total lightning flash rates were with the graupel echo and updraft volume and suggested this was due to the link with noninductive charging. A full, three-dimensional numerical simulation of the same supercell storm by Kuhlman et al. (2006b) showed relationships similar to those found by Wiens et al. (2005), with total flash rates being correlated best with graupel volume and updraft mass flux, while total flash rate appeared to have little dependence on maximum updraft speed.

This dissertation will discuss the hypothesis that the dependence of lightning flash rates on graupel production and updraft mass flux is what allows the HP supercell to have such a high flash rate, e.g., the ability to regenerate charge quickly. If the paradigm that electrification of the storm is dominated by noninductive charging is correct, lightning flash rates would be expected to be dependent upon graupel volume and updraft mass flux (though not updraft speed alone). This study will test this hypothesis and further investigate the relationship of lightning to graupel and updraft by using observations of the spatial distribution of lightning relative to the updraft core and storm kinematics, analyses of charge generation and flash location, and by analyses of the microphysics in numerical storm simulations enhanced by the use of mobile radar data assimilation.

1.2.2 How do updraft strength and size control the overall polarity of the storm and polarity of ground flashes?

A consistent result from all laboratory studies of noninductive charging is that at relatively warm temperatures (i.e., greater than -10°C) and at high liquid water contents, where graupel may be growing faster than ice crystals, graupel accumulating positive charge (Fig. 1.2; Takahashi 1978; Saunders and Peck 1998; Saunders et al. 2006). Typically, in a complex environment such as a thunderstorm, graupel could be gaining positive charge in some regions and negative in others (such as the periphery of the updraft core), though one graupel polarity can still dominate the charge at a given altitude. The storm height, flash rates, and large extent of the downshear anvil of the 29 May 2004 supercell are all evidence of a very large updraft mass flux, which would lead to a large liquid water content. It is plausible that the liquid water content within this storm was large enough to cause positive charging of graupel, and this should be apparent in the regions of charge determined by lightning activity. This issue will also be examined in the numerical simulations of the supercell in Chapter 5, along the lines of previous work by Mansell et al. (2005) and Kuhlman et al. (2006b).

As stated previously, the classic paradigm of normal polarity storms is that they have a region of negative charge at mid-altitudes and a region of positive charge at upper levels, with positive charge at low levels and lesser amounts of negative charge near the upper cloud boundary forming a screening layer. Inverted polarity storms contain positive charge at mid-levels with an upper negative charge and smaller lower negative charge, opposite from the usual charge structure. Most research studies suggest that normal polarity storms have a predominance of negative CG flashes while inverted polarity storms are dominated by positive CG flashes.

Negative ground flashes typically occur when there is a small amount of positive charge beneath a large negative charge. There has been less data concerning the initiation of positive ground flashes, but recent storm modeling (e.g., Mansell et al.

2002) and observations during the STEPS field campaign (e.g., Wiens et al. 2005; Weiss et al. 2008) suggest that positive ground flashes are initiated between a large positive charge at mid-levels and a small lower region of negative charge. Because this configuration would be characteristic of inverted storms, the ground flashes produced by inverted polarity storms would usually be expected to be predominately positive ground flashes. However, this hypothesis needs to be tested on data sets outside the STEPS domain (Rust et al. 2005).

Williams et al. (2005) hypothesized that a high cloud base height is partially responsible for inverted polarity storms and the corresponding prevelance of + CG flashes. Many of the storms in which ground flash activity is dominated by +CG flashes occur near dryline environments and in the High Plains of northwest Kansas and southwest Nebraska, where cloud bases tend to be high. A high cloud base height makes the "coalescence zone" (i.e., the area between cloud base and the 0°C isotherm) more shallow, and thus may lead to higher concentrations of cloud droplets in the mixed phase region and positive charging of graupel. Because cloud base tends to be lower in the Southern Plains and for HP storms, one might not expect this to be true for the 29 May 2004 supercell.

A similar result could be achieved by other factors. MacGorman et al. (2005, 2008b) suggested less recycling of precipitation into the updraft might be responsible for allowing a larger fraction of the liquid water content to remain liquid in the mixed phase region of updrafts due to less scavenging of cloud droplets at lower levels. Like the idea proposed by Williams et al. (2005), this would be consistent with +CG flashes being more prevalent near the dryline and in LP storms. It is possible that a different combination of processes contribute in different storms.

1.2.3 How is the spatial distribution and evolution of lightning governed by trajectories of hydrometeors relative to charge generation from the updraft core?

Several aspects of the distribution of lightning in the 29 May supercell can be considered within this broad question. Each will be discussed separately.

1.2.3.1 *How does the maximum density of lightning reflect the locations in which charge is replenished most rapidly?*

In an analysis of lightning in a supercell storm, Ray et al. (1987) found that the majority of lightning tended to be located downshear from the main updraft core in the reflectivity core. In addition to the analysis of the supercell, Ray et al. (1987) also examined a non-supercellular severe storm containing a more upright updraft structure with symmetric divergence at storm top. In this storm lightning was concentrated in the updraft and reflectivity core at mid-levels and in a broader cap in the diverging upper flow. As shown by MacGorman et al. (1983) for a severe storm, Ray et al. (1987) surmised that the distribution of lightning reflected the structure of the wind field relative to the updraft within the storm. In this dissertation, data from the LMA are combined with dual-Doppler analyses to examine how the location and characteristics of lightning changes as the storm kinematics evolve. The maximums in lightning activity should reflect the locations of greatest replenishment of charged hydrometeors, which, according to the hypotheses of Ray et al. (1987) and MacGorman et al. (1983), should be just above and downshear of the main updraft core.

1.2.3.2 *Are lightning holes caused by the lack of charged hydrometeors within a strong updraft core?*

The growth of precipitation is inhibited in the 0 C to -30 C layer within the very strong updrafts of supercell storms due to an insufficient amount of time for precipitation to form and grow, as small hydrometeors are rapidly swept upward with the air. Aircraft penetrations through roughly the -5 to -20 C levels of strong updraft (30-50 ms^{-1}) have detected no precipitation sized particles and few ice particles, it is this lack of radar-detectable particles that is the source for the bounded weak echo region (BWER) (Musil et al. 1986; Loney et al. 2002). The BWER is a nearly vertical area of weak radar echo, surrounded on the sides and top by significantly stronger echo. It is typically found at midlevels of strong convective storms, and its horizontal extent is generally a few kilometers in diameter.

The lack of precipitation sized particles, including graupel, in the BWER greatly inhibits the noninductive charging mechanism thus reducing the total lightning activity in that region. This lightning hole (or lightning weak) region has been noted in strong supercells (e.g., Krehbiel et al. 2000; MacGorman et al. 2005) coincident with a BWER. This signature is apparent both in horizontal and vertical cross-sections of lightning activity within the 29 May 2004 supercell, detailed analysis of extended time periods will be used to examine the evolution of the lightning hole relative the updraft and BWER evolution.

1.2.3.3 *Do updraft impulses cause the rising regions of lightning above the equilibrium level?*

The analysis related to this hypothesis explores the character of lightning above the equilibrium level. Little is known about lightning occuring in the region of the overshooting tops of thunderstorms. Lightning VHF sources were noted by Ray et al.

(1987) in the region above the main updraft core in a supercell storm, but not specifically in the overshooting top. More recently, lightning mapping technology has detected a secondary maximum of VHF sources in the overshooting tops of supercell thunderstorms (MacGorman et al. 2008a). Observational evidence suggests that the timing of these channels is associated with new updraft surges. The stronger the updraft, the higher the height at which the charge produced by noninductive charging in the mixed phase region will be lofted. This is partly because supercooled liquid water and associated hydrometeors are lifted up much higher in the storm and partly because the stronger updraft penetrates further above the equilibrium level. It is unknown whether the lightning in this region is initiated in the same way as other flashes, i.e., between two layers of charge, or if it is actually initiated between a top layer of charge associated with cloud ice and a screening layer. Taylor et al. (1984), for example, noted that lightning near the top of storms appeared to produce a continuous, but low rate, of individual VHF sources, and this suggests that either the physics of electric breakdown is somewhat different at these altitudes (Marshall et al. 2005) or that the charge regions connected to this activity are quite small in spatial extent or a combination of these factors. It is also possible that other mechanisms besides noninductive charging are responsible for the charge in the overshooting top. It is a viable option that another process such as the formation and entrainment of screening layer charge from the capture of ions at the cloud boundary contributes to an enhancement of charge necessary for increased lightning activity in this region.

1.2.3.4 *Are supercell storms with extremely high flash rates actually dominated by flashes that are shorter in time and horizontal extent than the "average?"*

In highly turbulent storms, it is likely that smaller pockets of opposing charge will be in close proximity to each other, thereby initiating lightning but not allowing for lightning to travel far horizontally. Also, frequent lightning may create holes in a region of charge thereby limiting the distance over which subsequent lightning can propagate. It is possible that the very large flash rate observed in the 29 May supercell relative to most storms was aided by the small extent of flashes that were observed. This issue is examined in Chapter 3 by analyzing mapped lightning flashes for periods of time and regions of the storm having greatly different flash rates and by comparing flashes in this storm with flashes in smaller, less severe storms.

1.2.4 How and why and what type of lightning may be initiated in supercell storm anvils?

A thunderstorm anvil is formed as bouyant air within the thunderstorm updraft reaches its equilibrium, and the air is forced to diverge horizontally. The result is a flat-topped cloud similar in appearance to a blacksmith's anvil. The asymmetry of the thunderstorm anvil is due to environmental winds pushing the diverging air downshear from the updraft. Anvils in supercell storms often extend over 100 km from the main convective core, as hydrometeors move downshear at a storm relative speed of roughly 20 $m\,s^{-1}$ (Heymsfield 1986).

Thunderstorm anvils are known to carry substantial electrical charge (Marshall et al. 1989; Dye et al. 2007) and lightning is known to extend from the storm core into the anvil region. While investigations have found electric fields large enough for the propagation of lightning, it has been generally believed that "little or no lightning actually initiates there" (Stolzenburg and Marshall 2008). Dye et al. (2007), showed, for example, that anvil lightning was confined to the regions closest to the storm core, with flashes being initiated near or in the core and following layers of charge horizontally downshear into the anvil. Similarly, anvil flashes from the 29 June 2000 STEPS supercell were typically contained within reflectivity greater than 25 dBZ (Wiens et al. 2005). Another, much weaker storm observed during the STEPS campaign, contained flashes that were initiated near the edge of the storm core into the anvil region but at limited distance downwind from the storm core (Tessendorf et al. 2007b). Up to this point, most observations have found that CG flashes emanating from the more distant anvil region are typically of postive polarity, with negative CGs occurring closer to the storm core (Rust et al. 1981; Wiens et al. 2005; MacGorman and Nielsen 1991; Tessendorf et al. 2007a).

As evidenced from the LMA, lightning in the anvil region of 29 May 2004 extended over one hundred kilometers downstream from the edge of the 30 dBZ reflectivity core. Some lightning actually began in the anvil region and then progressed back towards the core of the storm. Analysis of the OKLMA data combined with EFM soundings and dual-doppler wind fields is discussed in Chapter 4. Numerical simulations of 29 May 2004 in Chapter 5 are used for further evaluation and understanding of the anvil charge and lightning initiation in this storm.

Chapter 2

Data Description and Analysis Techniques

2.1 Lightning Data

Lightning activity, both in-cloud and cloud-to-ground, can give insight into storm charge structure. The main tools used to investigate lightning in this study are the Oklahoma Lightning Mapping Array (LMA) and the National Lightning Detection Network (NLDN). Additional in-situ measurements of storm charge are determined using data from balloon-borne electric-field meters.

2.1.1 The Lightning Mapping Array

Maps of lightning channel discharge geometry and flash rates were acquired using the Oklahoma Lightning Mapping Array (LMA) (Fig. 2.1). The Oklahoma LMA (Rison et al. 1999; Thomas et al. 2004; MacGorman et al. 2008b) is a Global Positioning System (GPS) based, time-of-arrival system that maps lightning by measuring the time at which an electromagnetic signal produced by a developing lightning channel arrives at each station in the array in central Oklahoma. The LMA was patterned after the Lightning Detection and Ranging (LDAR) system developed by Carl Lennon and others at the NASA Kennedy Space Center and described by Maier et al. (1995). The LMA can map up to 12,000 sources per second, and in the storm studied in this dissertation, typically mapped ten to several hundred points per flash.

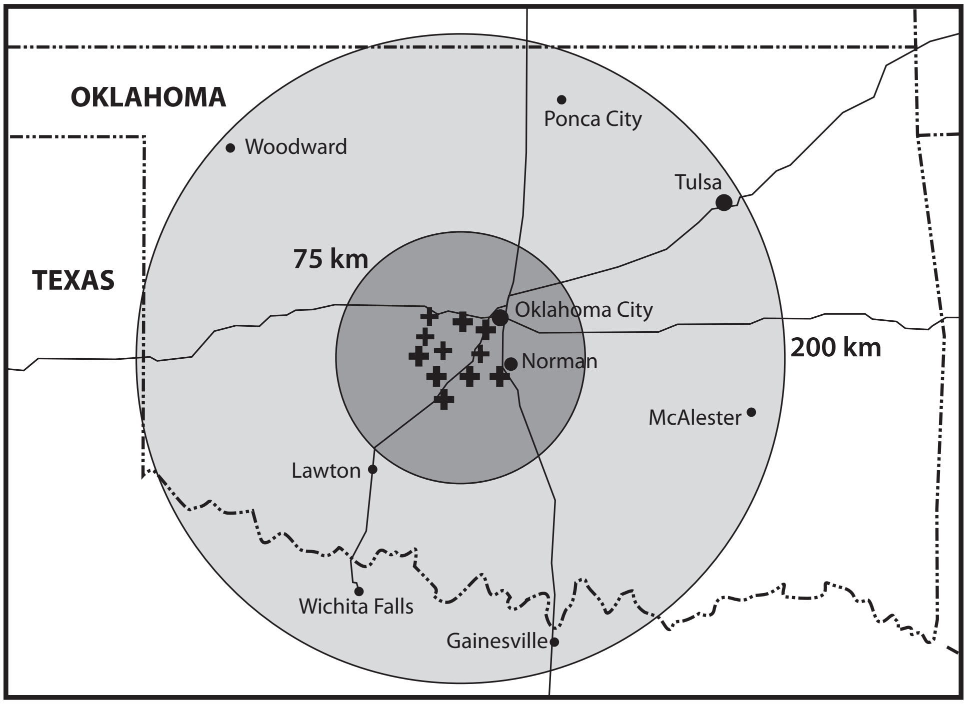

Figure 2.1: Oklahoma LMA network. The location of each of the 11 stations in the network is marked with a + symbol. The 3d range of the network is the dark gray circle (nominally 75 km from the network center); the 2d range is the 200 km lighter gray circle.

The Oklahoma array has eleven stations spaced 10-22 km apart (Fig. 2.1), each of which receives signals in a locally unused television channel (Ch.3) in the very high frequency (VHF) band. The system measures the arrival time independently at each station with 50 nanosecond time resolution (Rison et al. 1999) of the largest peak radiation event exceeding a noise threshold in each 80 microsecond window (Hamlin 2004). This process assumes that the same VHF event will produce the peak power received at each station in the array within that window. Occasionally, this assumption is violated, resulting in a nonphysical ”noise” point. From the fraction of points that are mapped, it appears that fewer than one out of 100 points results from such a violation (Hamlin 2004).

The processing of the data for TELEX to determine VHF source locations was completed using software developed by New Mexico Institute of Mining and Technology (Thomas et al. 2004; MacGorman et al. 2008b). One of the most important aspects of this processing is determining whether different sets of arrival times at the various network stations belong to the same event or not (Hamlin 2004). In order for an event to be counted in the final data set, it must be recorded by at least six stations. The station the event is closest to will measure the event first followed by the other stations in order of increasing distance (Fig. 2.2). The software takes the data from each of the 11 stations and finds combinations of time of arrival that are possible for signal propagation at the speed of light of each recorded event. It then iteratively finds the the location and source time that give the least-squares error for each combination and chooses as the solution the location and time from the combination that produces the smallest reduced chi-squared value (Fig. 2.2).

Typical measurement errors are within 6-12 m in the horizontal, 20-30 m in the vertical and 30-50 nanoseconds with the smallest errors in the center of the network and increasing with increasing range (Thomas et al. 2004). The effective range of the LMA is constrained by the propagation characteristics of VHF signals and by the effects of the array geometry on VHF source point calculations. Signal amplitude decreases linearly with range from the source and eventually falls below the threshold for detection, with only the stronger sources being detected at longer ranges. Furthermore, VHF signal detection is essentially line-of-sight, so sources below the LMA's horizon can not be detected. Finally, errors in computed locations, particularly in the vertical coordinate, increase rapidly with range outside the perimeter of the network. For these reasons, the effective range of the OKLMA is roughly 100 km from the network center for three-dimensional locations and 200 km for two-dimensional (x and y only) locations (Fig. 2.1).

The data are available as both a decimated data set (roughly 20% of the total; used commonly in real-time analyses) and the full data set. For this study, the full data set containing all available data were used in the analyses.

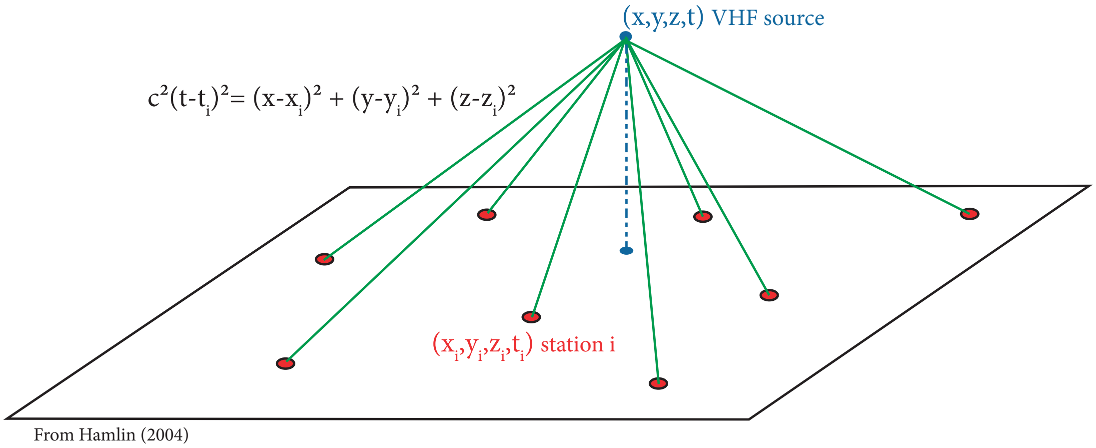

Figure 2.2: Diagram of LMA system geometry and time of arrival technique. VHF source point in blue and station locations in red. From Hamlin (2004).

2.1.1.1 Flash sorting and initiation height determination

Individual flashes were determined by using a flash algorithm developed by Thomas et al. (2003). The algorithm determines whether an individual VHF source point belongs to a given flash by using time and space constraints (3 km and 150 ms) and then determines the number of points the flash includes. When flash rates are large, as was the case with the storm studied in this dissertation, separation of the many VHF points into individual flashes becomes more difficult due to the continuous activity. The algorithm limits flashes to a maximum duration of 3 seconds for a single flash. The sizes of flashes are separated into small (1 VHF point), medium (fewer than 10 points), large (between 10 and 100 points), and extra large (greater than 100 points). Only large and extra large flashes are being counted in the total flash rates in this study.

Initiation height is determined by an algorithm developed by Lund (2008). This algorithm determines the initiation location of a flash containing 10 or more VHF source points. The algorithm groups the first 10 VHF points of a single flash and determines the average latitude, longitude, and height and standard deviation. If the standard deviation is greater than 0.5 km, an outlier VHF source point is dropped from the averaging until the standard deviation is less than 0.5 km. To reduce misplaced locations, the algorithm requires that at least five source points be used in the calculation.

2.1.1.2 Determination of Charge Regions

Individual flashes mapped by the LMA can be analyzed to infer the regions of storm charge involved in a flash. According to the bi-directional model (Kasemir 1960; Mazur and Ruhnke 1993), which has become the paradigm for understanding lightning development, lightning is initiated between regions of opposite charge where the magnitudes of the electric field are near a local maximum. The lightning then propagates into regions of opposite charge, with the negative leader traveling toward and into regions of positive charge and the positive leader traveling toward and into regions of negative charge. Numerical modeling studies (Mansell et al. 2002) and laboratory studies using sparks (Williams 1985) further expanded on this concept showing that the discharge preferentially travels into regions of higher charge density.

Shao and Krehbiel (1996) and Rison et al. (1999) have demonstrated that VHF mapping systems such as the LMA preferentially map negative leaders (which tend to propagate through positive charge), as negative leaders produce much more noise at the radio frequencies used by the LMA than positive leaders do. Thus, individual flashes can be examined to identify the charge structure of the storm (Wiens et al. 2005; Rust et al. 2005). This method requires a flash-by-flash analysis, subjectively partitioning the first several sources and higher density activity (positive charge) from the sources occurring later and at lower density (negative charge). An example of an analyzed flash is shown in Fig. 2.3. The flash is initiated at just above 10 km and initially proceeds downward with negative breakdown into inferred positive charge.

Later, a distinct line of points begins to occur above 10.5 - 11 km, an area of inferred negative charge.

2.1.2 National Lightning Detection Network

The cloud-to-ground lightning data used in this study were collected by the National Lightning Detection Network (NLDN). The NLDN consists of over 100 ground-based sensing stations located across North America that detect electromagnetic signals from lightning channels to ground (Cummins et al. 1998). The system underwent an upgrade during 2002 and 2003 to increase detection efficiency and location accuracy (Biagi et al. 2007). The Biagi et al. (2007) study, as well as other preliminary studies by Johnson and Mansell (2006) and Kuhlman et al. (2006a) comparing LMA data with NLDN in Oklahoma, found that many ($> 50\%$) of the low amplitude events (both negative and positive) were not actually ground strikes, but in-cloud discharges. To avoid contamination of the data, all strikes, positive and negative, were only used when the peak current of the first stroke was greater than 10 kA. This threshold was chosen based on the above mentioned studies and as suggested by Cummins et al. (1998) for positive CG flashes.

2.1.3 Electric Field Meters

Balloon-borne instrumentation were released into the storm on 29 May 2004 at three different times. Two of these flights contained an electric field meter (EFM) which provided vector electric field (**E**) measurements. This instrumentation was first developed by Winn and Byerley (1975) and upgraded for TELEX to include in-flight data recording (which provided cleaner data, but necessitated recovery of the instrument) as well as more durable construction and improved orientation reference signals through a new two-axis accelerometer and three-axis magnetic field sensor (Bruning et al. 2007). The vector Electric field, **E**, is determined as the EFM spins

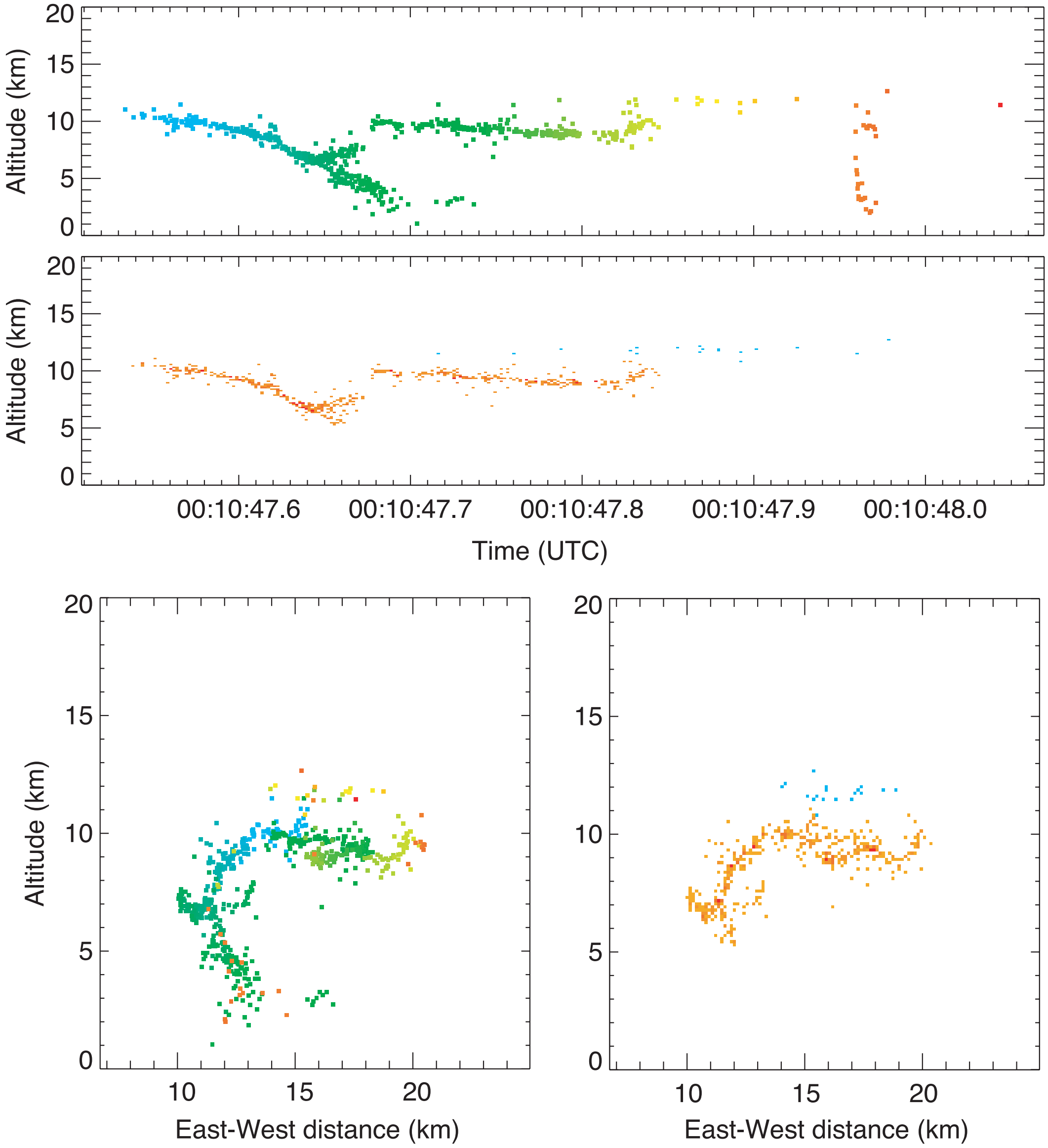

Figure 2.3: VHF points from a single flash occurring at 0010:47.6 UTC. Top two panels show vertical projection of VHF sources versus time, with points in upper panel color coded by time and in lower panel color coded by inferred storm charge (orange is positive charge and blue negative). Bottom two panels give vertical projection in east-west direction. Left panel has sources color coded by time (as in the top panel) and right panel is color coded by storm charge.

about its vertical and horizontal axes at approximately 1 and 3 Hz, respectively, thereby producing a sinusoidal raw electric field signal. An approximate expression for Gauss' law (Eqn. 2.1) is used in conjunction with the measurement of **E** by the EFM to infer the charge at the given location. Gauss's law (in one dimension) is given by:

$$\nabla \cdot \vec{E} = \frac{\rho}{\epsilon} \tag{2.1}$$

where ρ is space charge density, ϵ the permittivity of air (8.86×10^{-12}), and **E** is the vector electric field. This approximation assumes that the horizontal derivatives can be ignored. A vertical profile of storm charge can then be determined. Note, however, that the EFM only measures the vector electric field along the flight path of the instrument and this charge profile may not be representative of the entire storm (Bruning et al. 2007; Stolzenburg and Marshall 2008).

2.2 Radar Data

The use of Doppler radar to infer the dynamical structure of storms has been a common practice since the 1970's (Ray et al. 1975; Brandes 1977). This reserach primarily utilizes two mobile C-band radars, the Shared Mobile Atmospheric Research and Teaching (SMART) radars (Biggerstaff et al. 2005), and occasionally employs data from two S-band radars: KTLX, the National Weather Service (NWS) WSR-88D in Oklahoma City, OK, and KOUN, the NSSL polarimetric research radar located in Norman, OK.

2.2.1 The Shared Mobile Research and Teaching Radars

The SMART radars completed volume scans of the storm every three minutes for over two hours as it passed through central Oklahoma. Both SMART-radars transmitted at C-band and had a 1.5° beamwidth (Biggerstaff et al. 2005). For the majority of analyses shown in this study, the sector volume scans of approximately 120° were used for both radars, with the radars completing an entire volume scan in 1 min 50 sec. Elevation angles ranged from 0.5 - 33.5° with increments of 0.3 - 3.0°.

Data were edited by using the SOLOII software suite (Oye et al. 1995). The editing process manually removed ground blockage, velocity and range folding, and regions of high noise. With Nyquist velocities for SR1 and SR2 of 21 $\mathrm{m\,s^{-1}}$, velocity dealiasing for this supercell often involved more than one fold. Ground clutter was removed by identifying areas of near-zero velocity and high returned power at the lowest sweeps. A correction of azimuth orientation of +1.0° to SR1 and -0.8° to SR2 was also made.

2.2.2 Dual-Doppler Analysis

Dual-Doppler synthesis is a commonly used technique to estimate the three-dimensional wind field of supercell storms (e.g., Ray et al. 1980; Dowell and Bluestein 1997; Wurman et al. 2007). The SMART radars were deployed in a configuration suitable for dual-Doppler analysis for the supercell that passed through Geary, OK (west of Oklahoma City). Data collection started at 2247 UTC on 29 May 2004 and ended at 0212 UTC on 30 May 2004 (Fig. 2.4). Radial velocity and reflectivity from both SR1 and SR2 were interpolated onto a cartesian grid with a grid spacing of 0.5 km by using a single Barnes analysis (Majcen et al. 2008; Trapp and Doswell 2000; Koch et al. 1983) in order to compute the synthesis of the three-dimensional wind. As described in Majcen et al. (2008), the analysis uses the weighting function:

$$\omega_{jk,n} = exp\left(-\frac{r_{jk}^2}{\kappa_o \gamma^{n-1}}\right), \tag{2.2}$$

where $\omega_{jk,n}$ is the weight assigned to the kth radial observation at the jth grid point on the nth pass, r_{jk} is the distance (in km) between the grid point j and observation k, κ_o is the smoothing parameter (in km^2), and γ is the convergence parameter. For all the analyses used in this dissertation, a κ_o of 1.343 and γ of 0.3 was used. Though a Barnes analysis scheme was used, which, as seen in Eqn. 2.2 above includes an exponential weighting of all data out to infinity, a radius of 3 km was employed to place a practical limit on the data interpolated to a grid point.

Following interpolation to a cartesian grid, the three dimensional winds were computed from the radial velocity data. First, the horizontal components are computed using a least squares methodology and terminal fall speeds estimated from radar reflectivity. Then the vertical component is found combining the solutions for u and v with first an upward and then downward integration of the anelastic mass continuity equation (Eqn. 2.3) using boundary conditions of w=0 at the ground and above storm top.

$$\frac{\partial u}{\partial x} + \frac{\partial v}{\partial y} + \frac{\partial w}{\partial z} - \kappa w = 0 \tag{2.3}$$

where u, v, w are the x, y, and z components of the wind, respectively and *kappa* is the logarithmic change in density with height. The solution is weighted such that the upward integration is given an importance of 1 at the ground decreasing to 0 at the top with the downward integration weighted inversely.The differences between the two separate integrations are then averaged and and convergence to a final solution is achieved by iteration (Ray et al. 1980; Kessinger et al. 1987).

Dual-Doppler analyses were completed in this study for nine volume scans spanning the time period in which the storm moved through the TELEX domain: 2320, 2331, 2347, 2355, 0011, 0016, 0027, 0038, and 0052 UTC.

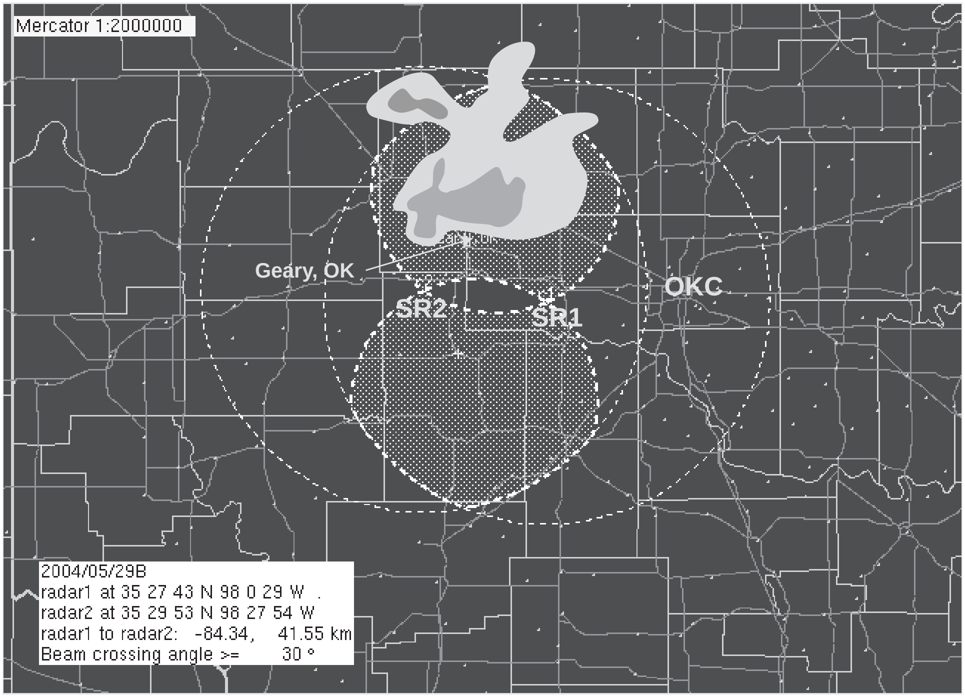

Figure 2.4: Schematic of SR deployment locations and storm reflectivity at 0016 UTC. Locations of SR2 and SR1 are labeled. Thick dashed lines mark the boundary of the dual-Doppler lobes, at a beam-crossing angle of $> 30°$. Hatched area inside each lobe represents areas where the beam-crossing angle is $> 30°$.

Chapter 3

Analysis of the 29 May 2004 supercell

3.1 Storm Overview

On 29 May 2004 multiple storms were initiated on a dryline located near the western Oklahoma-Texas border. By 2330 UTC, the southern-most cell became the most dominant and quickly developed supercell characteristics. With a strengthening low-level jet supplying moisture, the storm remained isolated and moved across the state (Fig. 3.1b) with a strengthening low-level jet supplying moisture before finally dissipating near the Oklahoma/Arkansas/Missouri border at approximately 0730 UTC. The storm produced its first F2 tornado at 0017 UTC over Blaine and Canadian counties, approximately 9 mi west-north-west of Geary, OK. The second F2 tornado began just as the first ended at approximately 0038 UTC moving from Blaine into Canadian county, north to northeast of Geary. In total, eighteen different tornadoes were produced by the storm across the state of Oklahoma including three F2 tornadoes and one F3 tornado. Hail reports of 1 - 2.75 in were common from the storm throughout its lifetime. The storm is estimated to have produced over 9 million dollars in property damage across the state.

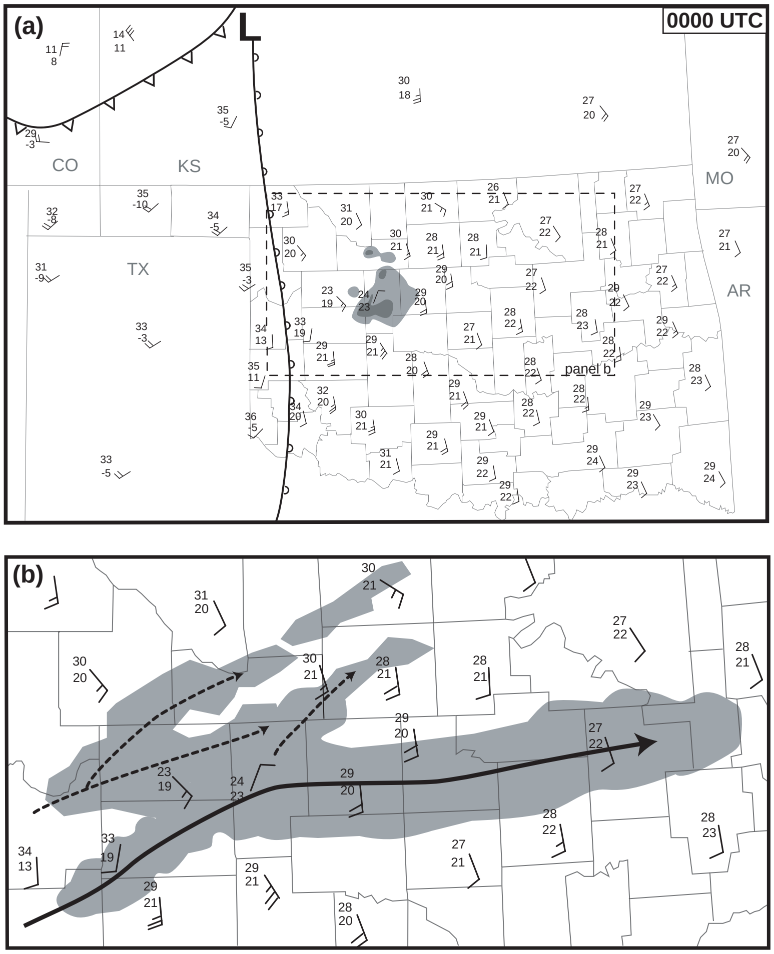

Figure 3.1: a) Surface observations and reflectivity from KTLX at 0000 UTC. Eastward moving dryline denoted by scalloped curve. (b) Evolution of storm tracks. Grey area indicates region of 30 dbZ reflectivity from 2200 UTC 29 May to 0500 UTC 30 May.

3.1.1 Environmental Conditions

Conditions across the central plains were extremely unstable on 29 May 2004 as an upper level trough moved across the area enhancing strong vertical shear. A surface low in southwestern Kansas and a strong dryline extending southward across western Oklahoma led to initiation of thunderstorms in the area (Fig. 3.1a). Afternoon temperatures and dewpoints to the east of the dryline were near 30°C and 22°C, respectively. Convection was originally delayed by a strengthening cap, but as the upper level-trough deepened, strong winds from the south at 20-25 $\mathrm{m\,s^{-1}}$ combined with surging dewpoints along an area of convergence at the dryline to initiate the first cells around 1940 UTC. An 1800 UTC sounding from Lamont, OK indicated large CAPE ($> 3000\,Jkg^{-1}$), veering winds with a peak of 50 $m\,s^{-1}$ at 220 hPa (Fig. 3.2).

The Storm Prediction Center in Norman, OK issued a high risk of severe weather across the majority of the central plains from Nebraska through central Oklahoma on the first Day 1 convective outlook; this outlook also included a 25% probability of a tornado, with a 10% or greater probability of F2 to F5 tornadoes within 25 miles of any point over that entire region (Fig. 3.3).

The tornado times and tracks contained within this study are taken from storm data, which combined data from the Doppler on Wheels (DOW), chaser accounts and field surveys (Don Burgess, personal communication, 2009). The particular tornadoes of interest during the analysis period include two F2 tornadoes: one at 0017-0038 UTC that travelled from northwest to north of Geary and another at 0038-0111 UTC that moved from north of Geary and ended in the vicinity of Calumet.

3.1.2 Storm Initiation and Evolution of Supercell Characteristics through Dual-Doppler Analysis

This study focuses on two storms that were initiated by the low-level convergence on a dryline located near the western Oklahoma-Texas border on 29 May 2004. The

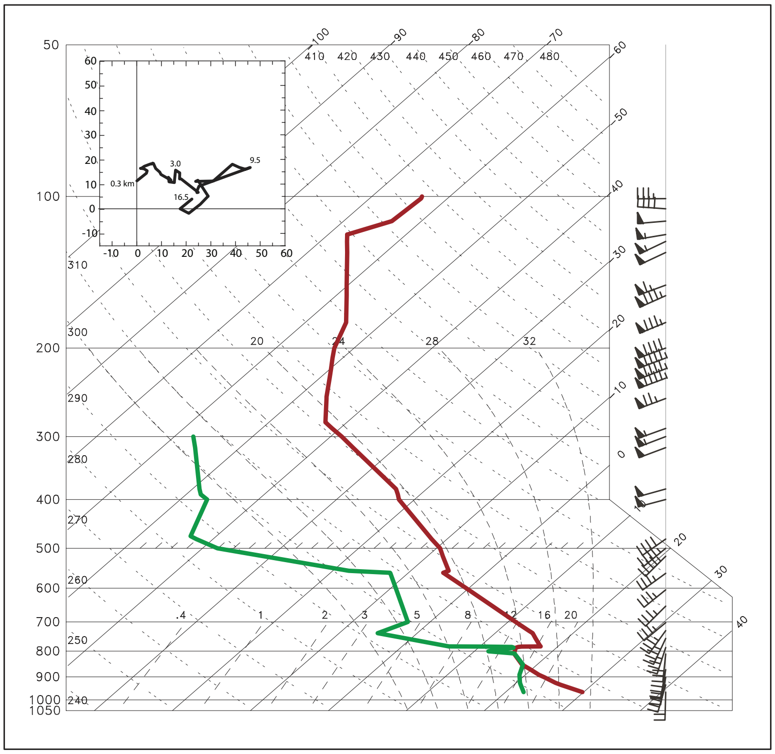

Figure 3.2: 1800 UTC sounding from Lamont, OK. CAPE=3281 $J\,kg^{-1}$, LCL = 859.1 mb. Winds are plotted with a filled flag = $25\,m\,s^{-1}$, full barb = $5\,m\,s^{-1}$, and half-barb = $2.5\,m\,s^{-1}$

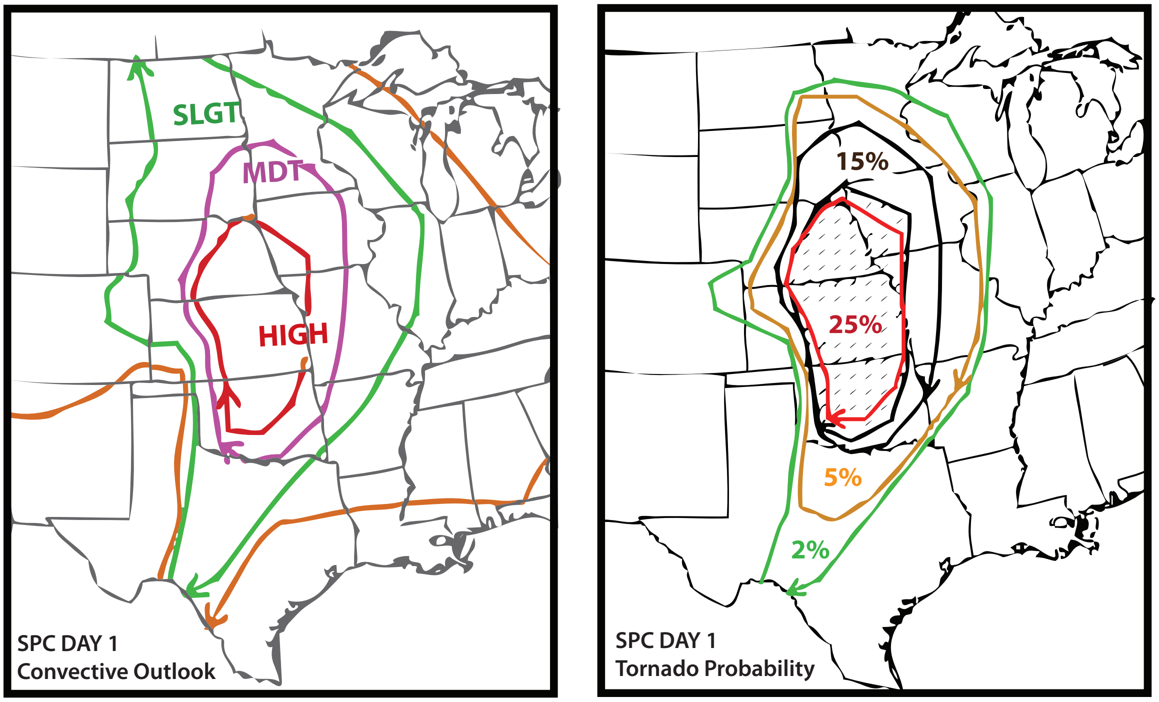

Figure 3.3: Day 1 convective outlook and tornado probability from the Storm Prediction Center in Norman, OK. 25% probability of a tornado within 25 miles from a point and high risk are noted over the TELEX domain in central Oklahoma. Hatched area represents region of 10% or greater probability of F2 to F5 tornadoes within 25 miles of any point.

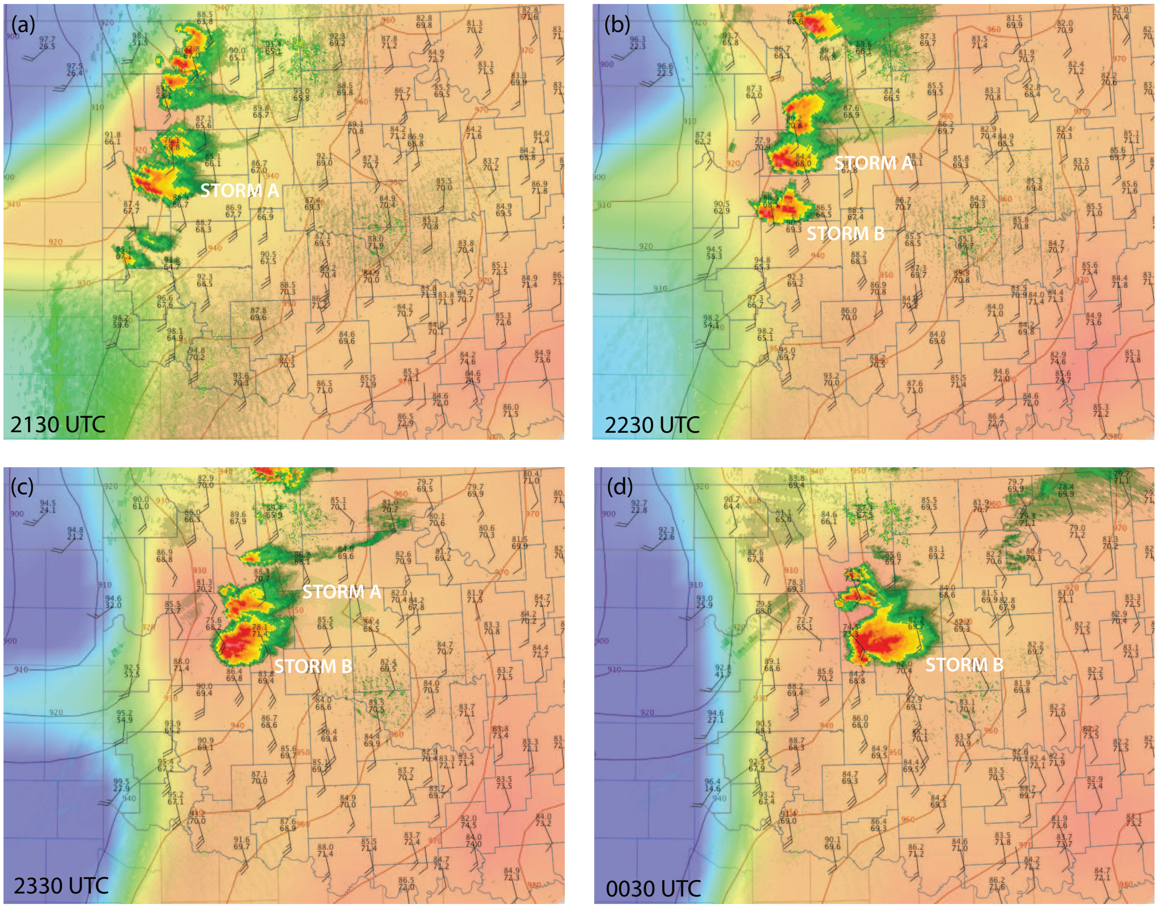

Figure 3.4: Evolution of ground observations from the Oklahoma Mesonet and base reflectivity from KTLX and KVNX radars. (a) 2130 UTC plots of mesonet tempearature, dewpoint at 1.5m and wind (knots) at 10 m. Atmospheric pressure is contoured in maroon in 10 mb levels. Mixing ratio is the background color gradient from 2 (blue) to 20 g/kg (red). (b) same as (a) except at 2230 UTC. (c) 2330 UTC (d) 0030 UTC.

first (storm A) was initiated at approximately 2030 UTC as the southernmost of three cells along the dryline. By 2130, at least four other storms were north of Storm A and two more cells had been initiated south of storm A (Fig. 3.4a). Storm A remained the strongest of these storms through the next hour and even began exhibiting supercellular characteristics, including rotation at mid-levels, as it moved northeast at 16 $m\,s^{-1}$ through 2230. During the following hour, 2230-2330, storm A's motion began to turn more eastward and slowed to 12 $m\,s^{-1}$. Meanwhile, the southernmost storm (storm B) rapidly intensified and moved northeast, eventually interfering with storm A's low-level inflow from the south. At 2329, storm B produced its first tornado, an F0 that moved across 6 miles south of Thomas, OK. From 2330 throughout the rest of the analysis period, storm B remained the strongest storm, and after 0030 UTC was the only storm in the TELEX domain.

The first dual-doppler analysis completed for the storms was at 2347 UTC (Fig. 3.5). [Note: all dual-Doppler times referenced are at the beginning time of the analysis period, each analysis covers roughly 3 min of scanning time by the SRs.] By this time, storm A was rapidly dissipating and storm B had slowed its forward progression to about 8.5 $m\,s^{-1}$ from 253 degrees. It was just before this period, between 2330 and 2345 UTC, that a hook echo was first noted in the reflectivity signature from the lowest scans of the KTLX WSR-88D radar and a brief F0 tornado was produced near Thomas, OK.

At 2347, two areas of weak circulation were at both low and middle levels of the storm (Fig. 3.5). At a height of 1 km, one area of vertical vorticity was in the updraft region along the inflow of the gust front [two maxima near (36 km, 30 km)]; another area was in larger reflectivity further west [near (31 km, 35 km)]. interior to the storm behind the hook area of higher reflectivity collocated with the first. Note that at this time the storm had just entered the dual-Doppler lobe and erroneous features are likely present along the far western edge of the analysis, such as the downdraft region near (28 km, 34 km) in Fig. 3.5f.

By 2355, the storm had moved into better dual-Doppler coverage and the double hook echo structure at 1km in reflectivity was more apparent, with a mesocyclone associated with the more eastern of the two hook echoes (vertical vorticity of $10 \times 10^{-3} s^{-1}$) at 1 km (Fig. 3.6e). At 6 km, this mesocyclone was collocated with the bounded weak echo region (BWER) overlapping the strongest updraft velocities and its vertical vorticity had increased to $40 \times 10^{-3} s^{-1}$, almost double the maxima 8 min earlier (Fig. 3.6d and f).

The next analyzed volume scan began at 0016 and encompassed the tornadogenesis of the first F2 tornado. At the 1 km level, the mesocyclone increased in areal extent, become elongated with a southwest-to-northeast orientation, and grew in strength with vertical vorticity values increasing to greater than $2 \times 10^{-2} s^{-1}$ (Fig. 3.7). A single hook echo replaced the two hook echoes seen previously at 1 km and it became more wrapped up, as reflectivity increased to as high as 60 dBZ in the rear flank downdraft (RFD). The updraft has two pronounced maxima along the gust front at 1 km and both of these maxima extended upward through middle levels of the storm, peaking near $7.5 - 8$ km at about 50 $m\,s^{-1}$.

The behavior of the storm at the time of tornadogenesis, as described above, differs slightly from previous studies. Often, as described, for example, by Burgess and Lemon (1976), Dowell and Bluestein (1997), Steiger et al. (2007), and Lemon (2009) the storm appears to weaken in several aspects at the time of tornadogensis: overall reflectivity decreases, the mid-level updraft weakens, storm top altitude falls, and there is a smaller reflectivity deficit in the BWER. However, unlike the storms observed by those studies, the 29 May 2004 supercell actually appeared to strengthen over this period, including an increase in updraft size and speed at low-levels and

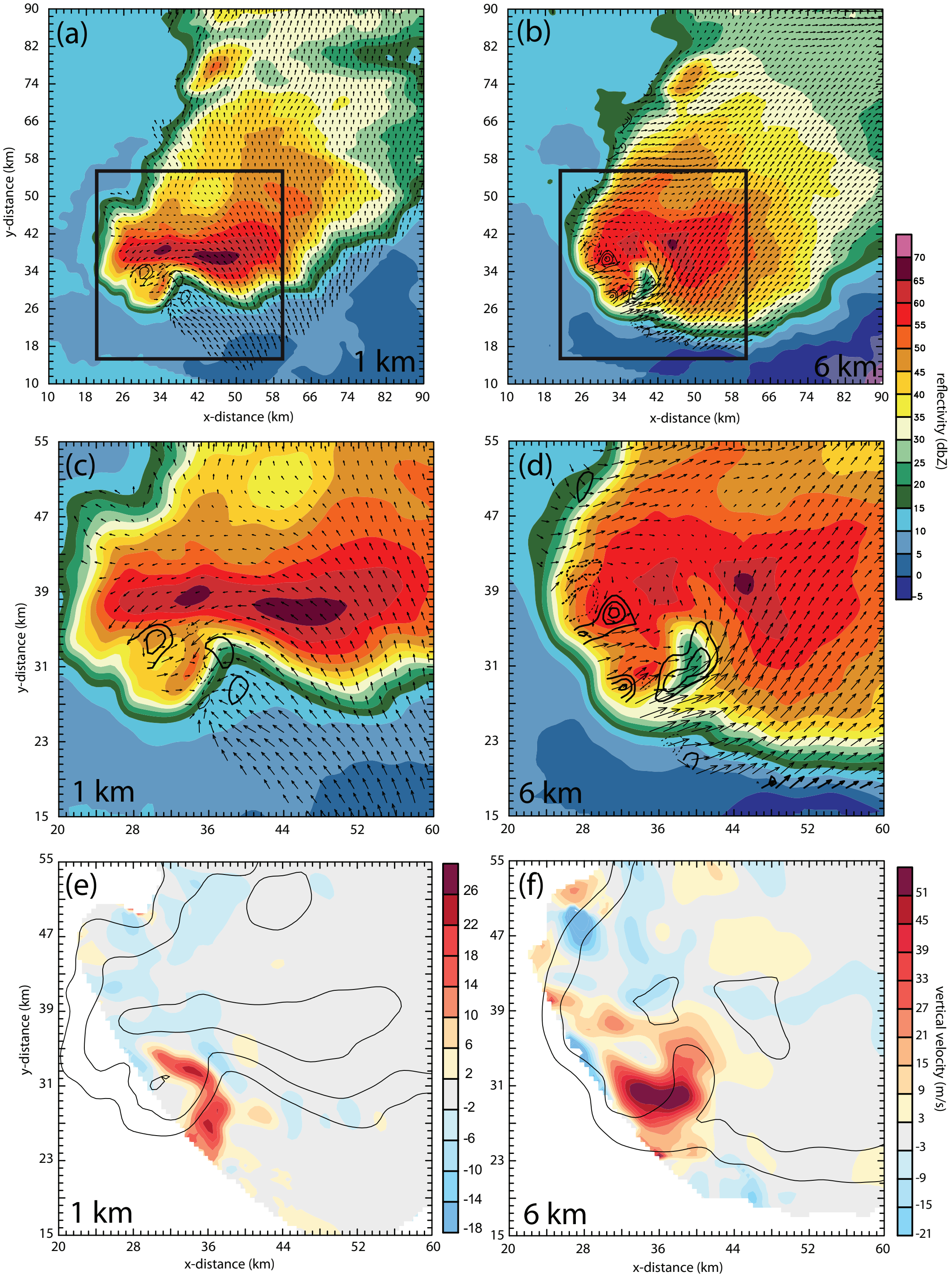

Figure 3.5: (a-b) Reflectivity and dual-doppler synthesized ground-relative horizontal wind vectors at 1.0 and 6.0 km AGL at 2347. (c-d) Reflectivity, wind vectors and contours of vertical vorticity every $10 \times 10^{-3} s^{-1}$, beginning at $10 \times 10^{-3} s^{-1}$ for the area with the box in panels a and b. (e-f) Vertical velocity (color fill) and contours of reflectivity, starting at 20 dBZ.

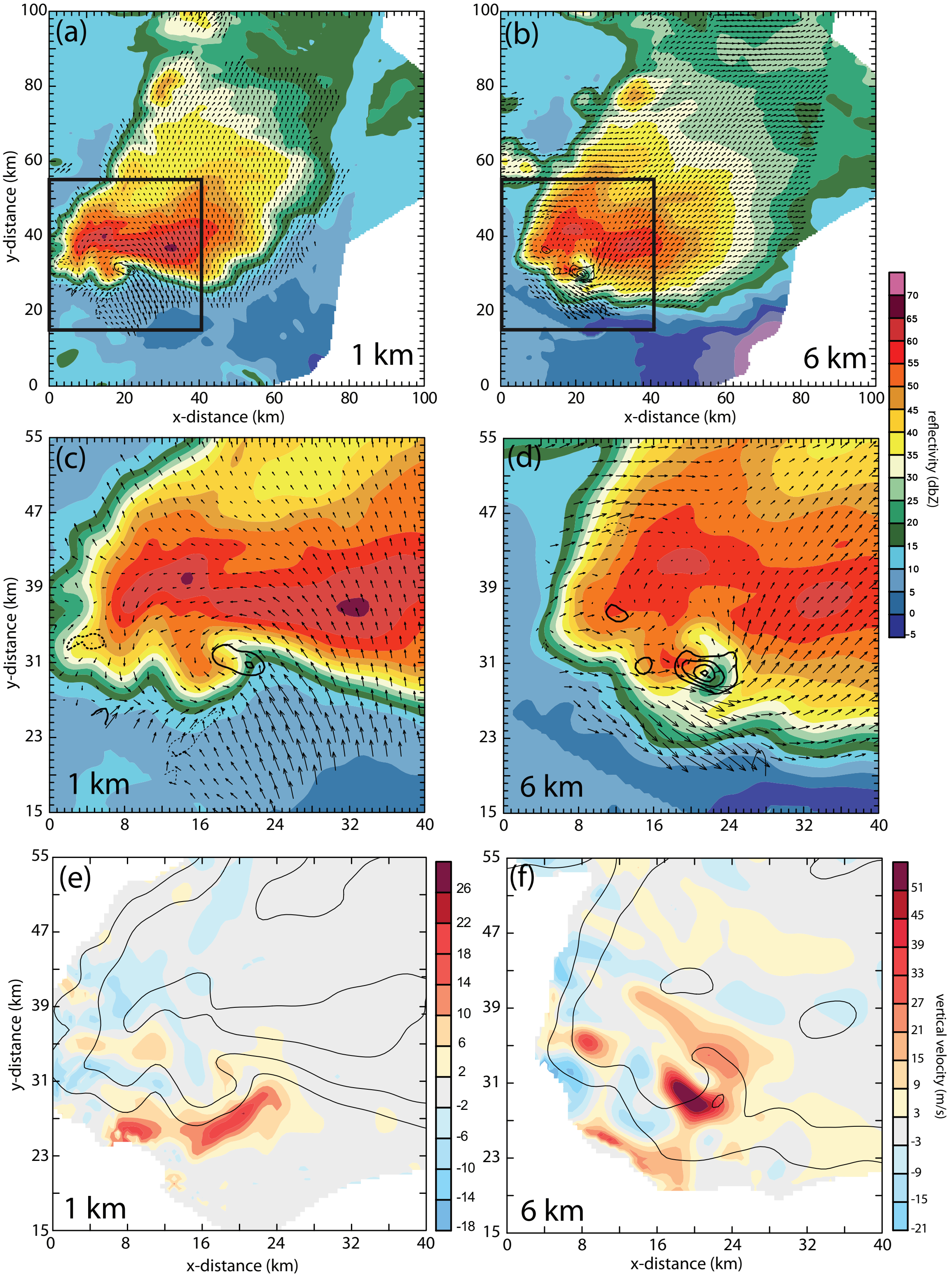

Figure 3.6: Same as Fig. 3.5 except at 2355 UTC.

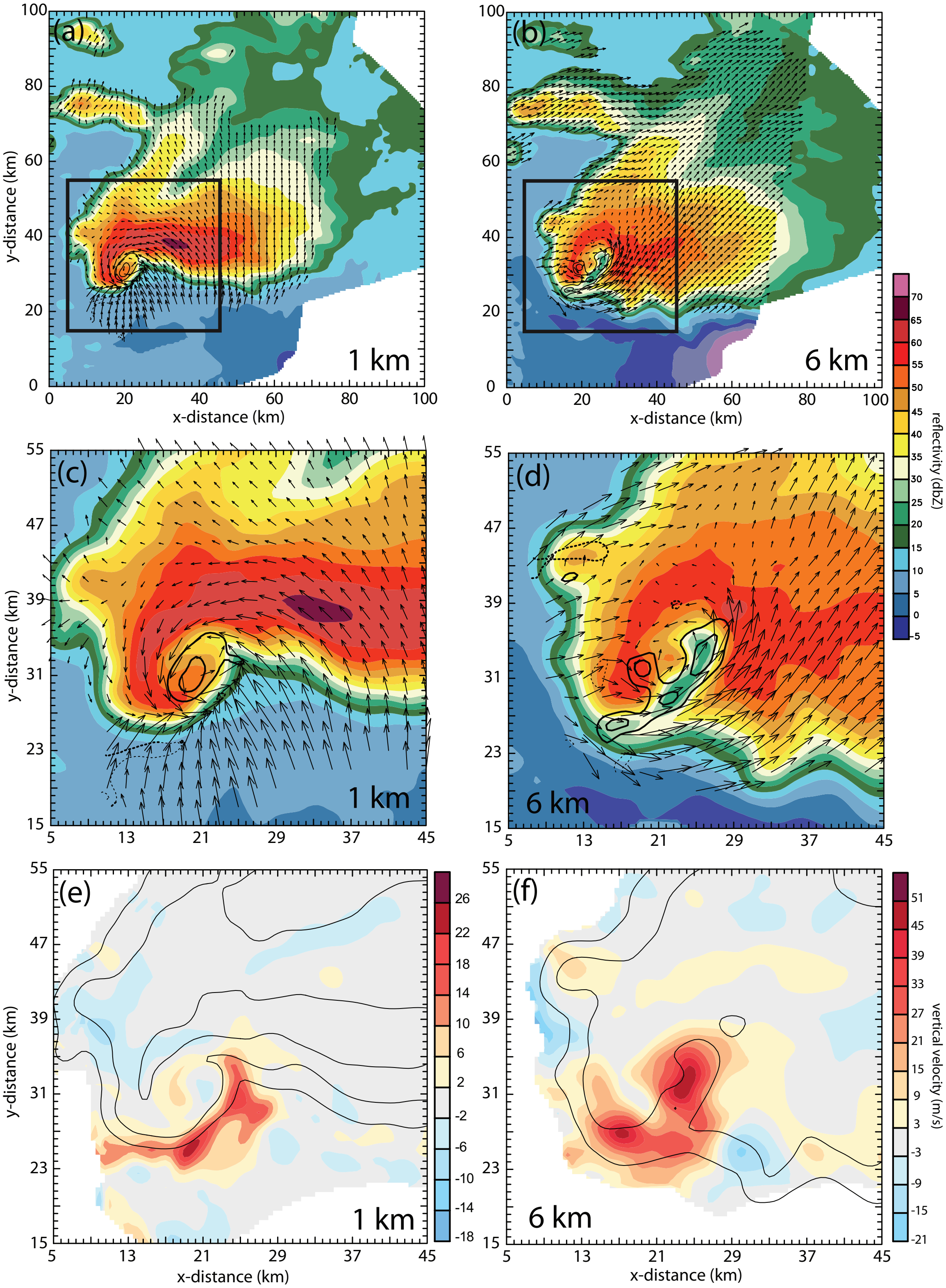

Figure 3.7: Same as Fig. 3.5 except at 0016 UTC.

increased size of the mid-level updraft and BWER with an increased reflectivity deficit in the BWER.

The supercell continued to strengthen between this analysis and the next analysis at 0027, when the tornado was still on the ground. Storm motion during time period was slightly north of due east, at about 12 $m\,s^{-1}$ from 276 degrees. The hook echo continued to become more wrapped up by higher reflectivities with the mesocyclone taking on a symmetric shape (Fig. 3.8). By 0027, vertical vorticity in the mesocyclone had increased to greater than $4 \times 10^{-2} s^{-1}$ at 1 km and greater than $3 \times 10^{-2} s^{-1}$ at 6 km. At low levels, the main updraft extended along the gust front, but remained strongest on the east side near the inflow notch. At mid-levels of the storm (Fig. 3.8d and f), the maximum updraft speed increased to almost 60 $m\,s^{-1}$ between 6 and 9 km, coincident with the BWER, just east of the main mesocyclone, but the updraft maxima on the southwest side [(17 km, 27 km) in Fig. 3.7f] decreased. The RFD pushed almost to the eastward edge of the gust front, and the resulting convergence possibly contributed to the intensification of the low-level mesocyclone. At 1 km, the vertical vorticity maximum was embedded in larger reflectivities within the hook echo near the boundary between the updraft and downdraft (Fig. 3.8c and e). At 6 km (Fig. 3.8d and f), the vorticity maximum was almost directly above the low-level maximum, but there was also a secondary maximum in the BWER, overlapping the region of largest updraft speeds.

The next analysis at 0038 shows that the mesocyclone continued to wrap up further and the updraft weakened somewhat. The maximum vertical velocity at both 1 and 6 km increased to greater than $5 \times 10^{-2} s^{-1}$, and at low levels the mesocyclone was mostly in weak updraft near the RFD (Fig. 3.9). [Unfortunately, parts of the storm were now on the edge of the dual-doppler analysis as a result of the extreme height of the storm and its proximity to the mobile radars. The volume scan did not reach storm top at the southern edge. Values in this area that may be suspect have been removed.] The mesocyclone at both low and mid-levels of the storm exceeded $30 \times 10^{-3} s^{-1}$. The maximum values of vertical velocity were at 8-10 km, with peak values of about 55 $m\,s^{-1}$.

By the 0052 analysis (Fig. 3.10), the mesocyclone had become completely occluded. At low-levels, it was fully within the RFD area. At middle levels, it was separate from the new BWER and northwest of the main updraft region. At mid-levels a new area of vertical velocity was co-located with the BWER region, inside and near the region of greatest updraft speeds. It appears that the storm mesocyclone exhibited a typical cyclic development as the old circulation became enveloped by the storm core, a new one formed ahead of the occluding hook echo, along the gust front. Peak values of vertical velocity were approximately 55 $m\,s^{-1}$, extending between 7 and 10 km.

3.2 Lightning Density and Charge Structure Relative to Structure of Reflectivity and Winds

The highest densities of lightning activity occurred near, but mostly outside the regions of of larger updraft speeds and the corresponding region of weaker reflectivity. Because charge is expected to be produced during graupel growth, one might expect considerable charge and lightning in the regions of larger concentrations around the updraft, as observed here. It is also expected that the magnitude and shear of the storm-relative wind are key in determining the lightning location relative to storm structure. Each of the sections below will describe various features of storm charge and lightning relative to storm structure as seen from the dual-Doppler analyses. In particular, how flashes differ in size and shape in various parts of the storm and how patterns of peak density of lightning change depending on layer or height within the storm will be examined.

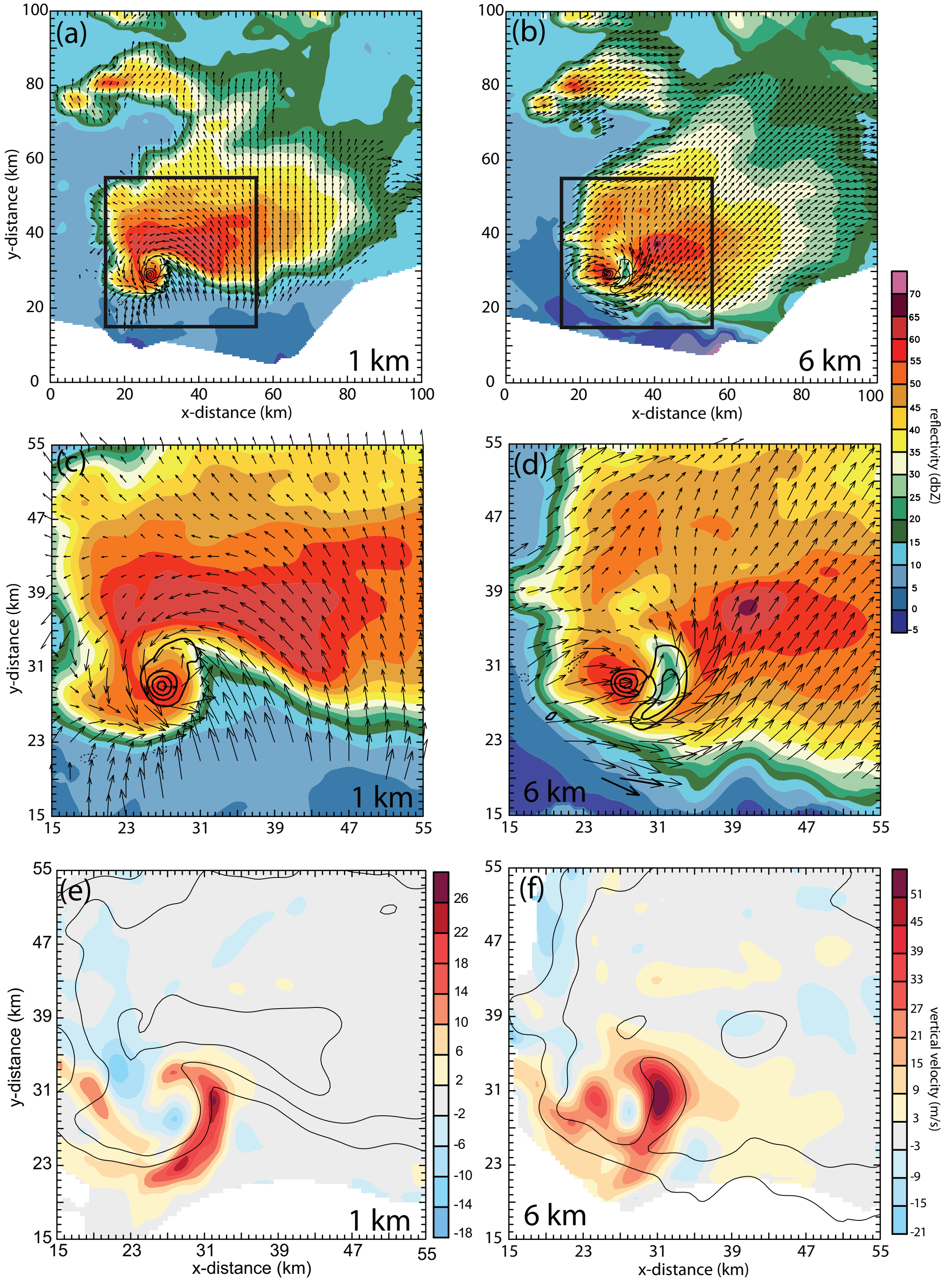

Figure 3.8: Same as Fig. 3.5 except at 0027 UTC.

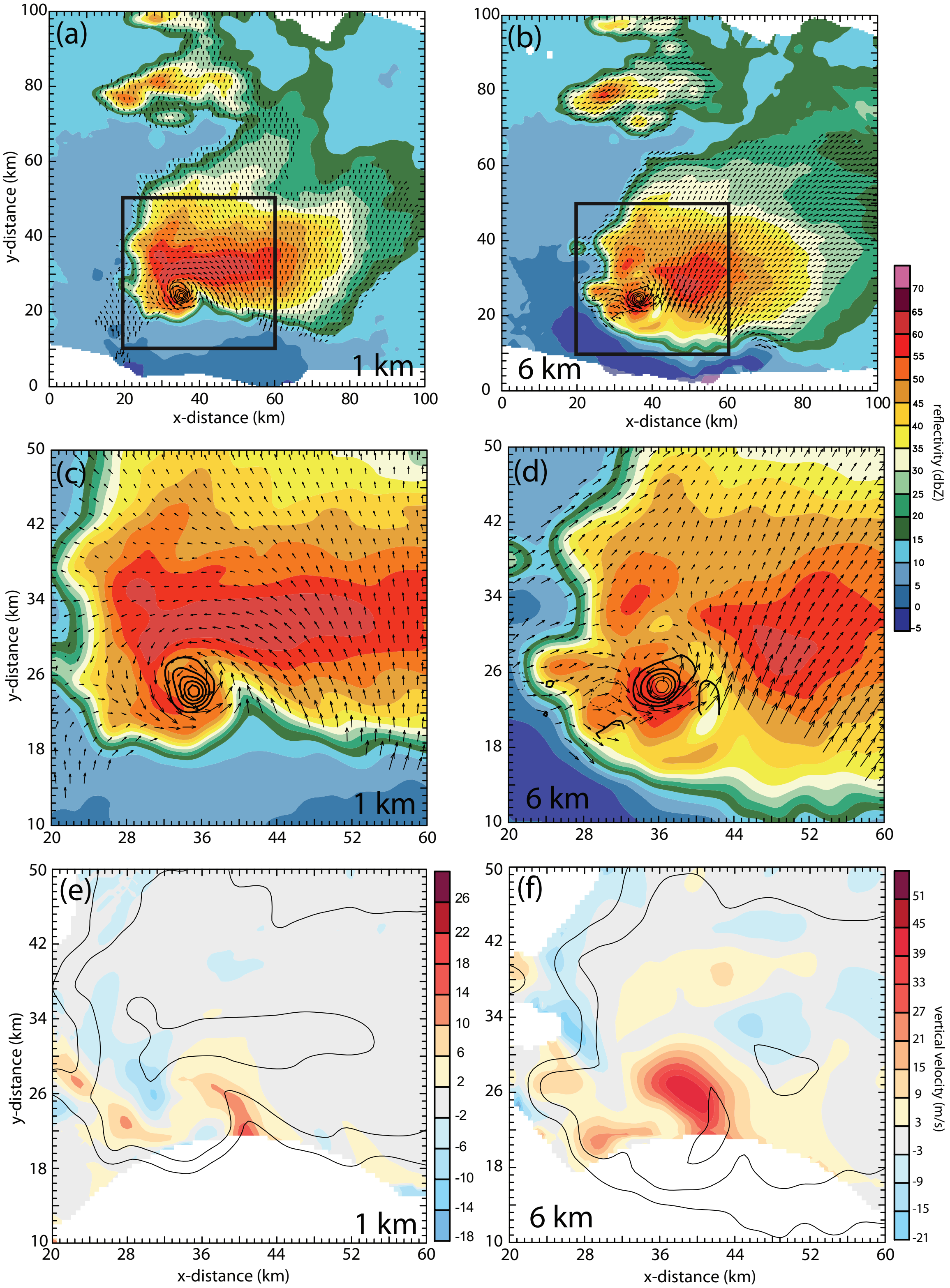

Figure 3.9: Same as Fig. 3.5 except at 0038 UTC.

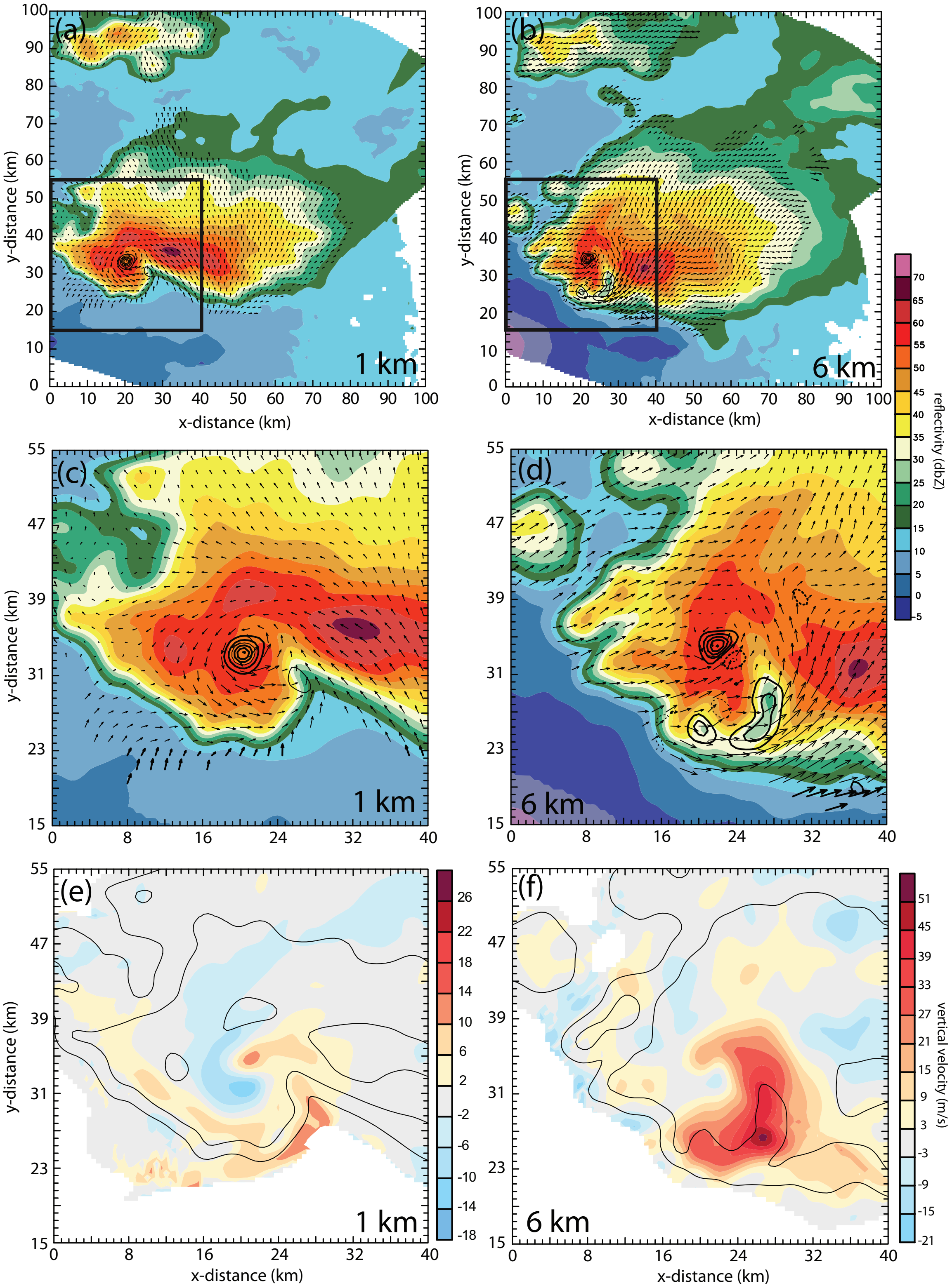

Figure 3.10: Same as Fig. 3.5 except at 0052 UTC.

3.2.1 Lightning Density in Vicinity of Updraft Region

If hydrometeors become charged by noninductive charge exchange during rebounding collisions between riming graupel and cloud ice, as is commonly believed now, then it is natural to expect the greatest charging rates to be in the region surrounding and just downshear from regions in which the greatest number of rebounding collisions are occurring. Because actively riming graupel implies a mixed-phase region with supercooled liquid water, the greatest charging rates would be expected in and around updrafts. Two features in the distribution of lightning in the 29-30 May 2004 supercell illuminate the relationship with updrafts further: first, the absence of lightning collocated with the updraft area and BWER, and second, the existence of lightning in the overshooting top, directly above the main updraft core. Both will be discussed further below.

3.2.1.1 Lightning Holes

Lightning holes (Krehbiel et al. 2000) represent lightning free areas within convection containing large updraft velocities (likely at least 30 - 45 $m\,s^{-1}$). Due to the strong updraft, little charge actually is allowed to accumulate in this area and as such, little lightning actually occurs. For the most part, the lightning hole tends to be a transient feature 5-6 km in diameter lasting at most 20 consecutive minutes (Wiens et al. 2005; Zhang et al. 2004; MacGorman et al. 2005). Likewise, the lightning hole seen during the 29 May 2004 storm is also a somewhat transient feature most notable at mid-levels of the storm where relatively few precipitation-sized particles exist in the updraft core. However, unlike many studies which noted a lightning hole for no more than 20 minutes, it is present throughout the majority analysis period discussed in this study, though it does vary in size. The feature itself is three-dimensional in nature and can get lost if one tries to force it into two-dimensions through a plan plot of the total lightning density encompassing all heights of the storm. This is especially true when there is lightning in the overshooting top, much of which lies directly above the lightning hole.

Throughout the analysis period (2347-0052 UTC) some degree of a lightning hole or lightning weak region exists. Fig. 3.11 gives a consistent representation of the lightning hole through three dual-doppler analysis times: 2355, 0016, and 0027 UTC. The diameter of the lightning hole remained between 7 and 12 km throughout the time period. Unlike the lightning hole in 6 Apr 2003 supercell analyzed by Steiger et al. (2007), the lightning hole in this case typically depicted a similar pattern in reflectivity as the BWER for the 29 May supercell extended much higher (above 10 km) in the storm. Similar to the storm observed by to McCaul et al. (2002), the hole itself was consistently co-located and extending slightly downshear from the BWER, though the exact shape of the hole differs somewhat from that of the BWER (Fig. 3.11). The main updraft area remained generally upwind form the lightning hole and not directly collocated with it as found in previous studies. Typically updrafts of at least 20-25 $m\,s^{-1}$ were contained within the region, but the strongest updrafts tended to lie just upshear of the lightning hole. Perhaps the best kinematic correspondence lies with the horizontal vector field at 10 km (also the height of the maximum LMA activity). Clearly evident in Fig. 3.11 are the divergence and circulation around the lightning hole in each of the analyses, suggesting that charged hydrometeors were actually getting swept out from and around this area.

Individual flashes do not depict any typical behavior surrounding the lightning hole, other than tendency to avoid the region containing the lightning hole. The flashes generally curved left or right when reaching the hole instead of maintaining what appeared to be a previously straight trajectory towards the center. Flashes in the vicinity of the hole either were initiated on the interior region near the edge of the the lightning hole and progressed either around the hole or outward or were initiated in the outer regions and moved inward. They did not appear to have any proclivity

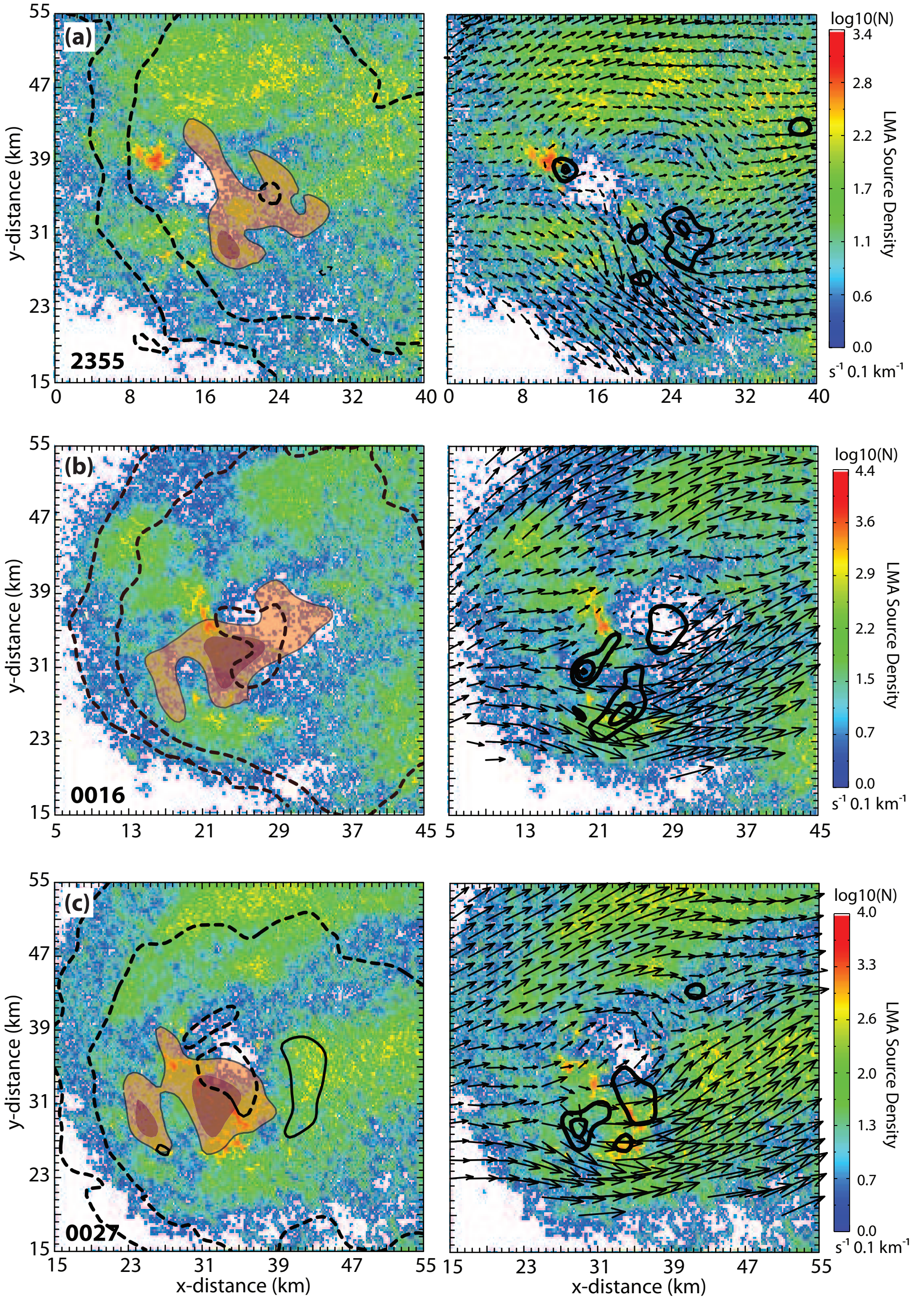

Figure 3.11: Doppler radar data at 10 km superimposed on LMA density of VHF source points from 6 to 15 km (color fill, density scale is a log scale). (a) 2355 UTC (b) 0016 UTC (c) 0027 UTC. Left panels include reflectivity (dashed contours at 20, 40 dbz, solid contour 60 dbz) and vertical velocity (fill at 20 and 40 $m\,s^{-1}$). Right panels show horizontal ground-relative wind vectors and vertical vorticity every $10 \times 10^{-3} s^{-1}$, beginning at $10 \times 10^{-3} s^{-1}$.

toward moving in any particular direction, upshear or downshear, surrounding the lightning hole. However, the longest flashes were typically initiated either on the south-southeast or north to northeast side of the lightning hole. One could interpret, therefore, that faster charge buildup was occurring nearby in the corresponding regions surrounding the updraft core.

Most flashes contained in the region of the peak updraft, southwest of the lightning hole, tended to be quite short in duration. Generally these flashes contained only 1 to 5 mapped points in length, although occasionally a longer flash moved through the region (2-3 per min, on average). Given the general low density of sources in the region of the peak updraft, it is possible that these are not actually “flashes” in terms of light and energy dissipation. They may be more of a spark or some kind of low current discharge. However, the region on the periphery of the updraft core contains a consistently large number of flash initiations as well as a higher source density in general. This remains true throughout the analysis and is consistent with the idea that the highest levels of noninductive charging are on the periphery of the updraft core (Kuhlman et al. 2006b).

3.2.1.2 Lightning in Overshooting Top

High altitude lightning, occurring at 15-16 km, above the region of the lightning hole, has been noted in previous supercells occurring over LMA networks (Krehbiel et al. 2000). Increasing trends of lightning in the overshooting top are expected to correspond generally to rapid vertical growth of the storm, which would likely be related to increasing updraft velocities and increasing updraft mass flux. In addition, upward pulses of lightning into this region have been theorized as a possible precursor to tornado onset.

In the 29 May 2004 storm, the majority of high altitude VHF sources seem to occur almost continually with at least 6 to 8 separate VHF source points occuring

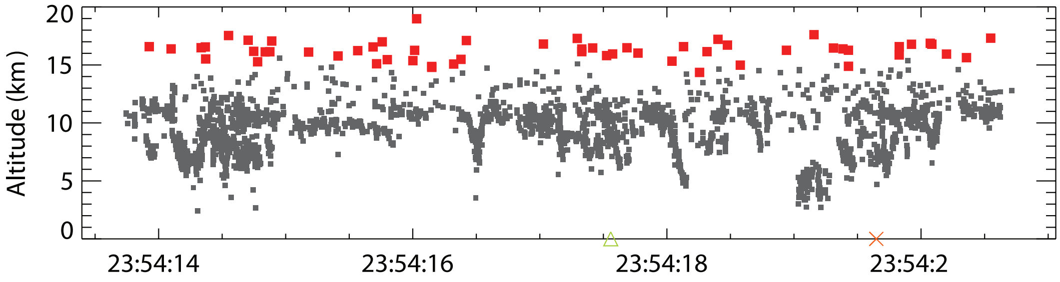

Figure 3.12: Time-height plot of VHF radiation points occurring in the seven second period beginning 2354:14 UTC. Points occurring in the overshooting top are highlighted in red, all other points in grey.

every second (e.g., Fig. 3.12). These singular VHF sources are too far apart in time and space to be associated in a single flash with each other, each failing criteria of distance or time for associating it with other points in a flash. A comparison with dual-doppler data indicates that these isolated points are concentrated directly above the main updraft and BWER, as well as downshear of the updraft near the 20 dBZ reflectivity contour (Fig. 3.13).

It is unknown why exactly the electrical activity in this region consists of only isolated VHF sources. However, because these source points were located near cloud top and along the edge of the large reflectivity gradient above and downshear from the oveshooting top, it is possible that the activity is occurring in a region of charge produced in the updraft, possibly in conjunction with a screening layer charge (Taylor et al. 1984; Proctor 1991). If screening layer charge is folded into the storm by turbulent eddies, it could decrease the distance to charge advected by the updraft and therefore increase the electric field. It is likely that these upper discharges are caused at least in part by the lower threshold for electric field breakdown at these heights (e.g., Marshall et al. 1995, 2005). Although there is uncertainty about the details of lightning initiation, all mechanisms suggested thus far require a lower threshold of electric field magnitude at higher altitudes. For example, as shown in Eqn 3.1 below

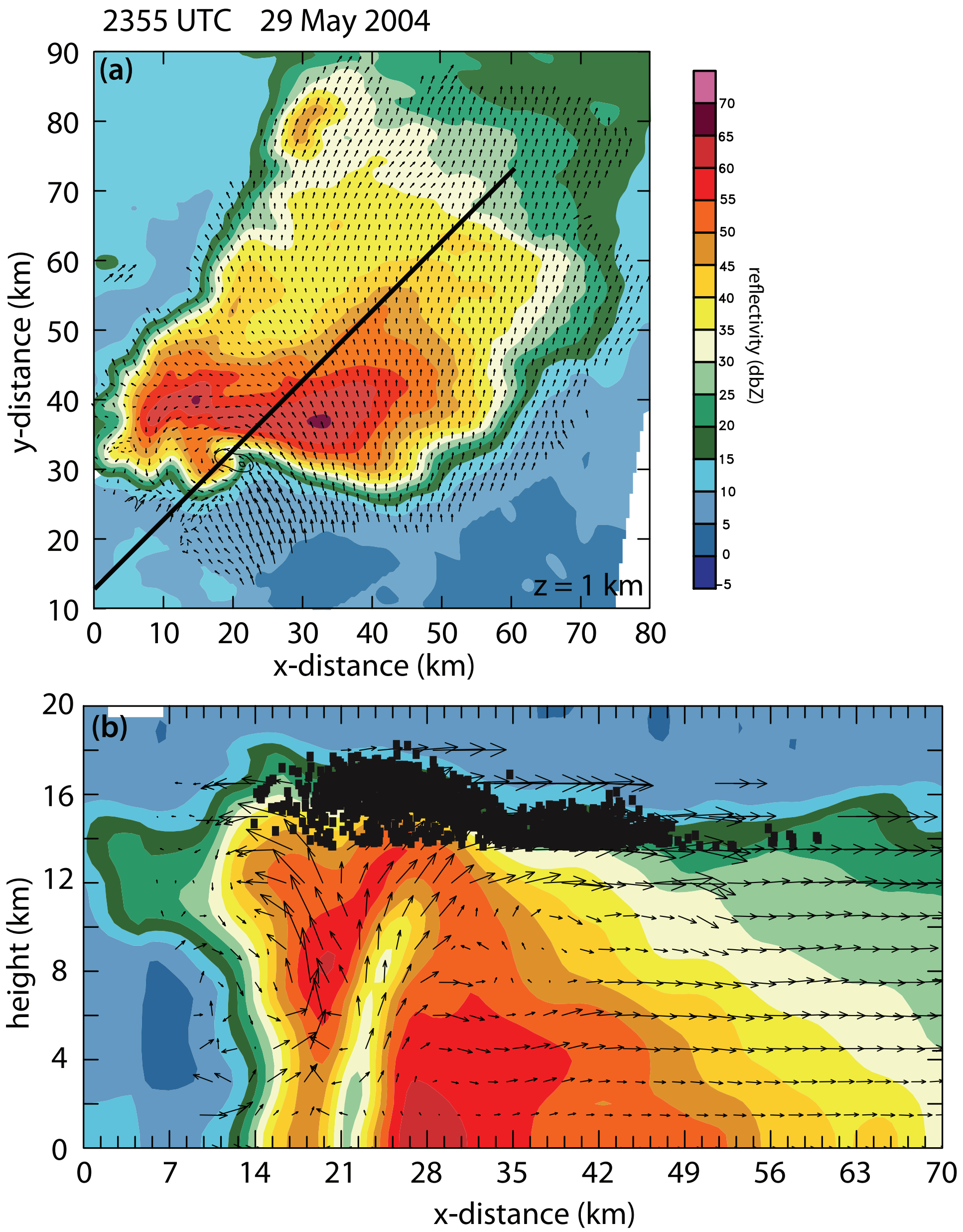

Figure 3.13: VHF radiation points overlaid on reflectivity and wind vectors from the dual-Doppler analysis at 2355 UTC (a) Plot at 1km. x-z cross-section of panel b is along black line. (b) VHF radiation points occurring 3 min 20 sec period beginning 2353:50 UTC overlaid on x-z cross-section. Only LMA VHF singleton points occurring above 14 km are shown.

and Fig. 3.14, the breakeven electric field decreases with increasing altitude due to the decreasing density of air, as described by McCarthy and Parks (1992):

$$E_z = 167\rho_z, \tag{3.1}$$

$$\rho_z = 1.208 \exp\left(\frac{-z}{8.4}\right). \tag{3.2}$$

The EFM sounding launched at 2346 UTC into the back of the storm core had magnitudes approaching and surpassing the threshold of the breakdown electric field in altitude ranges (Fig. 3.14). In particular, at the point the sounding reached its maximum altitude at around 12 km, the measured electric field magnitude exceeded the the breakeven electric field, which was approximately 50 $kV\ m^{-1}$, there. At the altitude of these continual VHF emissions (15-18 km), the breakeven electric field decreases to 33-23 $kV\ m^{-1}$. One of the goals of the numerical storm simulations is to examine whether the combination of conventional noninductive charging, screening layer charge, and reduced threshold of the breakeven electric field can account for the unusual discharges near storm top.

As stated earlier, periods of intensification or increased updraft strength can possibly be diagnosed by periods of high lightning activity revealed by time-series plots of lightning density (e.g., Fig. 3.15). It is evident in Fig. 3.15 that there are periods when additional increases in lightning activity above 16 km do occur, either as an extension of lightning from the upper storm area or completely within this overshooting top area only. Through most of the two-hour period, there is some lightning above 16 km, except during the 10-min period beginning just before 2330. The highest density of upper VHF sources clearly occurs at approximately 0010 UTC, with continued large densities of upper sources through 0040 UTC, after which the maximum altitude of lightning begins lowering again. The 0010 UTC impulse occurs just before the F2 tornado touched down NW of Geary, OK at 0017 UTC and the higher source

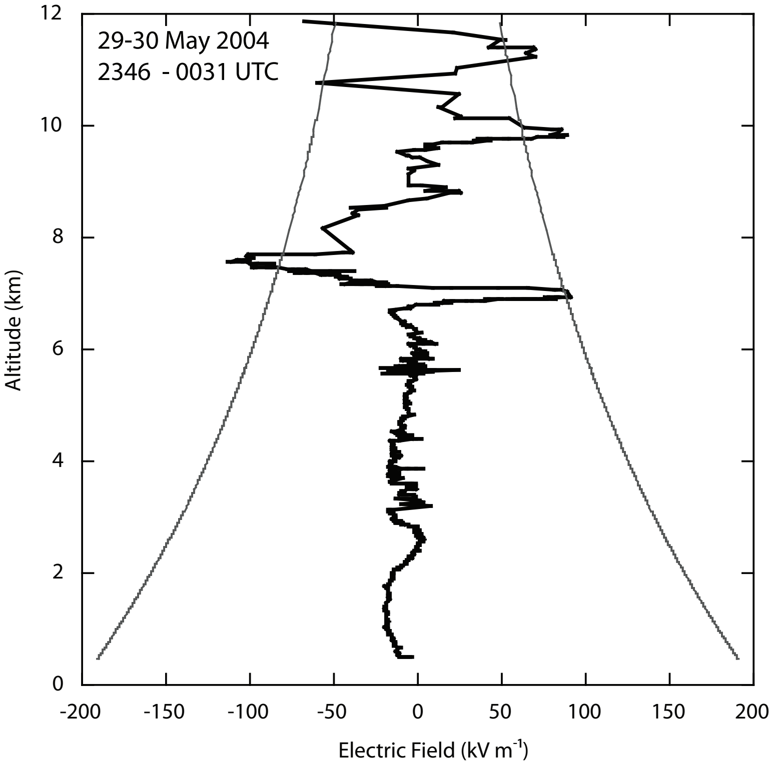

Figure 3.14: Electric field sounding through thunderstorm on 29 May 2004 and breakeven electric field as calcuated by Eqn 3.1. Balloon was launched at 2346 and reached maximum altitude of 12 km at 0031 UTC.

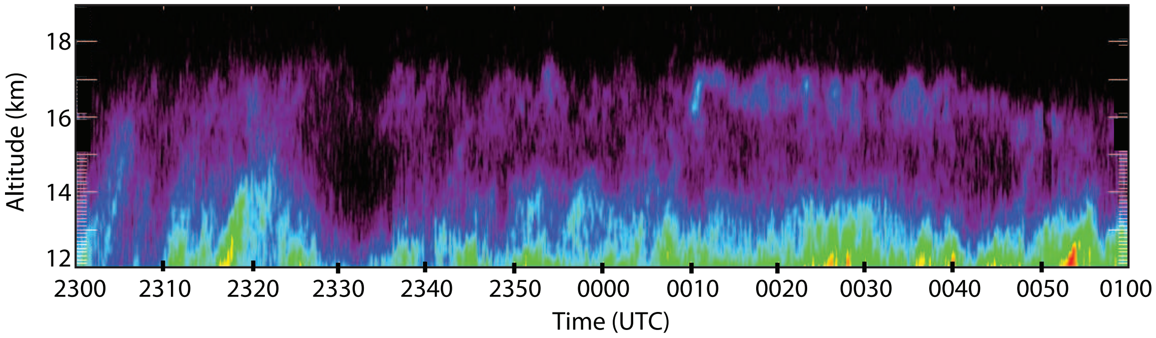

Figure 3.15: Time-height plot of VHF radiation points occurring above 12 km during the two hour period beginning 2300 UTC on 29 May.

density continued while the tornado remained on the ground and a second tornado formed at 0038 north of Geary. Note, however, that the first tornado spawned by this storm, a brief F0 tornado occurring near Thomas at 2330 UTC, began during almost a complete lull in electrical activity above 12 km, consistent with those studies suggesting a supercell collapse, especially in terms of storm top, at the time of tornadogenesis (e.g., Dowell and Bluestein 1997; Lemon 2009).

The peaks in overshooting top don't necessarily correspond to peaks in activity lower down in the storm. The 0010 UTC peak at 16 km did not have a corresponding increase lower lightning activity in the storm. Conversely, at 0052 UTC there was an increase in lightning around 12 km as well as an increase at lower levels, but little or no real activity above 16 km in the overshooting top. Furthermore, there typically is a minimum in VHF source density between 13 and 16 km and VHF sources above 16 km do not correspond systematically to flashes lower down. Thus, it appears likely that flashes contained in the overshooting top are a separate entity from those in the storm core just below.

Examination of the density of points at greater than 14 km accumulated over the 10 min period of 2340-2350 UTC compared with the dual-Doppler analysis centered at 2347 reveals that the largest density of points were within regions of updraft greater than or equal to 25 $m\ s^{-1}$ at 12-14 km (14 km level shown in Fig. 3.16a). The same result was found at almost all analyzed times, including the other two shown in Fig. 3.16. The horizontal position of the highest density of points in the upper area of the storm is within regions of larger updraft speeds. Several studies (e.g., Williams et al. 1989; Ziegler et al. 1991) have pointed out that the highest densities of charge in the vertical will tend to occur near a balance level as the updraft decreases with height to the point that particles no longer rise. Typically between 16 and 18 km, the region containing these upper LMA points took on a rounded-cap appearance in overshooting top, with the highest point directly above the region of largest, most vertical updraft and tilting downward east of the overshooting top, along the vertical gradient in reflectivity (Figs. 3.13 and 3.17 a-c). The north-south cross-sections in Fig. 3.17d-f best depict the separation of the peak activity in the overshooting top into a double pronged region, one corresponding to the divergent flow out of the updraft with a higher area of larger VHF density to the north where updraft speeds tend to be largest and a secondary peak in somewhat weaker updraft speeds to the south (Fig. 3.17 d-f). [The relationship with the southern maxima cannot be confirmed for 0010-0020 UTC period because the edge of the dual-Doppler analyses one of the mobile radars did not scan to storm top across part of the storm (see south side of storm in Fig. 3.17e).]

3.2.2 Vertical distribution of lightning

Throughout the hour and a half of the analysis when the storm was in 3D LMA range, the majority of lightning was initiated near 10-11 km in height (Fig. 5.13). Compared to other storms, even other supercells, it is unusual for such a large number of flashes to be initiated at this height. This is likely due to the continued strength of the updraft throughout the analysis period. As discussed earlier, each of the dual-Doppler analyses computed vertical velocities in the main updraft through the mid-levels of the storm (6-10 km in height) of at least 45-60 ms^{-1} throughout the

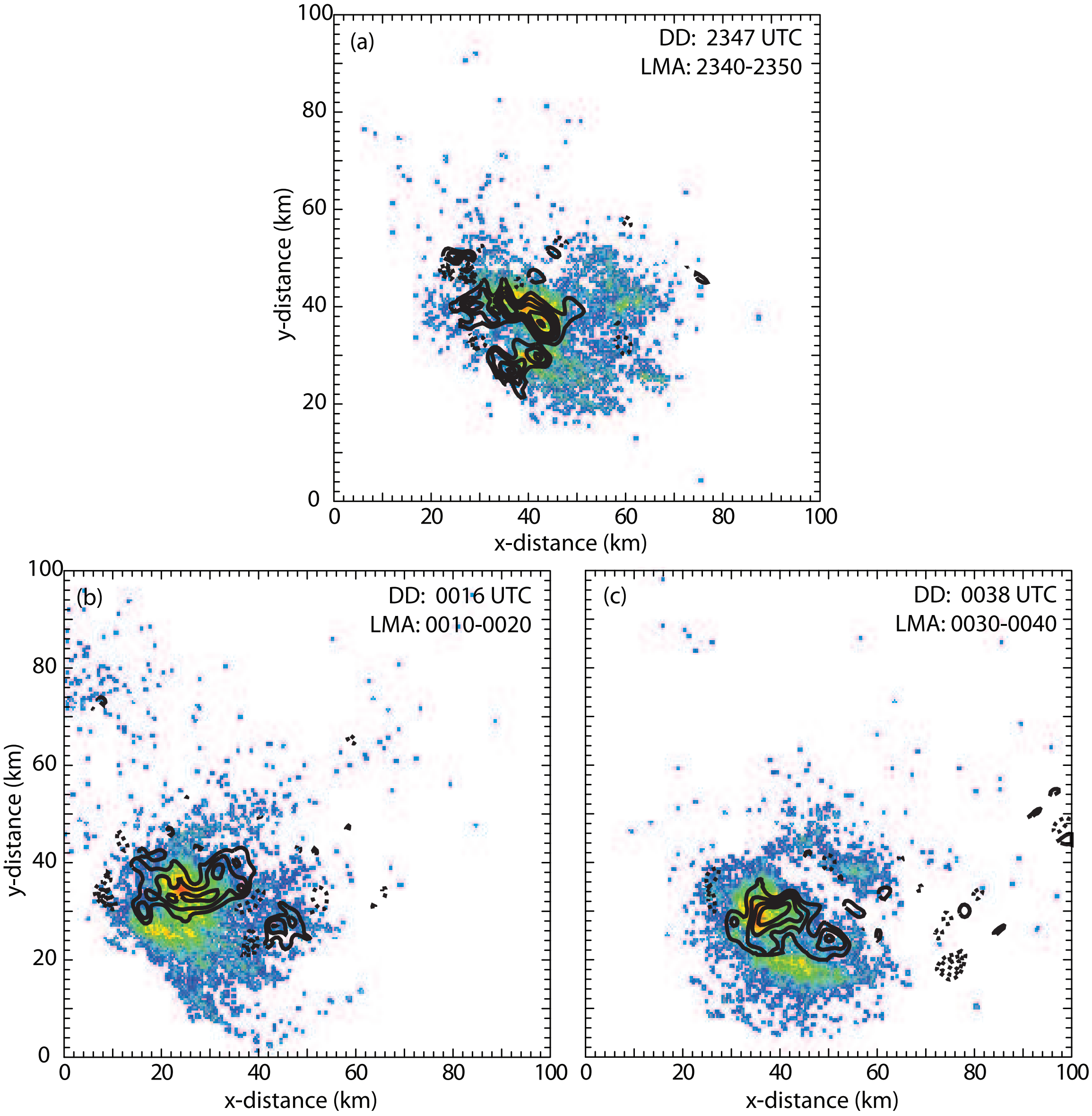

Figure 3.16: Density of LMA sources for 10 min periods above 14 km, contours of vertical velocity determined from dual-Doppler at 14 km analysis overlaid (times of each displayed on plot). Solid contours represent positive vertical velocity every 10 ms^{-1} starting at 15 ms^{-1}. Dashed contours are negative, beginning at -15 ms^{-1} every -10 ms^{-1}.

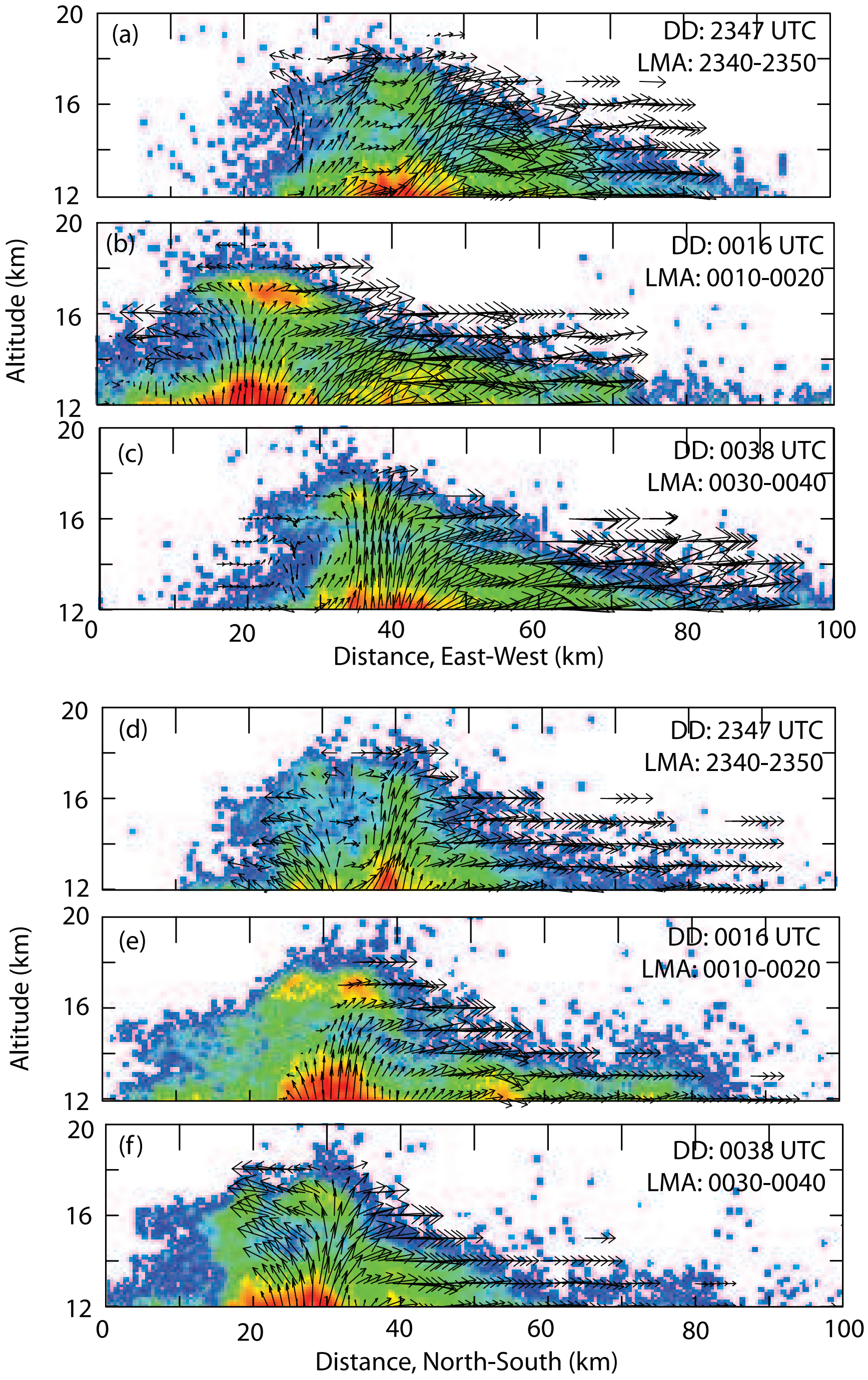

Figure 3.17: Top: X-Z cross-section of LMA source density for 10 min periods above 12 km, wind vectors from dual-Doppler analysis overlaid. Bottom: as above but for Y-Z cross-section. (a,d) LMA, 2340-2350 UTC, dual-Doppler 2347. (b,e) LMA, 0010-0020 UTC, dual-Doppler at 0016 UTC. (c,f) LMA, 0030-0040 UTC, dual-Doppler at 0038 UTC.

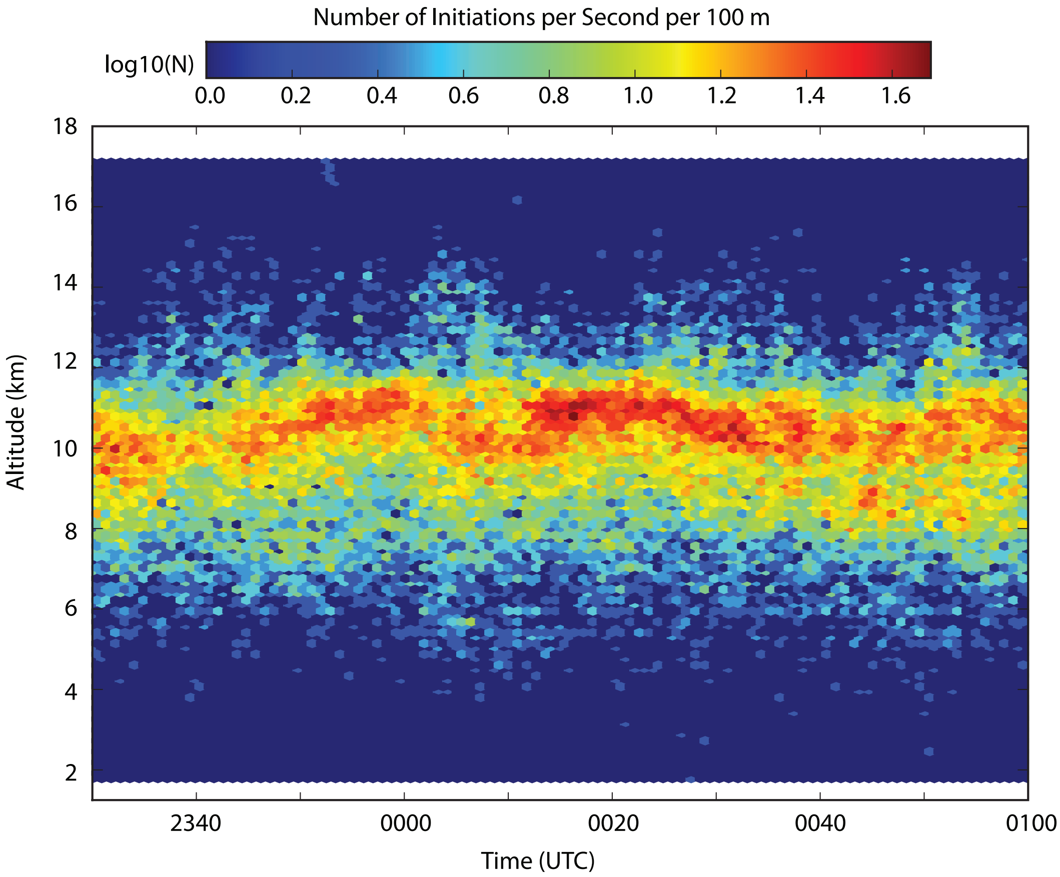

Figure 3.18: Time-height plot of lightning initiations per second per 100 m. Only includes flashes having at least ten mapped VHF sources.

analysis period. Following a small lull and decrease in initiation heights from 0003-0011 UTC, the highest concentration of flash initiations occurred just after 0012-0020 UTC, immediately before and during the time of the tornado northwest of Geary, OK. A similar trend is observed in the time-height plot of total VHF sources as well, as both the number and height of max sources increases at 0013 UTC (Fig. 3.19). Between 0025 and 0035 UTC flash initiations followed by VHF source density increased at 8 km, providing a bi-level structure to the density patterns in Figs. 5.13 and 3.19. The storm continued to have a bi-level maxima throughout the rest of the analysis period through 0100 UTC.

The distribution of lightning relative to the storm changes with altitude according to the trajectories of charged particles within the region (Fig. 3.20). At lowest levels of

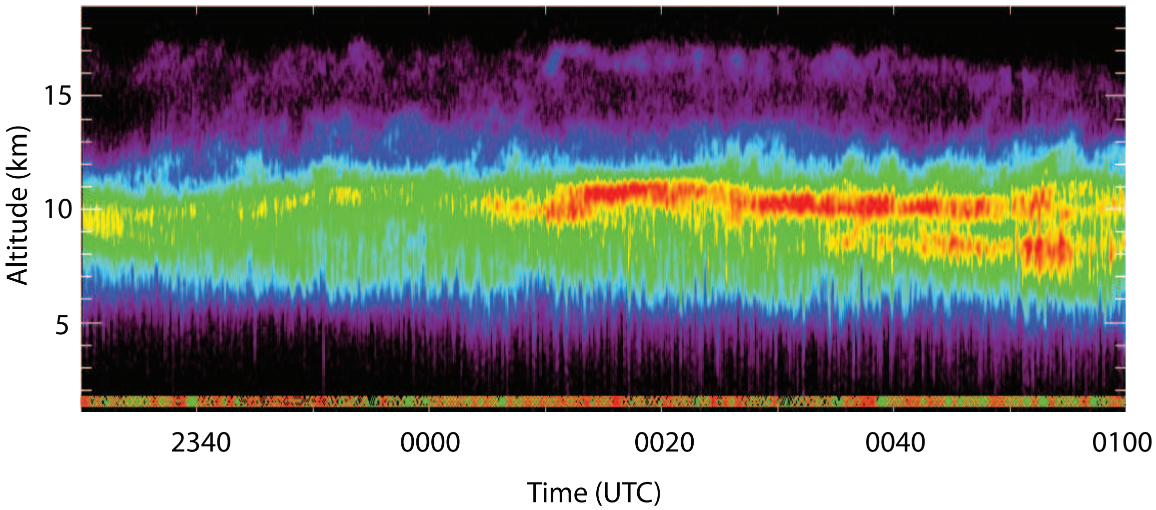

Figure 3.19: Time-height plot of lightning VHF sources from the LMA per second per 100 m.

the storm (below 6 km), where the inflow was from the south, peak areas of electrical activity were contained predominately within the RFD area within the hook echo and to a lesser degree in the FFD, north-northeast of the main updraft, as charged particles were brought down into these regions from mid-levels. Between 6 and 9 km, lightning activity has greatly expanded into the FFD area, following the movement of charged particles NE of the main updraft. From 9-12 km, the density of VHF source density pattern has expanded due east from the main updraft and charging area, following the direction strong upper level flow at these heights. At the upper extent of the storm, approaching 15 km, the VHF activity had a pattern of lower density similar to 9-12 km, but the majority of activity was contained predominately in the overshooting top as discussed in Sec. 3.2.1 above.

3.2.3 Flash size relative to location

There is a distinct difference in the frequency of flashes and the number of source points per flash goring from near the storm core in areas of high turbulence out to the far anvil region (Fig. 3.21). Lightning in the storm core or near the main updraft

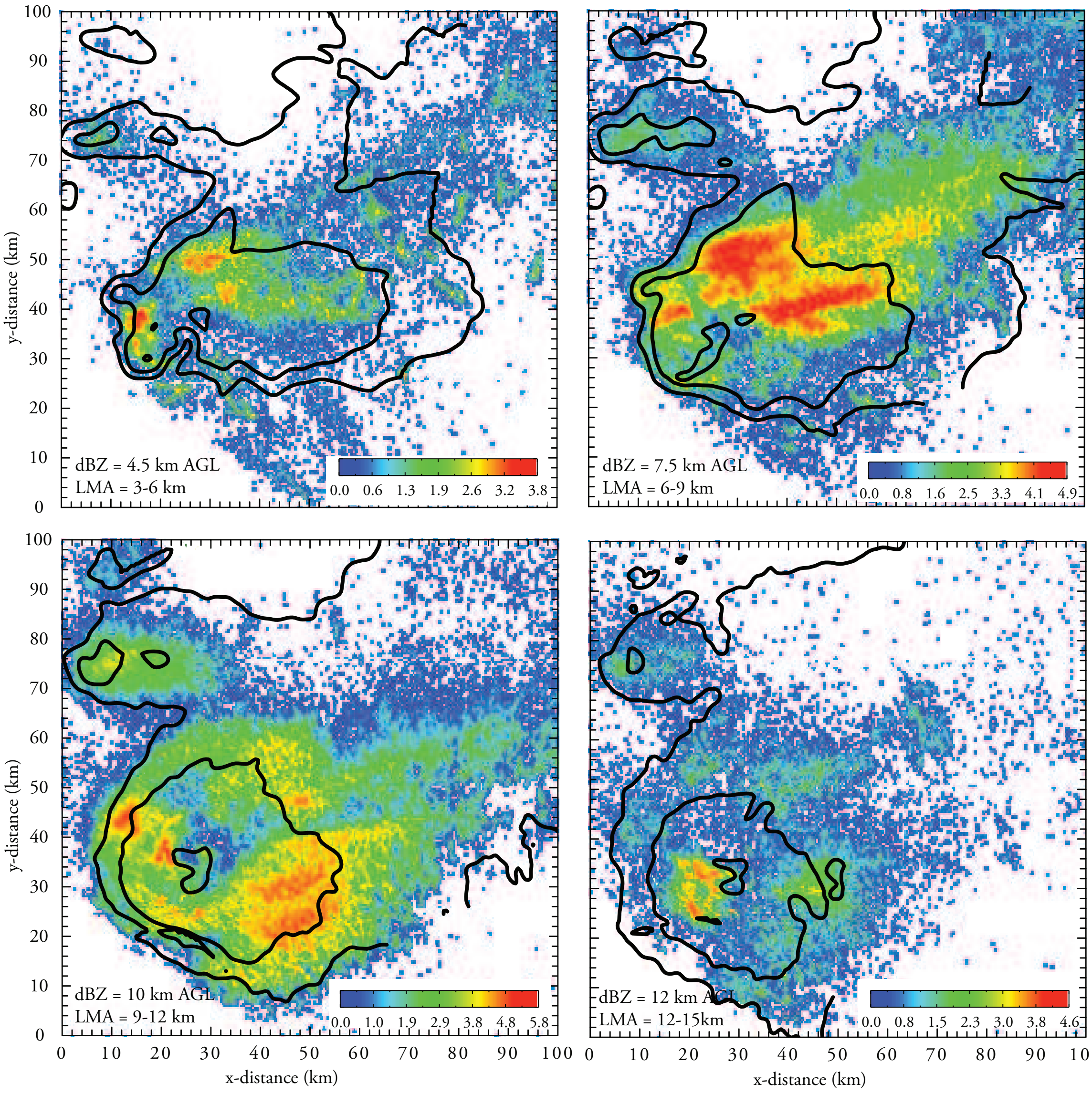

Figure 3.20: Reflectivity (20, 40, 60 dBZ) and LMA activity at 0016. (a) dbz at 4.5 km; LMA 3-6 km. (b) dbz at 7.5 km; LMA 6-9 km. (c) dbz at 10 km; LMA 9-12 km. (a) dbz at 12 km; LMA 12-15 km.

tends to be shorter (10-50 points total or less) and quite frequent. The extent of flashes mapped by the LMA within this region was usually no longer than 5-10 km horizontally and 3-5 km vertically. In contrast, lightning in the anvil quite frequently contained over 100 points per flash, spanned over 30 km in horizontal extent, and was quite a bit less frequent (see the next chapter for further details about anvil lightning in this storm). Typically (though not always), flashes tended to increase in horizontal extent and decrease in frequency as distance increased from the storm updraft.

Fig. 3.21 depicts a typical distribution of flashes across the storm core and anvil; this distribution was consistent throughout the 1.5 hr analysis period. The smallest flashes were most prevalent in the hook echo region, the backshear anvil, the updraft area, and as discussed earlier the overshooting top. Farther downshear from the main updraft and through the FFD towards the anvil the flashes got longer in length, both in terms of number of points and the distance covered by each flash.

It is likely this is due, at least in part, to the level of turbulence in each of these areas. As mentioned earlier, in the hook echo and main updraft area, flashes tend to be shortest. Since this is the predominant region of active charging combined with larger levels of turbulence due to updraft/downdraft interaction, it is likely that pockets of high charge density of opposite sign lie in close proximity to each other. So, while the threshold of the electric field may be easily reached to cause initiation, leaders have little room to travel before reaching a region of opposite polarity charge. However, further downshear from the updraft core, trajectories were smoother and charged regions would be expected to be more horizontally extensive. Larger, more continuous charges region allow flashes to have longer spatial extent (e.g., MacGorman et al. 1981; Williams 1985; MacGorman and Rust 1998). The size of flashes and layers or pockets of charge will be further tested in Ch. 5 through numerical simulations.

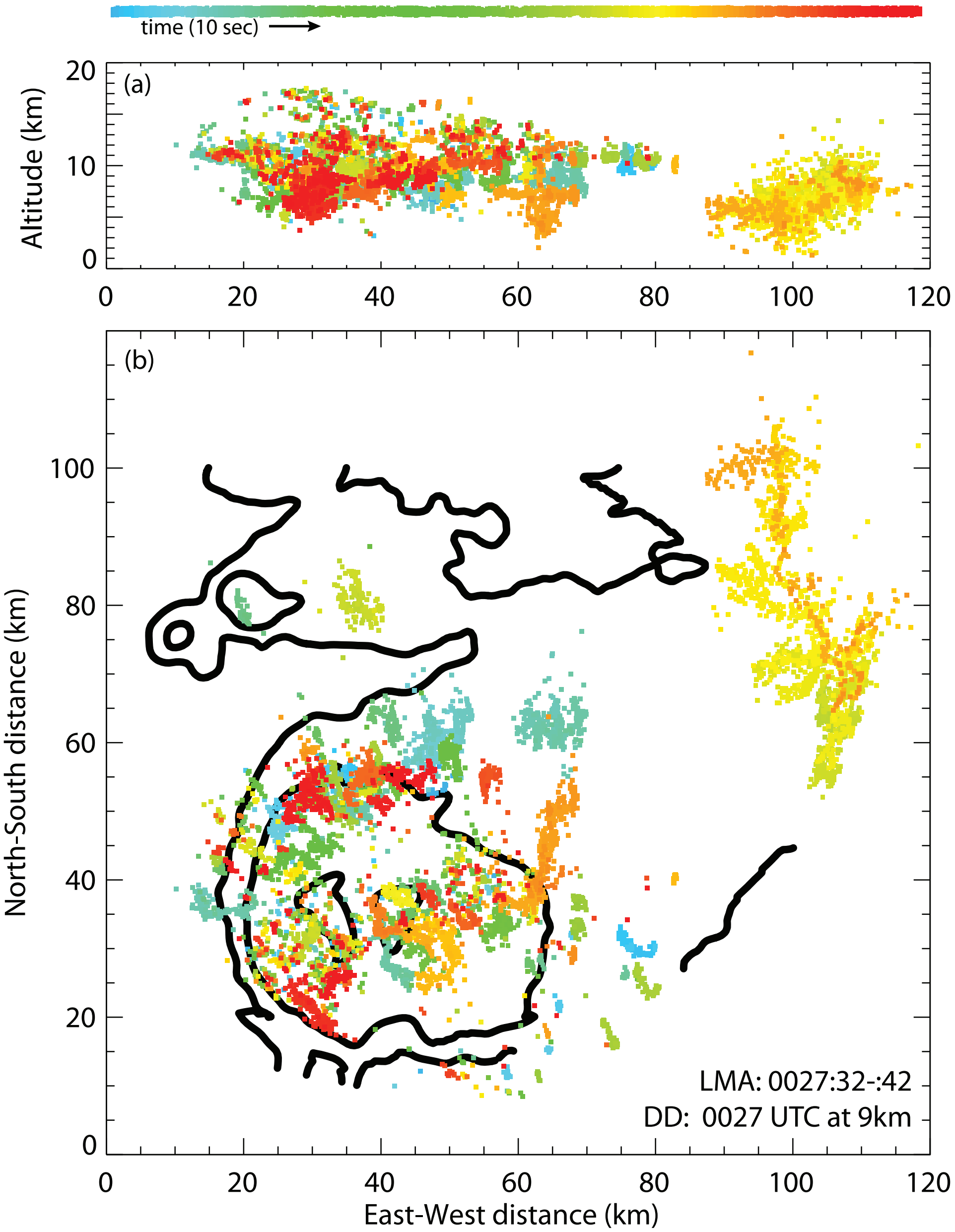

Figure 3.21: 10 seconds of LMA data beginning at 0027:32 UTC, color coded by time according to bar at top of figure. (a) x-z projection of LMA points across storm. (b) x-y projection of LMA points and reflectivity contours (every 20 dBZ) from dual-Doppler analysis at 9 km beginning at 0027 UTC.

3.3 Evolution of Lightning relative to evolving storm characteristics

3.3.1 Total Flash Rate

In high flash-rate storms such as this one, it is difficult to delineate some flashes occurring close together in space and time, so it is important not to focus on exact flash rates, but instead to examine trends in flash rates and the approximate value of the flash rates (Wiens et al. 2005; Murphy 2006; MacGorman et al. 2008b). As discussed above, within the storm core many flashes occurred in close proximity to each other. Many of these flashes contained fewer than ten VHF points per flash, quite a few with only 1-2 points per flash. Because isolated points can be an artifact counted by the LMA instrumentation, flashes with fewer than ten points were omitted from our analysis of flash rates. It is also likely that any automated flash sorting algorithm used will lump together some multiple flashes occurring in close proximity (time and space), as happens frequently in a very active storm core such as this one, into one flash. So, it is probable the exact number of flashes per minute computed by our analysis is only approximate. However, as done by Wiens et al. (2005), multiple algorithms have been tested, and while the specific number may change slightly, the overall trends remain the same. Furthermore, the flash rates from all algorithms were consistent in showing flash rates of at least 200 flashes per min throughout the analysis period. A minimum in flash rates occurred around 2340 UTC, followed by an increase and leveling off of flash rates through 0000 UTC and a dramatic increase in flash rates at 0015 UTC (Fig. 5.16) (just prior to the touchdown of the tornado NW of Geary, OK at 0017 UTC).

Previous modeling and observational studies have found that correlations of the total flash rate with graupel volume and updraft mass flux were significant in a high plains supercell (Wiens et al. 2005; Kuhlman et al. 2006b). The dual-Doppler

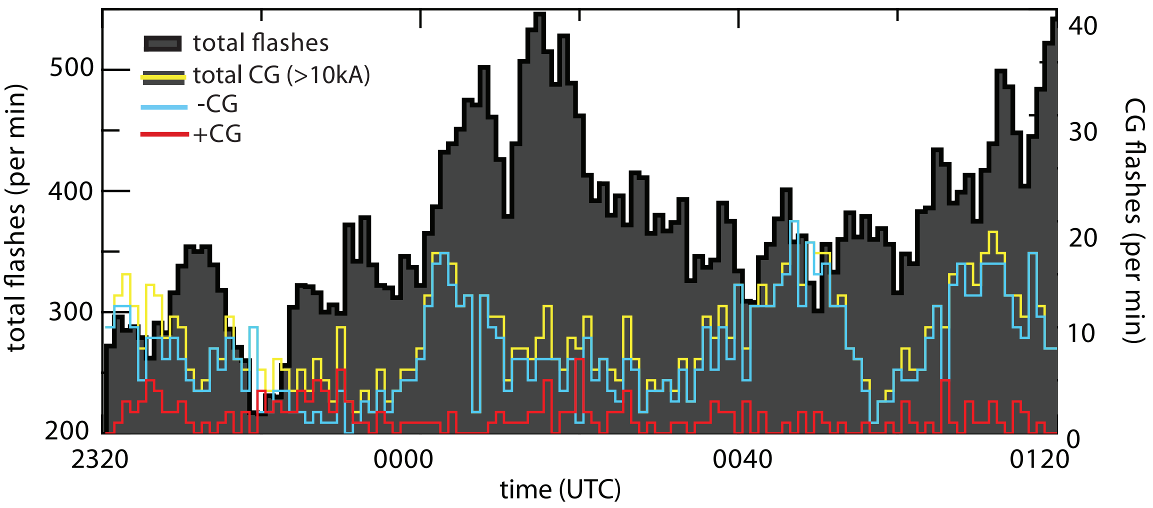

Figure 3.22: Lightning flash rates from 29 May 2004. Black shaded area represents the total flash rate determined from the LMA (scale on the left y-axis). Yellow indicates the total CG rate, including both positive and negative CG flashes having an estimated peak current greater than 10 kA from the NLDN. Blue line indicates the negative CG rate, red, the positive. The scale for all CG rates is on the right y-axis.

velocities were used to calculate the updraft mass flux through the storm for vertical velocities greater than 10 $m\,s^{-1}$ (Fig. 3.23). The updraft mass flux ($MF, kg\,s^{-1}$) through a level, i, was calculated according to Emanuel (1994):

$$MF_i = \rho_i \sigma_i w_i \tag{3.3}$$

where ρ is the density of air, σ, the areal coverage of the updraft (m^2), and w_i, the vertical velocity ($m\,s^{-1}$) at the ith height.

Although we do not have enough continuous data for statistical correlation, one can note that the overall flash rate for the storm (Fig. 5.16) increases at the time there is an increase in the updraft mass flux throughout all heights of the storm between 2355 and 0016 UTC and decreases following a decrease in the updraft mass flux at 0027 (Fig. 3.23). The maximum in updraft mass flux is around 10 km for all times, consistent with height of maximum flash initiation and LMA VHF activity (though the increase LMA activity at lower levels after 0035 is not accounted for

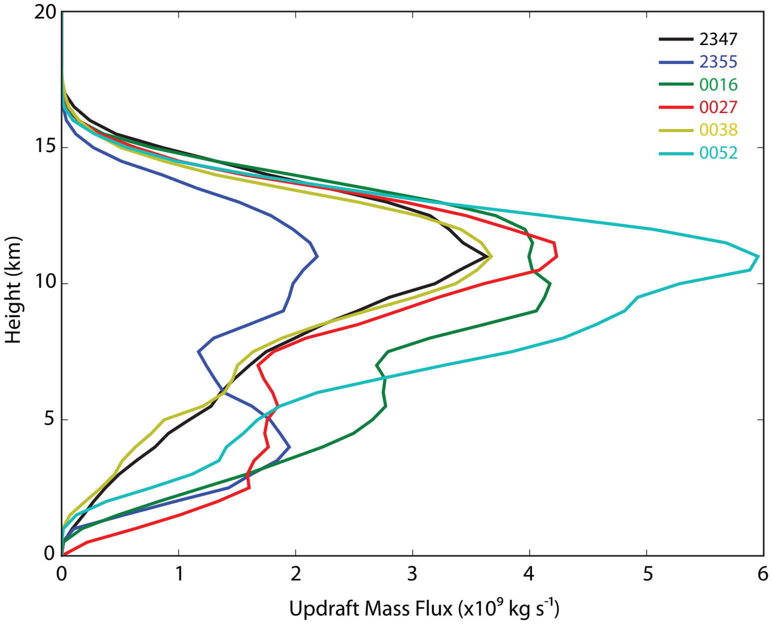

Figure 3.23: Updraft mass flux ($kg\,s^{-1}$) for w > 10 $m\,s^{-1}$ across all heights for each dual-Doppler analysis. Calculated according to Eqn. 3.3.

by this limited data). Overall, this remains consistent with the relationship between convective-scale charge separation and updraft mass flux expected if noninductive charging dominates thunderstorm electrification (e.g., Takahashi 1978; Carey and Rutledge 1996; Saunders et al. 2006). This storm consistently contained maximum vertical velocities around 45-55 $m\,s^{-1}$ at heights of 6-10 km and therefore, also like past studies, continues to show little correlation between maximum updraft velocity and flash rate. In summary, this suggests that the rate of thunderstorm electrification is not so much proportional to the speed of hydrometeors, but to the number and their collision rates with cloud ice.

3.3.2 Cloud-to-ground flash rate and percentage of total flashes

As seen in Fig. 5.16, cloud-to-ground lightning in the 29 May 2004 storm was typically dominated by negative cloud-to-ground (CG) flashes. The only exception to that was during 2340-2350 and 0025-0035 UTC periods during which the negative

CG flash rates dropped rapidly to equal that of the positive CG flash rate (Fig. 5.16). At it's maximum, the CG flashrate approached almost 20 per minute, but the overall average was closer to 10 per min. The peaks in CG flash rate occurred around 0005, 0045, 0110 UTC, occurring before, during, and just after tornadic activity. As found previously (MacGorman et al. 1989; MacGorman and Nielsen 1991), the CG flash rate showed no consistent correlation to tornadogenesis or other types of severe weather at the ground.

Throughout most of the analysis period, the percentage of CG flashes remained less than 3 to 5 percent. In general, strong storms typically have a low percentage of CG flashes (e.g., Rust et al. 1981) due to the large amount of charge centered at higher altitudes that has been lofted by the large, intense updrafts with these storms (MacGorman et al. 1989; Stolzenburg et al. 1998; Boccippio et al. 2001; Wiens et al. 2005; Steiger et al. 2007). However, the percentage of CG flashes for this storm is quite small for any storm, including other documented supercells. The maximum CG percentage during the analysis period occurred at 0045 UTC. The −CG flash rate increased rapidly, doubling from 10 to 20 flashes per minute at a time when the overall flash rate decreased to only 300 to 350 flashes per minute (maximum of 7% CG flashes). This increase in the CG rate occurred just after an increase of LMA activity in lower regions of the storm at 0035 and continues through 0050 UTC (Figs. 3.19 and 5.16). It appears that the development of a lower charge area, at least one strong enough to participate in lightning activity, contributed to the storm's overall ability to produce CG lighting.

3.3.3 Charge regions

As discussed in Ch. 2, regions containing flash initiation points indicate where the electric field tends to be large, typically near the boundary or between opposite polarity regions. The persistent large number of initiations at an altitude of roughly

10 km points to that being a region of charge separation. The region above 10 km (likely composed of cloud ice and snow) contained a relatively consistent negative charge, while the region below 10 km (likely consisting of larger ice hydrometeors) contained predominately positive charge. Later, following the increase in the number of initiations between 8-9 km and the secondary maxima in source density just below that, a secondary region of concentrated positive charge seems to have formed at lower levels in the storm, producing at least four predominate regions of charge vertically. It is likely that while this is good conceptual model of the overall charge structure in terms of height for this storm, the actual charge structure was much more complex with pockets of opposite charge existing in close proximity horizontally as well as vertically. As stated earlier, flashes in the core of the storm were typically quite small, often contained less than 15 VHF source points per flash and extended no more than 5-10 km in total length; thus, determination of initial breakdown and direction of these flashes for charge analysis was problematic. Since we do not have additional detailed in-situ measurements of charge, further discussion will be deferred to the examination of simulations of the storm in Ch. 5. The charge regions as determined from the LMA analysis for the anvil region will be further discussed in the context of Ch. 4.

Chapter 4

Anvil Lightning

4.1 Introduction

Previous studies of lightning in anvil clouds have reported that flashes began in or near the storm core and propagated downwind into the anvil. It had been thought that flashes could not be initiated far downwind in the anvil, because anvil charge was thought to be produced mainly in the storm's deep updraft and to decrease with distance into the anvil. Here we report observations of the in-cloud development of lightning flashes in the anvils of two supercell storms, including the first observations of flashes that began in the anvil 30-100 km from the cores of the storms and propagated upwind back toward the cores. Interaction between charge regions in the two converging anvils of adjoining storms appeared to cause some of the distant flash initiations, but a local charging mechanism in the anvil likely also contributed to the flash initiations. All flashes that struck ground beneath the distant anvil transferred negative charge to ground instead of the positive charge usually transferred to ground there, an apparent consequence of the parent storm having an inverted-polarity electrical structure.

Substantial advances have been made in our understanding of lightning in deep convective regions and in the widespread stratiform precipitation that trails large storm systems (e.g., MacGorman and Rust 1998; Lang et al. 2004; Bruning et al.

2007; MacGorman et al. 2008b). However, lightning in anvil clouds has received far less attention. (The anvil is a layer of cloud that flows horizontally out from the upper part of the parent storm and can extend more than 100 km from the deep convection.) Though large electric fields are observed in anvils (e.g., Marshall et al. 1989), charge in the anvil has been viewed as originating primarily in deep convection and flowing passively into the anvil, with some contributions from environmental currents to anvil cloud boundaries and complications from lightning (e.g., Byrne et al. 1989; Dye et al. 2007). As will be discussed, however, in this study in agreement with and Dye and Willett [2007], it can be inferred from new observations that significant charging also occurs in the anvil, an inference likely having important implications for our understanding of anvil kinematics and microphysics. Most previous studies of anvil lightning analyzed only cloud-to-ground (CG) lightning channels below clouds, as observations of in-cloud lightning structure have been scarce. CG studies found that anvil flashes striking ground near the storm core can lower either positive charge (+CG flashes) or negative charge (−CG flashes) to ground, but those striking ground > 30 km from the core are almost always +CG flashes (Rust et al. 1981). Only one case has been reported in which there was a cluster of −CG flashes from the distant anvil (Bluestein and MacGorman 1998).

The scarcity of in-cloud lightning observations in anvils has been overcome recently with the advent of automated systems for mapping very high frequency (VHF) electromagnetic radiation sources (Thomas et al. 2004). A few subsequent studies [e.g., Wiens et al., 2005; Dye and Willett, 2007; Tessendorf et al., 2007] have reported the in-cloud development and structure of anvil lightning. These flashes all began in or near the storm core and propagated into the anvil, but the number of storms analyzed by these studies is very small. Here we report the lightning and electrical structure observed in the anvils of two supercell storms on 29-30 May 2004. These observations provide the first documentation of flashes beginning in an anvil several tens of kilometers from the storm core, instead of beginning in or near the storm core and propagating into the anvil. Besides having implications concerning anvil processes, these observations provide insight into situations under which distant anvil CG flashes are -CG flashes, instead of the +CG flashes usually observed there.

4.2 Observations from 29 May 2004

The Oklahoma Lightning Mapping Array (OKLMA) provided the in-cloud lightning data we have analyzed. Storm winds and precipitation were measured by two mobile, C-band Doppler radars (Biggerstaff et al. 2005), which were 30-40 km apart and took 2-3 minutes to complete a synchronized sector volume scan of the storm. See Chapters 2 and 3 for more information on the LMA and dual-Doppler analyses. Radar data were interpolated to a grid having 1 km horizontal spacing and 0.5-km vertical spacing by using a modified Barnes weighting scheme (Trapp and Doswell 2000) in the REORDER software package (Oye et al. 1995). The CEDRIC package (Miller and Fredrick 1998) was used for wind synthesis. Most lightning occurred in the deep convective cores of the storms, but many flashes occurred in the large anvils. The northern storm developed first and was already a supercell storm when our analysis period started. The southern storm began later, but overtook the northern storm and produced multiple tornadoes.

Our analysis began at 2255 UTC, when both storms were in the region of three dimensional lightning mapping coverage and the anvil of the southern storm was starting to overlap the anvil of the northern storm. Before 2255 UTC, all anvil lightning was associated solely with the northern storm. Most anvil flashes began in or near the main core of the northern storm and propagated into the anvil, as seen in previous studies (e.g., Marshall et al. 1989; Tessendorf et al. 2007b), but some flashes were initiated in the anvil of the northern storm $>$ 30 km from the storm core. [Distances from the core are measured from the eastward boundary of 30 dBZ reflectivity at 2-3 km above mean sea level (MSL).]

Between 2255 and 2325 UTC, lightning continued to be initiated in the distant anvil of the northern storm, but some of these flashes also began to involve part of the anvil of the southern storm. Lightning initiations migrated south from a region well inside the northern anvil to a region in which the northern and southern anvils merged and overlapped (e.g., Fig. 4.1). Of the ten flashes initiated > 30 km from the core during this period, five did not strike ground, and five were -CG flashes. The flashes propagated back toward the storm core through a midlevel layer of positive charge in each anvil, in reflectivity > 20 dBZ (Fig. 4.1). Channels propagating through the upper negative charge (the polarity of charge lowered to ground) were in the northern anvil only. Channels from flashes initiated in the distant anvil approached, but did not overlap flashes propagating out from the core.

The flash in Fig. 4.1 was the last to be initiated in the northern anvil > 30 km from the storm core. The estimated distribution of the charge involved in all anvil lightning 2320-2330 UTC (which included Fig. 4.1‘s flash) is shown in Figs. 4.2a,b and 4.3a. During this period, the southern storm was just starting to become a supercell storm. (By 2330 UTC, radar clearly detected supercell characteristics, including a rotating updraft.) The northern storm was weakening rapidly from its supercell stage, because the southern storm had started interfering with low-level inflow into the updraft of the northern storm.

The polarity of electrical structure inferred from lightning in the convective cores of both storms 2320-2330 UTC (an uppermost negative charge in a vertical tripolar or dipolar arrangement) (Figs. 4.2a,b; 4.3a) could be described as inverted from the usual polarity [e..g, Rust et al., 2005]. This structure clearly extended into the anvil of the northern storm. Midlevel positive charge also extended into the anvil of the southern storm, but little or no lightning involved upper negative charge in the southern anvil.

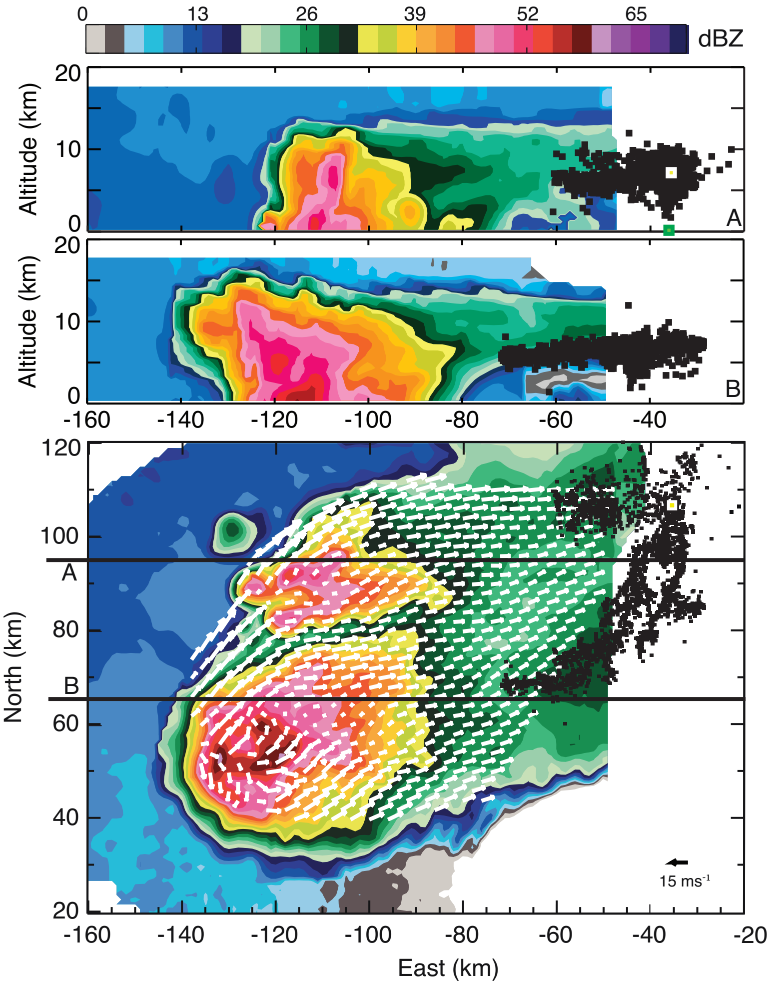

Figure 4.1: Mapped VHF sources at all altitudes from the flash at 2321:45.2-46.9 UTC, superimposed on reflectivity and synthesized horizontal winds from the SMART-R volume scan beginning at 2321 UTC. Yellow square marks flash initiation; green square, connection to ground. (Top) Vertical profile along line A, includes LMA points north of line A. (Middle) Vertical profile along line B, includes LMA points south of line A. (Bottom) z=8.3 km AGL.

As seen most clearly in the side-by-side distributions for the anvils shown in Fig. 4.3a, the upper part of the positive charge in the anvil of the southern storm was at the same altitude as, and adjacent to, the upper negative charge in the anvil of the northern storm. (Ingesting colder, drier air from the outflow of the southern storm into the updraft of the northern storm reduced the height of the northern storm.) The probable cause of lightning initiation in the region of anvil convergence (Fig. 4.1) is that the electric field magnitude was increased by the two converging anvils bringing opposite polarities of charge close together at the same altitude. The period from 2330 to 0010 UTC was a transitional period in which neither storm produced any lightning $>$ 30 km from its convective core. Throughout this period, lightning activity was influenced by the growth of the southern storm and the weakening of the northern storm. For example, the amount of lightning involving upper negative charge in the northern storm decreased dramatically from Fig. 4.2a to 4.2c, and the eastward extent of lightning into the anvil decreased steadily in Fig. 4.2a,c,e. By 2350-0000 UTC (Fig. 4.2g), the amount of lightning in both the core and anvil of the northern storm had decreased considerably. Though lightning in the northern storm appeared to increase slightly from 2350 to 0010 UTC (Figs. 4.2g-j, 4.3d-e), much of this lightning originated in the southern storm and propagated into the northern storm, and none was initiated in the northern anvil. By 0040 UTC, no lightning was detected in the northern anvil at all.

Although the southern storm grew in size and the total amount of lightning it produced (not shown) increased 2330-2350 UTC, the eastward extent of lightning into the anvil of the southern storm shrank to a minimum by 2350 UTC (Fig. 4.2b,d,f), possibly due to the decreasing contribution of charge from the northern anvil. After 2350 UTC, lightning began again to extend farther into the anvil of the southern storm (Fig. 4.2f,h,j), but this time in both the upper negative and midlevel positive

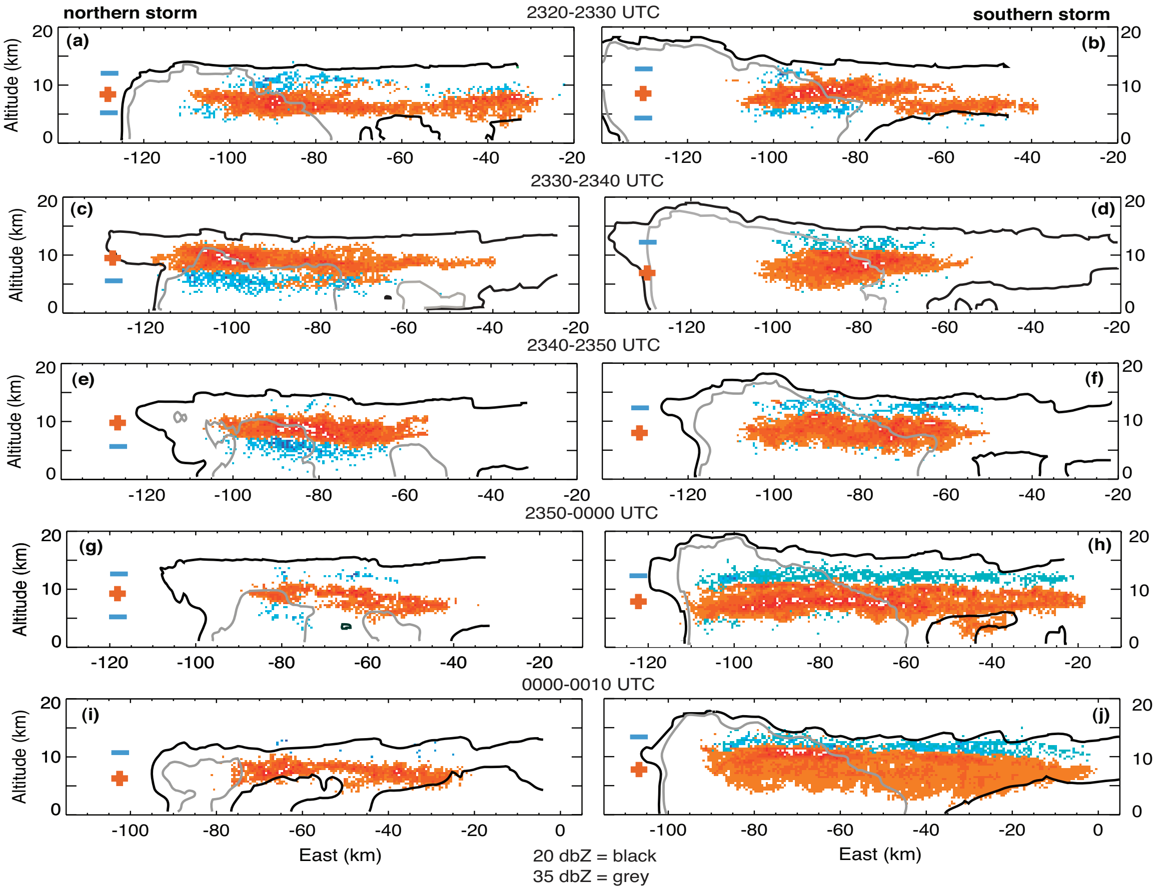

Figure 4.2: (a-j) East-altitude projection of charge distributions inferred from mapped lightning in 10-minute periods 2320-0010 UTC. Orange points are mapped VHF sources inferred to have been in positive charge; blue points, in negative charge. Northern storm is shown in left column; southern storm, in right. The assignment of sources to a particular storm was by eye using the convergence line between anvils as the boundary; all sources that occurred in the two anvils are shown in one storm or the other. Black and grey lines are contours of 20 and 35 dBZ reflectivity, respectively, in a vertical cross section along a line through the corresponding storm core and the center of the anvil. The VHF points in the core are mainly for the part of the storm core near the anvil. Those closer to the updraft core are omitted.

regions. Lightning initiations (not shown) also began to occur in the southern anvil increasingly far from the core, but not beyond 30 km, through 0010 UTC.

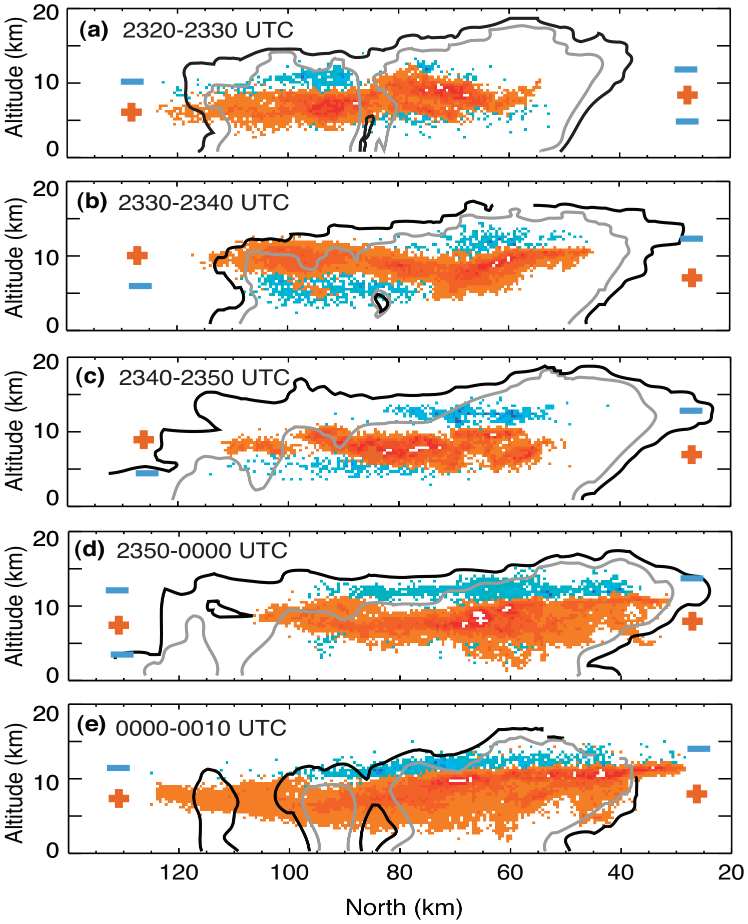

Figure 4.3: (a-e)Same as Fig. 4.2, except north-altitude projection. Reflectivity contours are along a north-vertical cross section through the storm cores.

After the transition period, the first flash to be initiated in the southern anvil > 30 km from the southern core was an intracloud flash that occurred at 0013:48.9 UTC. Subsequently, the majority of flashes initiated in the distant anvil through 0040 UTC were -CG flashes (the rest were intracloud flashes). The rate at which flashes had been initiated in the distant anvil of the northern storm 2255-2325 UTC was typically less than 1 per minute, but the rate in the southern anvil after 0013 UTC quickly increased to larger values (Fig. 4.4). From 0020 to 0040 UTC, distant -CG flashes were initiated in the southern anvil at rates of 3-5 per minute, and many initiations were $>$ 75 km from the southern storm core.

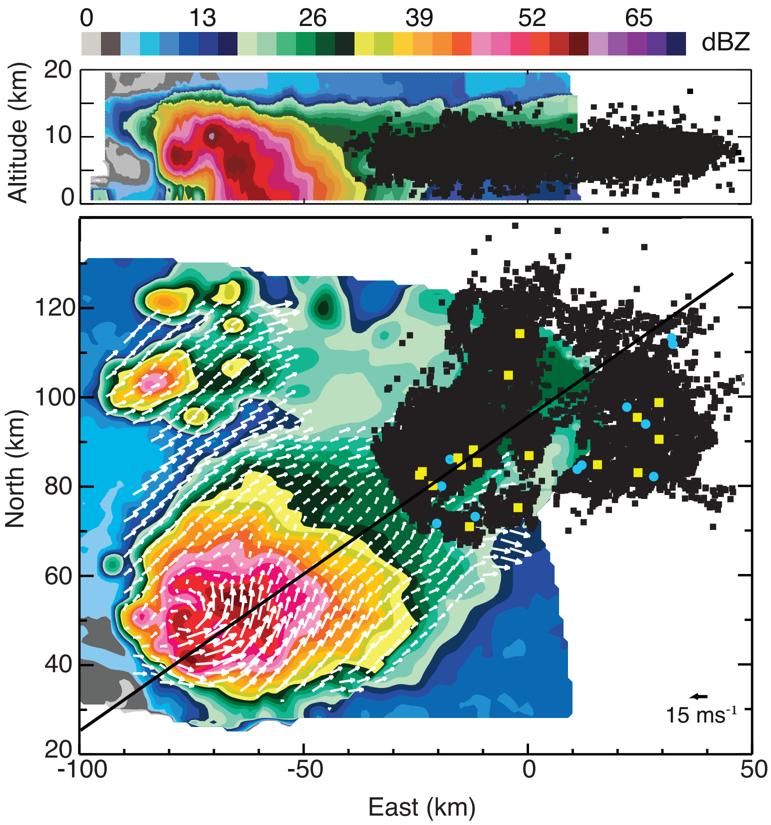

Figure 4.4: Mapped VHF sources for the 2-minute period beginning 0030:30 UTC, overlaid on radar reflectivity and synthesized horizontal winds from the volume scan beginning at 0038 UTC. (Bottom) Vectors are synthesized horizontal winds at 7.8 km AGL. Lightning initiation locations are indicated by yellow squares; -CG ground strike points, by blue circles. The lack of lightning and the low reflectivity values far downwind in the northern anvil together indicate that the northern storm likely contributed no significant charge to distant anvil lightning. (Top) All mapped LMA points in bottom panel superimposed on vertical cross section of reflectivity along the black line shown in bottom panel.

4.3 Discussion and Conclusions

Two aspects of the above observations are remarkable: (1) some flashes were initiated 30-100 km from the convective core and (2) CG flashes in the distant anvil were -CG flashes, instead of the +CG flashes usually observed there. We discuss -CG flashes first.

All CG flashes observed to have begun in the distant anvil of either storm were -CG flashes, in contrast to a previously published report that only +CG flashes occurred far from the core (Rust et al. 1981). Furthermore, all -CG flashes that struck ground far from the convective core were initiated in the anvil. As in Fig. 4.1, the -CG flashes that began in the anvil typically were initiated between 8 and 10 km MSL, below the upper negative charge and above midlevel positive charge, struck ground almost directly under the initiation point, and tended to propagate back toward the storm cores.

This initiation between an upper negative and lower positive charge is consistent with the usual configuration for -CG flash initiation (Jacobson and Krider 1976; Mansell et al. 2002). (Most CG flashes are thought to occur when the electric potential well created along the lightning path by the lower charge region is too shallow to terminate the downward propagating channel, a condition that can arise in several ways.) However, having substantial negative charge over positive charge (as needed to produce most -CG flashes) in the anvil is a consequence of the convective core having a vertical electrical structure whose polarity was inverted from the usual polarity. Thus, having -CG flashes, instead of the usual +CG flashes, in the distant anvil probably was a consequence of the inverted electrical structure of the parent storm.

Now we consider flash initation in the distant anvil. It is not surprising that an already initiated flash can extend into the anvil, because anvils can contain substantial amounts of electric charge, as indicated by measurements of large electric fields in anvils (Marshall et al. 1989; Byrne et al. 1989; Dye et al. 2007; Dye and Willett 2007).

Most charge in the anvil is commonly thought to originate in the updraft of the storm core and to be carried into the anvil by horizontal flow from the diverging upper level updraft (e.g., Byrne et al. 1989; Dye et al. 2007). This is consistent with our observation that the rate of flash initiation in the anvil and that the distance flashes extended into the anvil both exhibited cycles consistent with the timing of typical updraft lifecycles. Increases were often clearly related to overall storm intensification, when the mass flux into the anvil also would increase, and decreases occurred as the storm weakened.

The dependence on charging in the updraft can explain lightning propagating from the core into the anvil, but fails to explain how lightning can be initiated in the distant anvil. Electric fields and charge would be expected to decrease with distance into the anvil because of diffusion and the electrical conductivity of air (e.g., Dye et al. 2007), if there were no additional influence in the anvil itself. Something must enhance the electric field enough locally in the anvil to initiate lightning there. We suggest two basic ways this can happen: (1) convergence or confluence of charge or (2) a local charging mechanism within the anvil.

Confluence of charge from the two anvils likely explains the initiation of distant anvil lightning near the beginning of the analyzed period (Figure 4.1). However, converging anvils cannot explain initiation in the anvil at earlier or later times, because initiation occurred in the distant northern anvil before it was influenced significantly by the southern storm and occurred in the distant southern anvil long after the northern storm stopped producing lightning and had completely dissipated. It may also be possible for other forms of charge convergence to enhance the electric field, such as: (1) convergence between the anvil and the upper outflow of weak storms developing beneath the anvil, (2) vertical motions in the anvil driven by speed variations in the outflow from surges in the main updraft, or (3) vertical convergence from gravity waves in the anvil, caused by buoyancy forces from the overshooting updraft.

It is also possible that some charging mechanism is active inside the anvil. A recent study of electric field and radar reflectivity measurements in two Florida storm anvils concluded that there is some such mechanism in anvils (Dye and Willett 2007). The basic modeling and analyses to support the idea of a significant charging mechanism in the anvil are essentially the same as those that have been used to conclude that a significant charging mechanism exists in the stratiform precipitation regions of mesoscale convective systems (MCSs). MCS stratiform regions are highly electrified and contain lightning that is as horizontally extensive (Lang et al. 2004; Dotzek et al. 2005; MacGorman et al. 2008b) as the anvil lightning we observed. Observational and modeling studies have concluded that, while much of the charge in stratiform regions is advected from the convective line, charge is also generated locally in the stratiform region (e.g., Stolzenburg et al. 1994; Schuur and Rutledge 2000).

One reason for thinking that a local charging mechanism is active in stratiform regions and in the anvils we observed is that lightning can occur farther from deep convection and more frequently in both situations than would be expected from charge transport alone. At times during the period we analyzed, the rate at which flashes were initiated in the anvil exceeded 5 min^{-1}, and many of these flashes tended to be initiated in and propagate through roughly the same region for 5-10 minutes at a time. Thus, either each flash removed relatively little charge from those regions of the anvil, or the charge was replenished within roughly 10-30 s, too little time for charge transport across the region of anvil lightning activity.

Chapter 5

Ensemble Kalman Filter and Numerical Simulations

5.1 Introduction

Numerical simulations are valuable tools for three-dimensional storm-scale analysis. The process of obtaining 3D velocity and thermodynamic field from radar data, namely through dual-Doppler synthesis and analysis as done in Chapter 3, is subject to errors (particularly when deriving properties from the vertical velocity estimates) and falls short of providing a complete enough description of the storm and environment to determine what processes are responsible for producing various storm phenomena. Ziegler (1985) and others have suggested employing numerical models to retrieve thermodynamic and microphysical variables of convective storms. This idea has been advanced more recently through the introduction of radar data assimilation as a means to reduce the differences between observed and model storms (Sun and Crook 1998; Snyder and Zhang 2003; Dowell et al. 2004), often to improve the initial state of the atmosphere used for forecasts. For the present study, the ensemble Kalman filter (EnKF) method for data assimilation, described by Dowell et al. (2004), was employed, not to improve forecasts, but to retrieve the storm state during the period in which radar data were obtained.

The availability of nearly continuous radar data from SR2 on 29 May during a particularly intense period of the supercell storm as it moved through the TELEX domain provides high resolution (in both time and space) reflectivity and velocity data for assimilation. The details of the model and data assimilation system are discussed below in Section 5.2. Section 5.3 compares the simulated storm to observations of the storm and discusses the new results.

5.2 Model Details

5.2.1 Dynamics and Microphysics

The COMMAS model uses the basic kinematic equation set from Klemp and Wilhelmson (1978) with prognostic equations for momentum, pressure, potential temperature, and turbulent kinetic energy (Coniglio et al. 2006). The numerical integration scheme follows the methodology of Wicker and Skamarock (2002) and Bryan (2005): a third-order Runge-Kutta scheme is used with 5th-order differencing on the first two iterations followed by 6th-order finite differencing for scalar quantities on the final step. Wind components are advected by using a 5th-order non-oscillatory scheme (Bryan 2005).

The microphysics package currently employed in the COMMAS model is described in detail in the Appendix of Mansell et al. (2010); however, it will also be briefly summarized below. The microphysics scheme used is adapted from Ziegler (1985) with modifications from Straka and Mansell (2005) for additional diversity in graupel and hail fall speed. A two-moment scheme predicts both mixing ratio and number concentration for the six hydrometeor categories (shown in Table 5.1, along with the assumed density or range of densities for water in each category). In addition, the scheme also predicts the bulk concentration of cloud condensation nuclei (CCN) and the average bulk densities of graupel and hail. Graupel density varies and can range

Category	Abbreviation	Density (kgm^{-3})
Cloud Droplets	q_c	1000
Rain	q_r	1000
Cloud Ice	q_i	900
Snow	q_s	100
Graupel	q_g	300-900
Hail	q_h	500-900

Table 5.1: Hydrometeor categories and densities. A range signifies imposed limits on hydrometeor densities in the two solid categories for which density is predicted. From Mansell et al. (2010).

from low-density graupel to high density frozen drops (or small hail, as in Mansell et al. (2010)). The conversion of graupel to hail occurs under wet growth conditions, as done by Milbrandt and Yau (2005), but with the additional constraint that the density of the rime accreted by the graupel is sufficiently high ($> 800\,kg\,m^{-3}$) and the temperature is $< -2°C$, as done by Mansell et al. (2010).

5.2.2 Charging, Electrification, and Lightning

The model includes a choice of parameterizations for charging hydrometeors. This study uses both inductive and noninductive charging to produce electrification. The results of laboratory and modeling studies strongly suggest that noninductive charging plays the primary role in producing electrification levels close to that of observed storms (MacGorman and Rust 1998). However, it is believed that inductive charging could also play a role (Mason 1988; Brooks and Saunders 1994). Inductive charging occurs in the presence of an electric field, when a rebounding collision occurs between two polarized particles. In the model, inductive charging is included only during graupel-droplet collisions and then specifically in "dry-growth" mode. Noninductive charging (independent of the electric field) occurs during rebounding collisions between riming graupel and ice particles in the presence of liquid water. Differential sedimentation of the graupel and small cloud particles separates the opposite polarities of charge into regions of net charge. As the amount of net charge in various regions increase, the electric field also tends to increase. With enough charging, the electric field eventually increases to the point that it produces lightning.

Inductive charging in the model is calculated based on a formula from Ziegler et al. (1991). This equation is expressed by Mansell (2000) in terms of characteristic diameter $\mathcal{D}_g$ and mass weighted mean fallspeed $\bar{V}_g$ of graupel as:

$$\begin{aligned} \frac{\partial \varrho_g}{\partial t} &= (\pi^3/8)\left(\frac{6.0\bar{V}_g}{\Gamma(4.5)}\right) E_{gc} E_r n_{t,c} n_{0g} D_c^2 \times \\ &\quad \left[\pi \Gamma(3.5) \epsilon \langle \cos\theta \rangle E_z \mathcal{D}_{n,g}^2 - \Gamma(1.5) \varrho_g / (3 n_{t,g})\right]. \end{aligned} \tag{5.1}$$

In Eq. 5.1, E_{gc} and E_r are the collection and rebound efficiencies, $n_{t,c}$ and $n_{t,g}$ are the total cloud water and graupel number densities, $n_{0,g}$ is the number concentration intercept for graupel, D_c is the cloud droplet diameter, $\langle \cos\theta \rangle$ is the average cosine of the angle of the rebounding collision, E_z is the vertical component of the electric field, ϱ_g is the charge on graupel, and ϵ is the permittivity of air. The inductive charging used in the simulations approaches values described as "strong" by Mansell et al. (2003), with $E_r = 0.01$ and $\langle \cos\theta \rangle = 0.45$.

Noninductive charging involving riming graupel and ice crystals has been the focus of several laboratory experiments (e.g., Takahashi 1978; Brooks and Saunders 1995; Saunders and Peck 1998; Pereyra et al. 2000; Saunders et al. 2006). The charge gained by the graupel is dependent on the ambient temperature and the liquid water content as well as the size and growth state of the hydrometeors. Different studies have focused on a reversal temperature for the transition in the polarity of charge gained by the graupel. Most studies agree that the reversal temperature is dependent on the liquid water content or riming rate, though differences arise in determining the conditions for charge polarity reversal. The general formula for noninductive charge separation between colliding particles x and y is:

$$\frac{\partial \varrho_{xy}}{\partial t} = \int_0^\infty \int_0^\infty \frac{\pi}{4} \delta q'_{xy} (1 - E_{xy}) |V_y - V_x| (D_x + D_y)^2 n_x(D_x) n_y(D_y) dD_x dD_y, \quad (5.2)$$

where D_x and D_y are the diameters of the colliding particles, E_{xy} is the collection efficiency, $|V_y - V_x|$ is the relative fall speed, n_j is the number concentration of the jth hydrometeor category, and $\delta q'_{xy}$ is the charge separated per collision. Eq. 5.2 can be manipulated into a form such that $\delta q'_{xy} \rightarrow \delta q_{xy}$, or in terms of a representative (weighted average) separated charge per collision as shown in Mansell (2000). The value of $|\delta q_{xy}|$ is limited to a maximum of 50 fC for graupel-snow collisions and 20 fC for graupel-cloud ice collisions to prevent unrealistic charging and lightning rates. Based on previous sensitivity tests of multiple noninductive charging parameterizations (Mansell et al. 2005; Kuhlman et al. 2006b), it was found that the schemes incorporating rime accretion rate better reproduced observational findings. As used by Mansell et al. (2010), this study uses a hybrid parameterization of the noninductive charging mechanism based on the Saunders and Peck (1998) laboratory results, with an adjustment for warmer temperatures ($T > -15^\circ$ C) following Brooks et al. (1997) (Fig. 5.1). The Saunders and Peck (1998) parameterization is described in more detail in the subsection below.

5.2.2.1 Saunders and Peck 1998 (SP98)

The noninductive charging rate in the Saunders and Peck (1998) scheme (SP98) is based on their laboratory charging measurements as a function of temperature and rime accretion rate (RAR). The critical RAR value (RAR_{crit}) is dependent on temperature and delineates positive and negative charging regions in temperature and RAR space (Fig. 5.1). The sign of the charge transferred to the graupel during a rebounding collision in the SP98 scheme is strongly influenced by the amount of

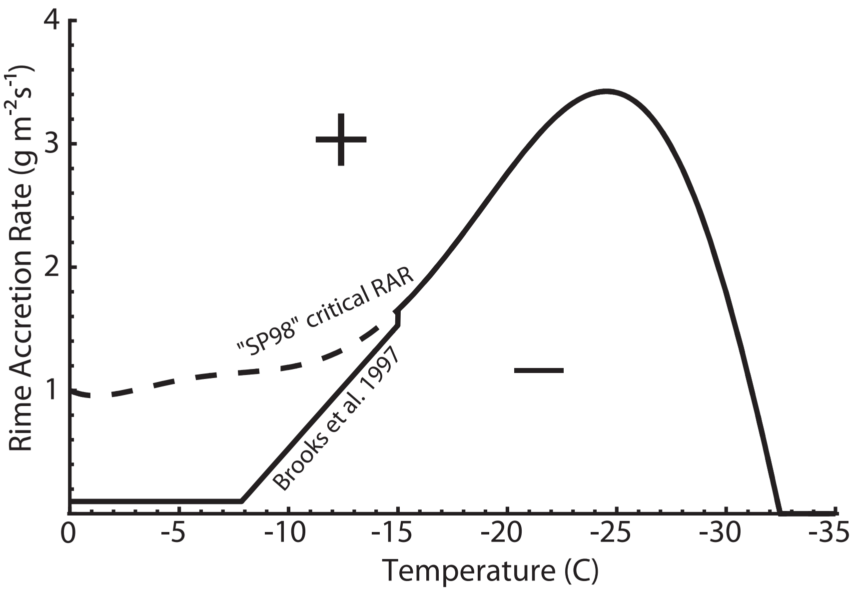

Figure 5.1: Noninductive charge separation sign-reversal curve. The critical rime accretion rate (RAR) curve follows Saunders and Peck (1998) for $T < -15°$ C (shown as dashed curve for $T > -15°$ C) and Brooks et al. (1997) at warmer temperatures. Charge transfer is set to zero for $T < -33°$ C. Adapted from Mansell et al. (2010).

water accreted on the graupel (i.e. the rimer). The charge separated per collision (δq) is calculated according to Brooks et al. (1997) as:

$$\delta q = BD^a_{n,\mathrm{I}}(\bar{V}_g - \bar{V}_\mathrm{I})^b q_\pm(RAR), \tag{5.3}$$

where B, a, and b are constants that depend on crystal size (Table 5.2), $D_{n,\mathrm{I}}$ is the diameter of the cloud ice or snow, and $\bar{V}_g$ and $\bar{V}_\mathrm{I}$ are the mass weighted mean terminal speeds for graupel and ice crystals. If $RAR > RAR_\mathrm{crit}$ the graupel charges positively according to

$$q_+(RAR) = 6.74(RAR - RAR_\mathrm{crit}). \tag{5.4}$$

If $RAR_\mathrm{crit} > RAR > 0.1\,\mathrm{g\,m^{-2}s^{-1}}$ the graupel charges negatively as

$$q_-(RAR) = 3.9(RAR_\mathrm{crit} - 0.1)\left(-1.0 + 4.0\left[\frac{RAR - (RAR_\mathrm{crit} + 0.1)/2.0}{(RAR_\mathrm{crit} - 0.1)}\right]^2\right). \tag{5.5}$$

Charging is set to zero for $RAR < 0.1\,\mathrm{g\,m^{-2}s^{-1}}$.

Charge sign	Crystal size (μm)	B	a	b
+	< 155	4.9×10^{13}	3.76	2.5
+	155–452	4×10^{6}	1.9	2.5
+	> 452	52.8	0.44	2.5
−	< 253	5.24×10^{8}	2.54	2.8
−	> 253	24	0.5	2.8

Table 5.2: Values of constants for riming rate charging scheme (from Brooks et al. 1997).

In the model, the curve RAR$_{crit}$ in the SP98 scheme (Fig. 5.1) is calculated as a piecewise function as given by Mansell (2000):

$$RAR_{\mathrm{crit}}(T) = \begin{cases} s(T) & \text{for } T > -23.7°\mathrm{C} \\ k(T) & \text{for } -23.7 > T > -40.0°\mathrm{C} \\ 0 & \text{for } T \leq -33.0°\mathrm{C}, \end{cases} \tag{5.6}$$

where $s(T)$ is the sixth-order polynomial function given by Saunders and Peck (1998):

$$\begin{aligned} s(T) &= 1.0 + 7.9262 \times 10^{-2}T + 4.4847 \times 10^{-2}T^2 \\ &\quad +7.4754 \times 10^{-3}T^3 + 5.4686 \times 10^{-4}T^4 \\ &\quad +1.6737 \times 10^{-5}T^5 + 1.7613 \times 10^{-7}T^6. \end{aligned} \tag{5.7}$$

Since the function $s(T)$ becomes negative at temperatures less than $-32.45°$ C and liquid droplets can exist at temperatures colder than this, the function $k(T)$ is used for $T < -23°$ C to keep the critical RAR positive down to $T < -33°$ C:

$$k(T) = 3.39608 \left[1.0 - \left(\frac{|T + 23.7|}{-23.7 + 40.0}\right)^3\right]. \tag{5.8}$$

In Eq. 5.8, k(T) experiences a cubic decrease from $k(-23.7) = s(-23.7)$ to $k(-33) = 0$.

5.2.2.2 Charge Conservation, Advection, and Ions

A charge density is connected with every hydrometeor type. As mass shifts between categories in the microphysics, the charge also is transferred from one category to another (e.g., mass from ice to rain). Although charge is conserved in the model domain, charge is not absolutely conserved due to charge movement from ion currents entering or exiting the domain, advection through a lateral boundary, or transport to ground by lightning. The charge continuity equation from Mansell (2000) resembles a typical conservation equation with treatment of advection, diffusion, and falling particle motion. The model neglects the accelerations of charged particles in an electric field. The electric field is determined as the negative gradient of the potential: $\mathbf{E} = -\nabla\phi$.

Small ion processes are also included in the model (Mansell et al. 2003). Conservation equations are defined for both positive and negative ion concentrations. The equations take into account advection and mixing, drift motion (ion motion induced by the electric field), cosmic ray generation, ion recombination, ion attachment to hydrometeors, corona discharge from the ground, and release of ions from evaporating hydrometeors. Mansell et al. (2003) use a fair weather state from Gish (1944) as expressed by Helsdon and Farley (1987) to incorporate sources of ions unrelated to thunderstorms.

5.2.2.3 Lightning Parameterization

Lightning flashes are parameterized by a stochastic dielectric breakdown model as described in Mansell et al. (2002, 2005), a version of which has been employed, for example, by Kuhlman et al. (2006b), Riousset et al. (2007), Krehbiel et al. (2008), and Mansell et al. (2010). The lightning develops bidirectionally across a uniform grid with each step chosen randomly from among the surrounding points at which the electric field meets or exceeds a threshold value for propagation. After each step, the electric field is recalculated to include the contribution of the lightning channel to the electric field. The end result is a branched, fractal-like leader structure of each flash in three dimensions.

Following Mansell et al. (2010), flash initiation occurs if the electric field reaches the threshold for runaway air breakdown determined by Dwyer (2003). A particular initiation point is chosen randomly from all the points that exceed $0.9E_{\mathrm{be}}$ and each channel maintains an overall charge neutrality. The critical threshold for continued channel propagation is assumed to be a fraction of the initiation threshold. Continuation of lightning propagation is quite sensitive to the grid resolution (Tan et al. 2006). Even though the lightning grid spacing is smaller in the horizontal (500 m) than the dynamics grid spacing(1 km), it still does not approach the 250 or 12.5 meter resolutions that were tested by Tan et al. (2006). Thus, the threshold for continued breakdown of lightning leaders relative to initiation is set to be quite small in this study to compensate for the inadequate resolution (Mansell et al. 2010).

Positive leaders carry positive charge and tend to travel preferentially through negative charge regions, while negative leaders carry negative charge and tend to travel through regions of net positive charge (Mansell et al. 2002). Therefore, the simulated flashes tend to reflect the charge structure of a storm simulation. As in Mansell et al. (2005, 2010), a flash is declared to be a CG if it descends to a height threshold of 500m (or 3 grid points above ground); however, even with this addition, the model under-predicts the fraction of flashes that strike ground relative to observations.

5.2.3 Data assimilation through EnKF

Following the methodology of Dowell et al. (2004), a full objective analysis to a Cartesian grid of the radar data was not completed. Instead, each sweep of edited SR2 data was objectively analyzed separately to a x-y grid, maintaining the conical distribution of the data and reducing vertical interpolation errors. A Cressman weighting function with a 1000 m radius of influence was used with grid points spaced 2000 m apart in the horizontal, corresponding to model grid points. The vertical height of the data corresponds to the actual height of the observation on the conical scan at the (x, y) location. Reflectivity and radial velocity data from SR2 were assimilated in approximately five minute intervals from 2320 UTC to 0040 UTC up to 8.5 km in height (limited to prevent overprediction of precipitation due to large reflectivities aloft and continuous coverage from SR2). The EnKF methodology (specifically, an ensemble square root filter–EnSRF) was used to assimilate the observations following the process described by Dowell and Wicker (2009). The EnSRF uses the traditional Kalman gain for updating the ensemble mean but uses a "reduced" Kalman gain to update deviations from the ensemble mean (Whitaker and Hamill 2002)

As completed by Dowell et al. (2004), observations are processed one at a time, under the assumption that observational errors are uncorrelated in space and time. In short, the entire assimilation process was completed by converting each model state to an expected observation, comparing the value with the observation and observational error distribution, determining the incremental difference, creating the state variable increments and new state variables, and finally advancing the model and repeating the steps at the next observational time. During this process, the ensemble mean and members are updated according to the following equations:

$$K = \frac{\frac{1}{N-1}\sum_{n=1}^{N}\left(x_n^f - \bar{x}^f\right)\left[H\left(\mathbf{x}_n^f\right) - \overline{H\left(\mathbf{x}^f\right)}\right]}{\sigma^2 + \frac{1}{N-1}\sum_{n=1}^{N}\left[H(\mathbf{x}_n^f) - \overline{H\left(\mathbf{x}^f\right)}\right]^2}, \tag{5.9}$$

$$\beta = \left[1 + \sqrt{\frac{\sigma^2}{\sigma^2 + \frac{1}{N-1} \sum_{n=1}^{N} \left[H(\mathbf{x}_n^f) - \overline{H\left(\mathbf{x}^f\right)} \right]^2}} \right]^{-1}, \tag{5.10}$$

$$\bar{x}^a = \bar{x}^f + WK \left[y^o - \overline{H\left(\mathbf{x}^f\right)} \right], \tag{5.11}$$

$$x_n^a = \bar{x}^a + \left(x_n^f - \bar{x}^f \right) + WK\beta \left[\overline{H\left(\mathbf{x}^f\right)} - H(\mathbf{x}_n^f) \right], \tag{5.12}$$

where K is the Kalman gain, N the number of ensemble members (25, including the mean), n is the index of a particular member, x is the model field, $\mathbf{x}$ the entire model state, the superscript f indicates a forecast state prior to assimilation, the superscript a indicates an analysis state after the assimilation, an overbar indicates the esemble mean. H represents the observation operator and maps the model state to the observation type and location. σ^2 is the observation-error variance for Doppler velocity $(2.0\, ms^{-1})^2$ and reflectivity (5 dBZ) (Dowell et al. 2004), y^o is the observation, and β is the reduced-gain factor (Whitaker and Hamill 2002; Dowell and Wicker 2009).

5.2.4 Model Configuration

This analysis created an ensemble of model states (24 members plus an ensemble mean) starting at 2305 UTC, advanced the ensemble to the first observation time (2320 UTC), assimilated all observations within 60 sec of the time, advanced the ensemble to next observation time, and repeated the process until the last observation was assimilated at 0041 UTC.

The model domain is 140 km x 140 km x 22 km with horizontal grid spacing of 1 km and vertical grid spacing of 200 m stretched to a maximum of 500 m at 20 km over 53 grid points. Lightning propagation is calculated on a higher resolution grid with 500 m spacing in the horizontal with lateral domain extensions of 10 km at 500 m spacing

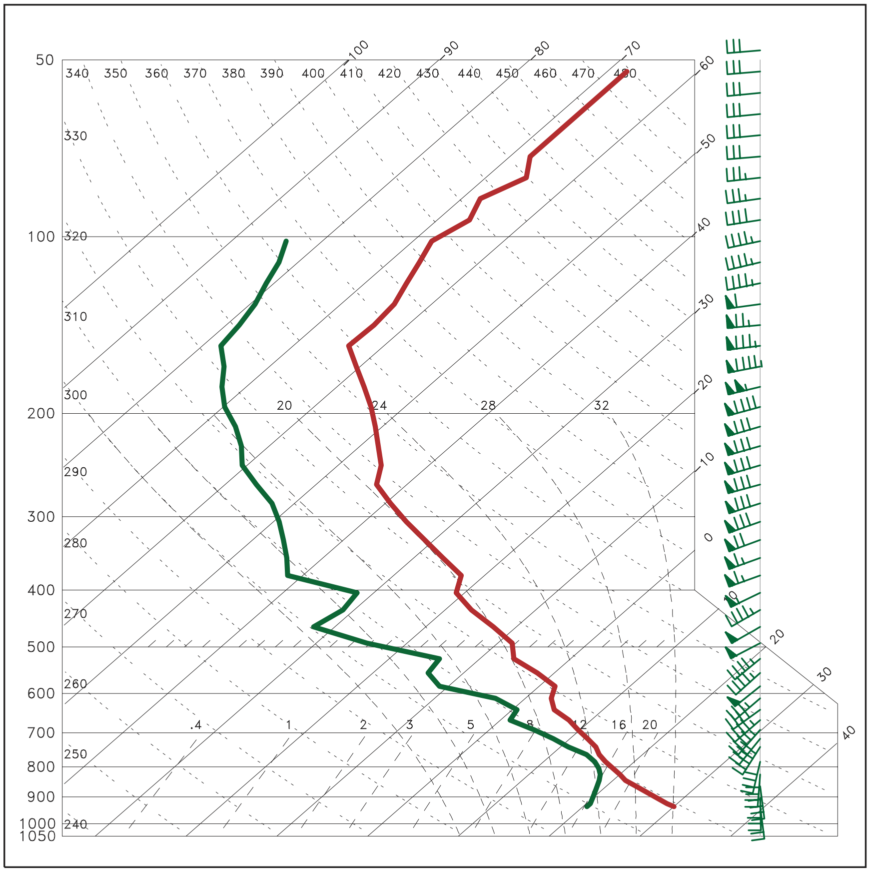

Figure 5.2: Skew T – log p diagram for the base state in the assimilation experiments interpolated to model grid levels. Below 400 mb, the sounding is taken from an environmental sounding released near Weatherford, OK. Above 400 mb, the sounding is from data from the National Weather Service Norman, OK sounding released at 0000 UTC. Winds are plotted with a filled flag $= 25 m\, s^{-1}$, full barb $= 5 m\, s^{-1}$, and half-barb $= 2.5 m\, s^{-1}$.

surrounding the dynamics domain. The environment over the domain is initialized to be horizontally homogeneous using a combination of two soundings merged into one. Below 400 mb, the sounding is taken from an environmental sounding released near Weatherford, OK. Above 400 mb, the data is from the sounding released at the Norman, Oklahoma National Weather Service Forecast Office at 0000 UTC.

The simulations employed a two-moment microphysics scheme with variable graupel and hail density (predicts hydrometeor number concentration and mass). A 24-member ensemble was used; convective storms developed in the ensemble members through the random bubbles, model advance, and data assimilation. Randomly-perturbed (4 K) warm bubbles were inserted in the boundary layer in each member where cells are indicated by radar reflectivity within 21 min in the future. Reflectivity and velocity from SR2 are assimilated in approximately five minute intervals from 2320 UTC to 0040 UTC up to 8.5 km. Prior to the assimilation radar data has been objectively analyzed to a 2km grid in x and y by using a Cressman weighting function, as described by Dowell et al. (2004).

5.3 Results

5.3.1 Comparison with dual-Doppler observations

Typically, all members of the ensemble contain weaker reflectivity values than those noted with the dual-Doppler analyses in Chapter 3. This is especially true at mid-levels of the storm, where the reflectivity is particularly deficient in the region of the southern overhang and within the back shear anvil. The weaker reflectivity values are due in part to the state of the assimilated data; SR2 was located southwest of the storm core throughout the assimilation period and suffered from attenuation. Therefore, in both the SR2 data and all of the ensemble members, the reflectivities directly along the path of the radar beam behind the storm hail core are too weak.

On average, the mesocyclone strength in the simulations was considerably weaker than the dual-Doppler derived mesocyclones seen in Chapter 3, though the location and shape are generally well matched. The vertical velocity values of the main updraft in the simulations were slightly smaller at low-levels, but nearly identical at mid and upper levels of the storm (Fig. 5.3) (the earliest comparison time, 2347 UTC, is not as well matched as the storm in the simulations is still developing at this time). The differing values of the mesocyclone strength, in particular the lower values in the simulations, are somewhat expected with the 1 km grid spacing, as smaller grid

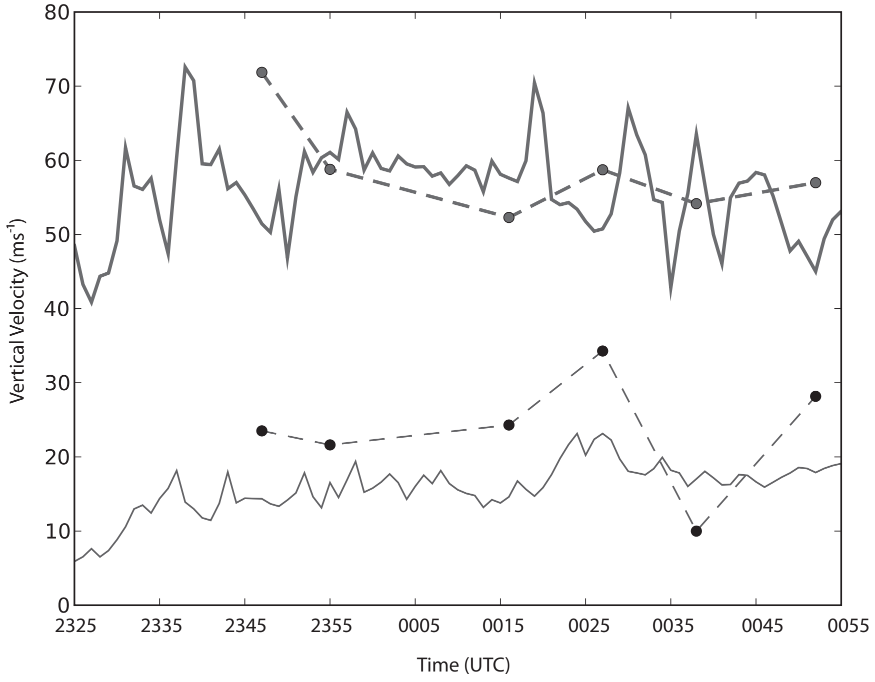

Figure 5.3: Maximum vertical velocity ($m\,s^{-1}$) in Member 1 the EnKF (solid lines) simulations and dual-Doppler analyses (points) at 1.5 km (lower values) and 9 km AGL.

spacing (such as the 500 m used in the dual-Doppler analyses) may enable slightly higher values (Adlerman and Droegemeier 2002). Throughout the remainder of this chapter (including all figures), specific comparisons with dual-Doppler analyses are made with Member 1 of the ensemble (all members provide similar kinematic results, but Member 1 includes electrification processes).

Member 1 at 0018 UTC (Fig. 5.4) matches well with the dual-Doppler analysis beginning at 0016 UTC (Fig. 3.7). While reflectivity values in the simulation tend to be about 5 dBZ less and not as large in areal extent as observed, the overall shape of the storm and hook echo as well the location of the maximum of the FFD are handled quite well by the simulation. The mesocyclone size, shape and strength are all replicated by the simulation. The maxima of the updraft at low-levels along the edge of the outflow and the hook echo as well as the location of the updraft associated with the BWER at mid-levels are captured by the simulation. In addition, the simulation produces a secondary updraft along an outflow region (at x=33 km, y=60 km) not seen in the dual-Doppler analysis, possibly due to the west side of the storm not being captured well by SR1 (located east-south-east of the storm) at this time.

At 0028 UTC (Fig. 5.5), the simulation reproduces the two observed regions of the RFD at 1 km (compare with Fig. 3.8): one with the peak reflectivity near the end of the hook and another extending along the arm of the hook from the core. The simulated FFD is colocated with the max in reflectivity in the storm core and slightly stronger in the simulation than in the dual-Doppler analysis. The size and shape of the main updraft at low levels is well approximated with similar peak values and similar locations: above the tip of the hook and following the outflow boundary along the reflectivity edge around to the south side. However, the simulated storm is smaller than observed at mid-levels, and the simulated mesocyclone is neither as strong nor as circular as observed.

By 0040 UTC (Fig. 5.6), the simulated storm has a much better size and shape (compare with Fig. 3.9), with increased reflectivity values extending through the hook echo and reflectivity values at mid-levels closer to what was observed by radar than during earlier time periods. The simulation captures the occlusion of the mesocyclone and also produces additional wrapping of the main updraft and intrusion of the RFD into the region that may have been missed in the dual-Doppler analysis due to the storm possibly exending beyond the southern edge of the SR1 scans at the time.

By 0050 UTC, the older of the two mesocyclones is totally occluded in the simulations (Fig. 5.7) as was also seen in the observations (Fig. 3.10). As evident in both the observations and the ensemble members, the mesocyclone at this time is not at all associated with the main updraft, but instead is fully wrapped-up within the RFD. As the simulated mesocyclone becomes fully wrapped by the downdraft, it becomes much weaker and decays more quickly than the observed. Meanwhile, a new

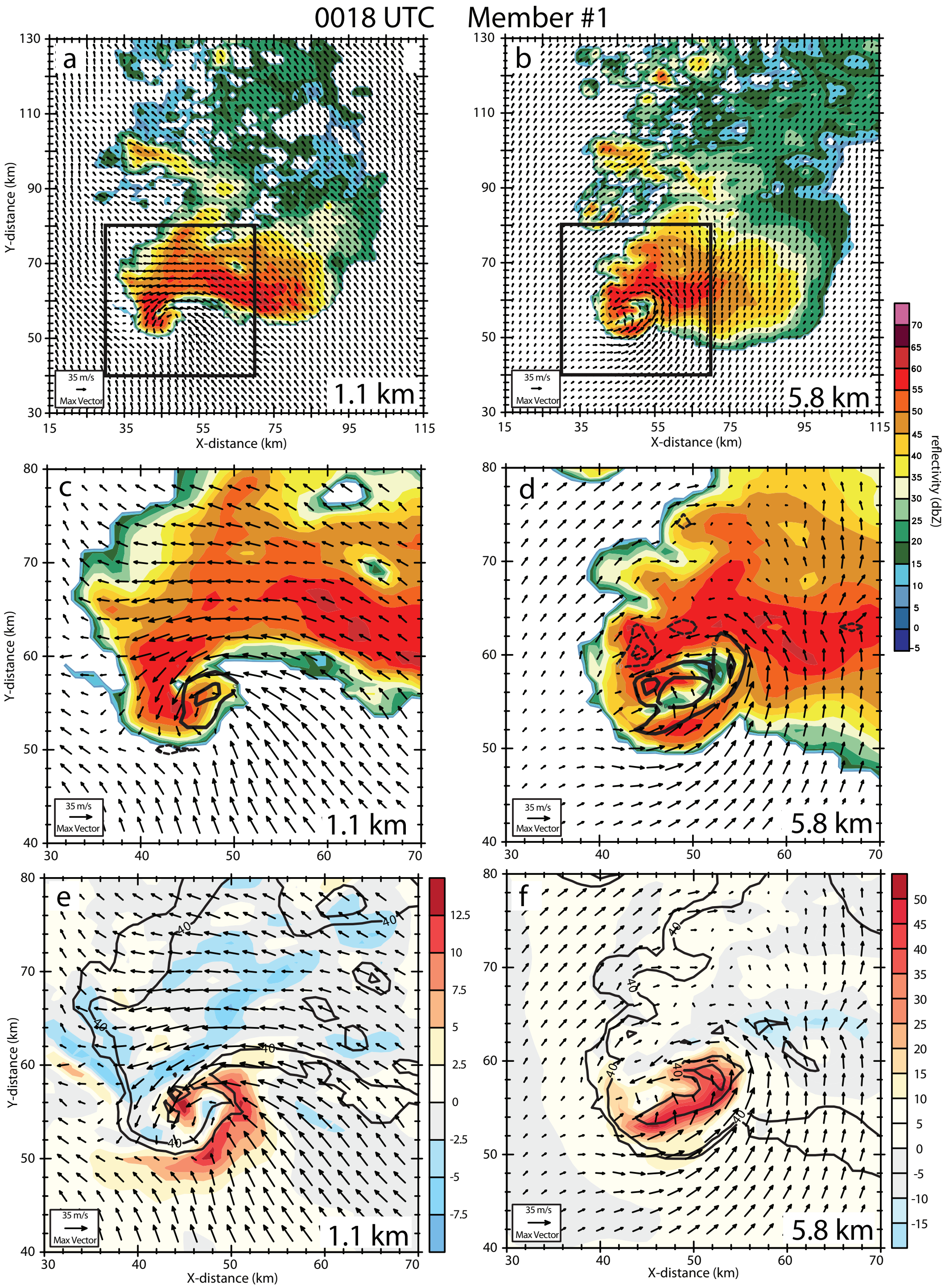

Figure 5.4: (a-b) Reflectivity and wind vectors at 1.1 and 5.8 km AGL at 0018 UTC (72 min). (c-d) Area within box shown in (a-b), reflectivity, wind vectors and contours of vertical velocity every $10 \times 10^{-3}s^{-1}$, beginning at $10 \times 10^{-3}s^{-1}$. (e-f) Color fill indicating vertical velocity. Contours of reflectivity every 20 dBZ.

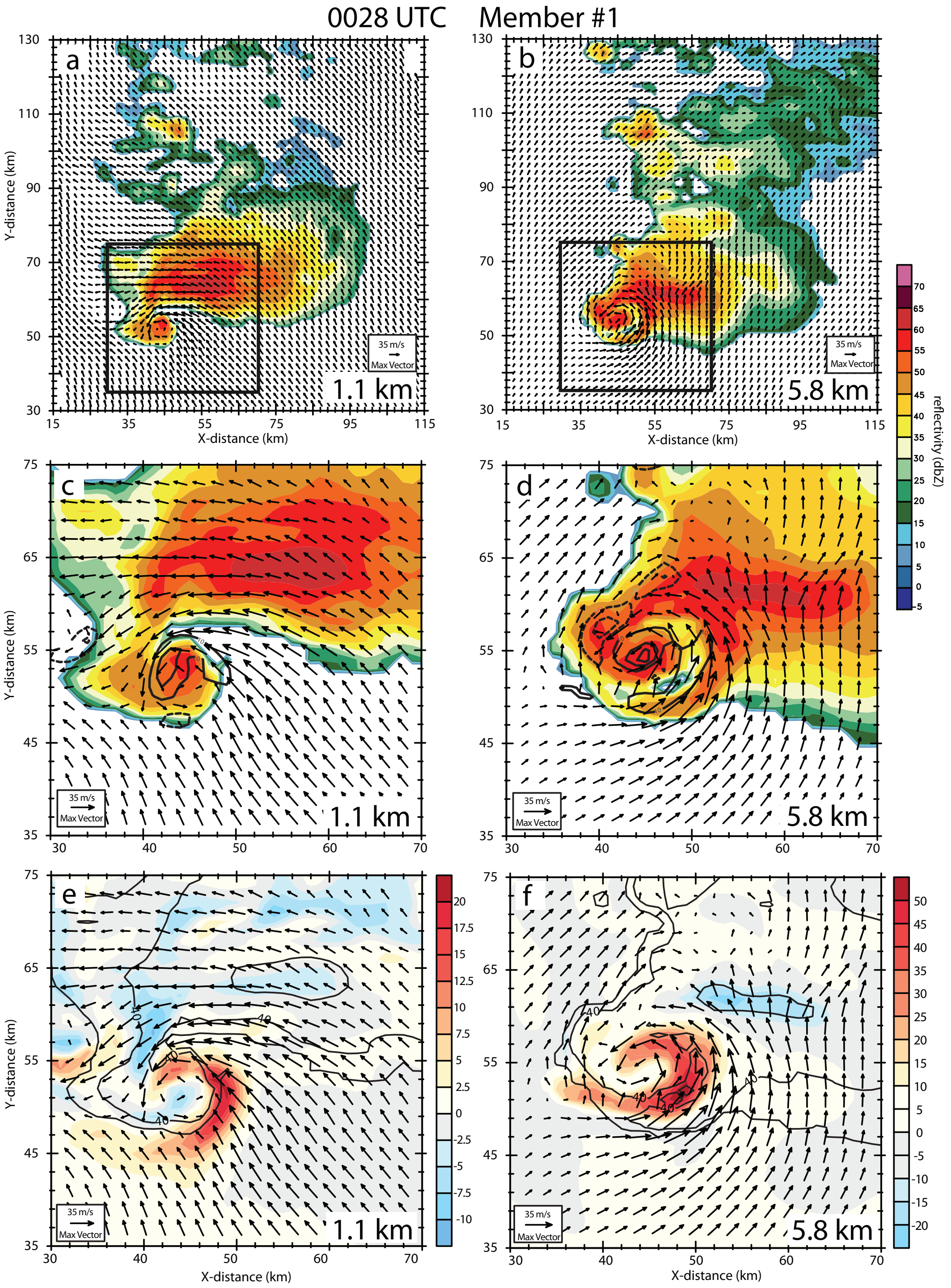

Figure 5.5: (a-b) Reflectivity and wind vectors at 1.1 and 5.8 km AGL at 0028 UTC (82 min). (c-d) Area within box shown in (a-b), reflectivity, wind vectors and contours of vertical velocity every $10 \times 10^{-3} s^{-1}$, beginning at $10 \times 10^{-3} s^{-1}$. (e-f) Color fill indicating vertical velocity. Contours of reflectivity every 20 dBZ.

mesocyclone is developing in the simulation in what is now the main updraft along the gust front farther east.

5.3.2 Microphysical and Electrical Evolution

5.3.2.1 Spatial distribution and evolution

This is a well-developed, mature supercell throughout the analysis period. For the simulations, it was necessary first to initialize storms where they were observed and then to allow them time to take on the character of the observed storms through the data assimilation process. Due to artifacts in the behavior of the lightning, electrification processes were not begun until 40 min into simulation, after characteristics of the subject storm had stabilized somewhat. At that time, the storm was large, with core reflectivities greater than 60 dBZ and updrafts as large as 70 $\mathrm{m\,s^{-1}}$ at mid-levels. Supercell features had developed (including a hook echo and mesocyclone at low levels) as early as 56 min in the simulation.

Charge structure could be discerned in the simulated storm updraft at 42 min, only two minutes after electrification processes were begun. It consisted of an inverted polarity tripole, with a main positive charge region (between 9 and 11 km in height), a small upper negative region (11 to 13 km) and a large lower negative region (5 to 9 km). The width of this charged region covered about 10 km horizontally. Less than two minutes later (at approximately 44-46 minutes into the simulation), the charge structure had evolved dramatically: the core of the storm contained six layers of charge, as a small lower positive region (below 4 km) and an upper dipole (between 13 and 16 km) have developed. The center of the structure was still dominated by the inverted tripole seen in the first two minutes of electrification, but the main main positive charge region had expanded in depth and width while the lower negative charge region moved further downward and outward into the FFD. At this point, the region of the storm containing charge took up about 20 km horizontally.

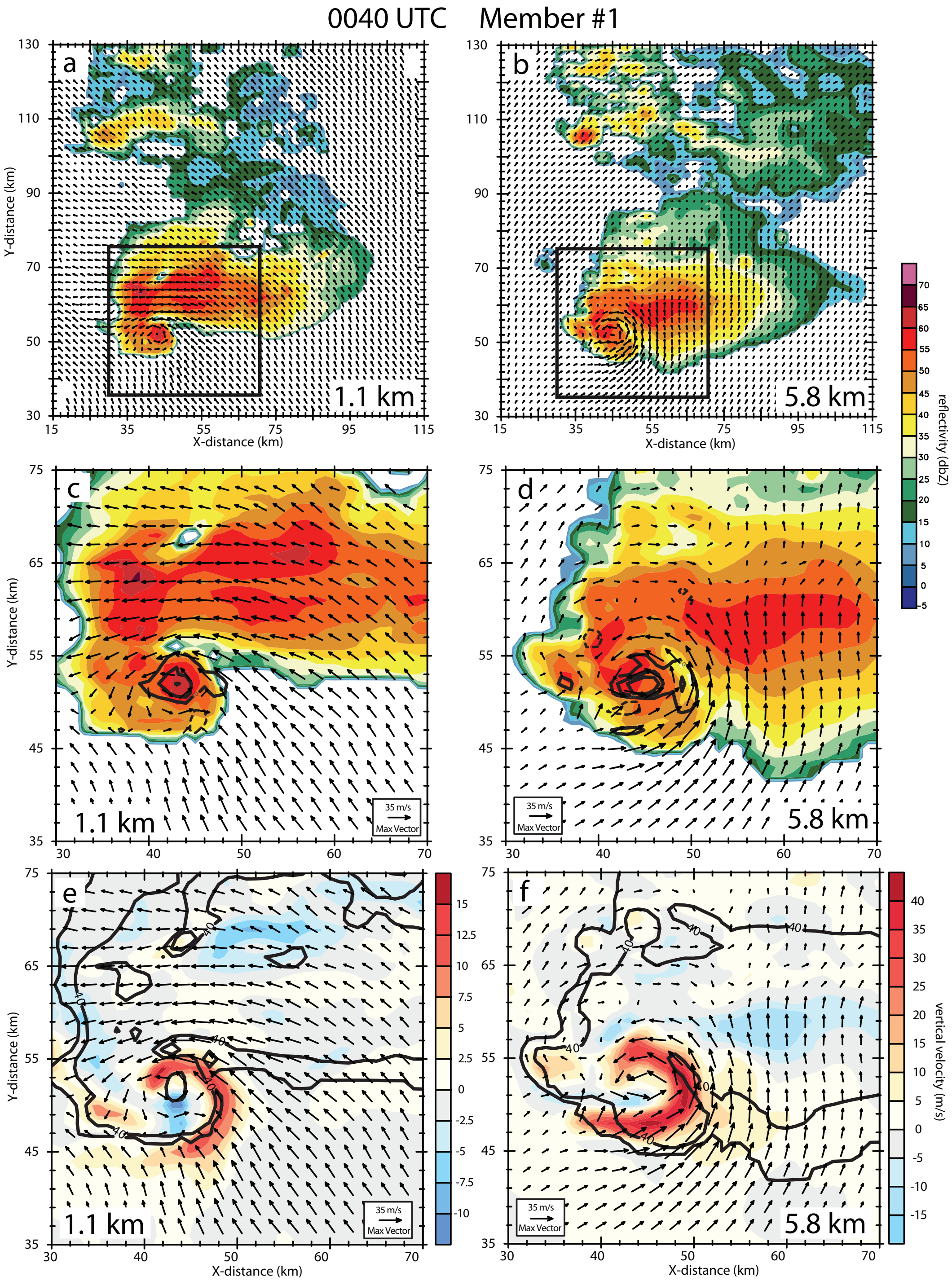

Figure 5.6: (a-b) Reflectivity and wind vectors at 1.1 and 5.8 km AGL at 0040 UTC (94 min). (c-d) Area within box shown in (a-b), reflectivity, wind vectors and contours of vertical velocity every $10 \times 10^{-3} s^{-1}$, beginning at $10 \times 10^{-3} s^{-1}$. (e-f) Color fill indicating vertical velocity, contours of reflectivity every 20 dBZ.

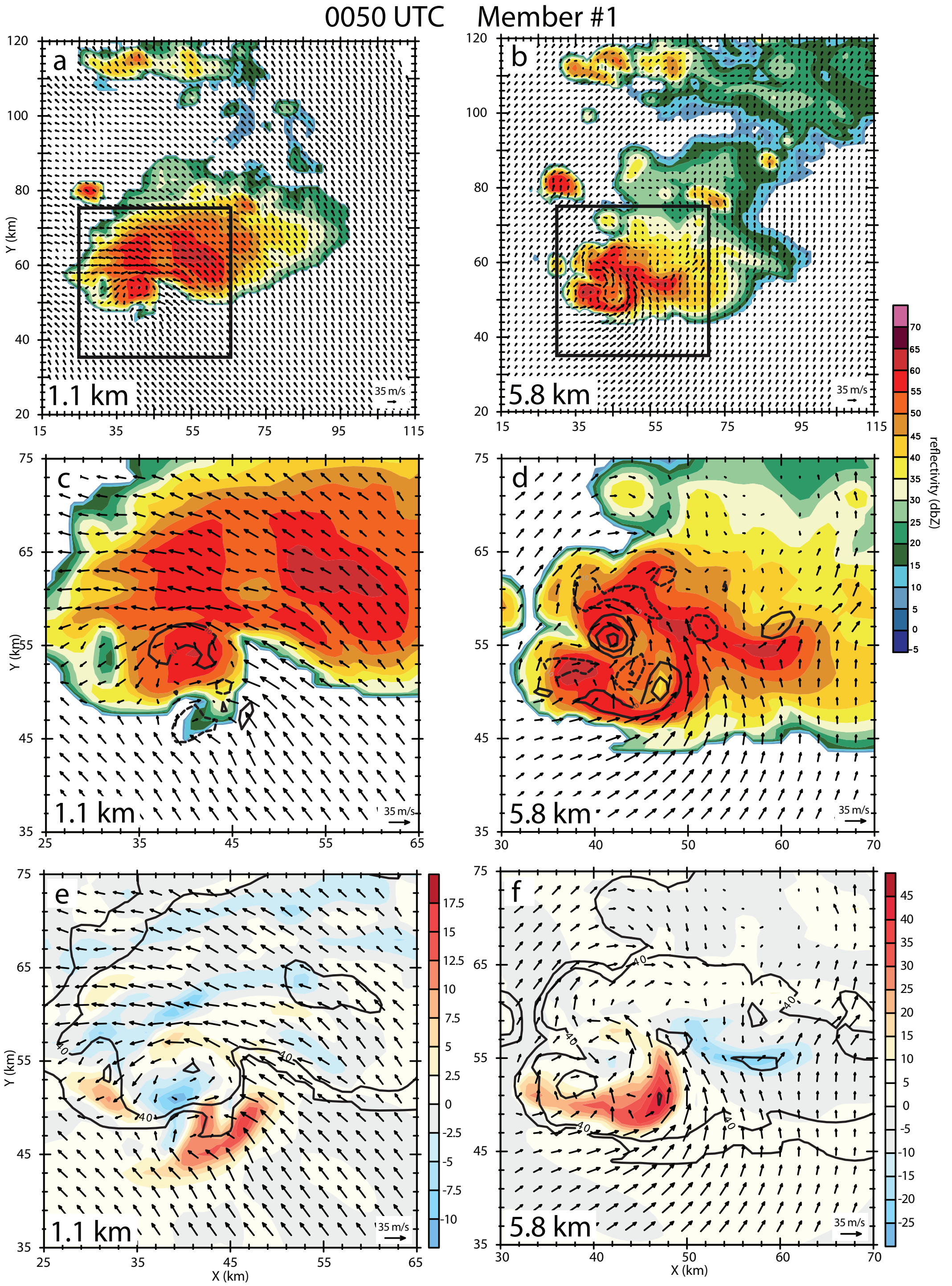

Figure 5.7: (a-b) Reflectivity and wind vectors at 1.1 and 5.8 km AGL at 0050 UTC (104 min). (c-d) Area within box shown in (a-b), reflectivity, wind vectors and contours of vertical velocity every $10 \times 10^{-3}s^{-1}$, beginning at $10 \times 10^{-3}s^{-1}$. (e-f) Color fill indicating vertical velocity. Contours of reflectivity every 20 dBZ.

At 60-70 min into the simulations, the charge structure continued its complex evolution. As charged hydrometeors moved further away from the updraft core, lightning activity neutralized pockets of charge, and some charged hydrometeors recycled through the updraft. As the simulation progressed, there typically was little charge below 4 km in the region of the main updraft. However, from 4 km through storm top in the updraft, there were more than 5 or 6 different charge layers all with small horizontal extent some smaller than 5 km horizontally, all smaller than 10 km. In the downdraft, frequently 6 to 7 different charge layers were present. These tended to be of much longer horizontal extent, reaching as far as 30 km horizontally from the the region of active charging in the main core updraft. Overall, the charge structure at this time and throughout the rest of the simulations remained quite complex, much more elaborate than can be described by a dipole or tripole structure alone (Fig. 5.8e).

Laboratory experiments (Takahashi and Miyawaki 2002; Saunders et al. 2006) show that the graupel within and surrounding the main updraft gains positive charge at warmer temperatures and with higher cloud water content and riming rate (Fig. 5.1). Both positive and negative charging of the large ice hydrometeors occurs within different parts of the main updraft region: on the east side and at the core of the updraft at high liquid water contents the larger ice hydrometeors gained positive charge, while on the periphery of the updraft at lower liquid water contents and on the west side of the updraft at colder temperatures, strong negative charging of graupel and hail is active (Figs. 5.8f and 5.10f).

As seen in Figs. 5.9b and 5.11b, the availability of high liquid water contents in the simulated HP supercell contribute greatly to the positive noninductive charging rates of graupel (and frozen drops). However, this does not cause the storm charge structure to become strictly an inverted vertical tripole, with a positive charge region between two negative charge regions. At middle altitudes, while parts of the storm do contain a net positive polarity charge, substantial parts of the storm at the same altitude

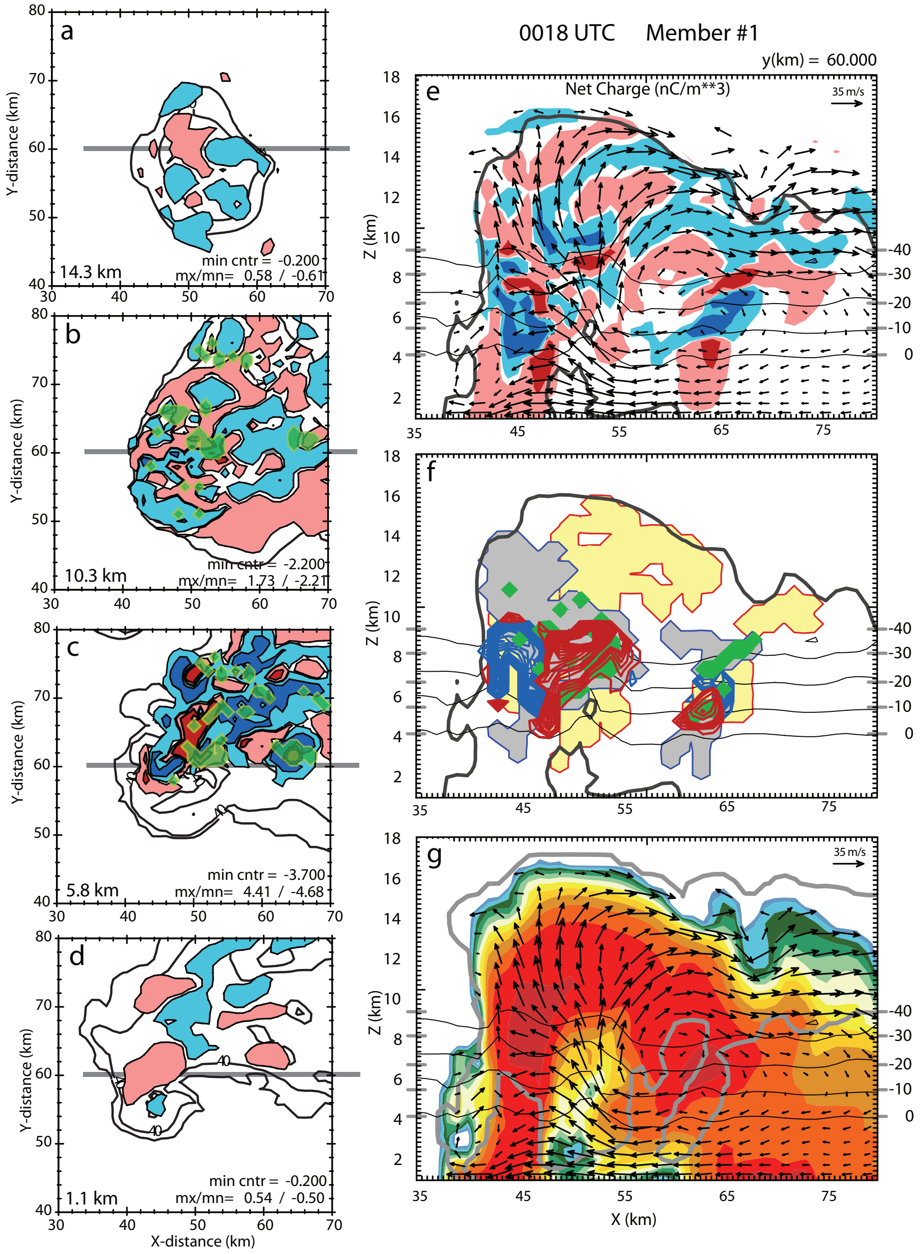

Figure 5.8: Data from ensemble member 1 at 0018 UTC. (a-d) Net charge ($nC\,m^{-3}$) positive(red), negative (blue) and reflectivity contours at 20, 40, and 60 dBZ. Lightning initiation locations surrounding slice in green fill. (a) z=14.3 km (b) z=10.3 km (c) z=5.8 (d) z=1.1 km. (e-g) Cross section through storm at y=60 km. (e) Storm charge ($nC\,m^{-3}$) positive(red), negative (blue)). (f) Noninductive charge separation rates, between graupel and ice crystals-snow. Polarity (red, positive; blue, negative) indicates the sign of charge gained by graupel. Lightning inititation regions (green), areas of of positive leaders (red contour, yellow fill), negative leaders (blue contour, gray fill), and 20 dBZ reflectivity contour also shown. (g) Reflectivity and wind vectors, cloud boundary.

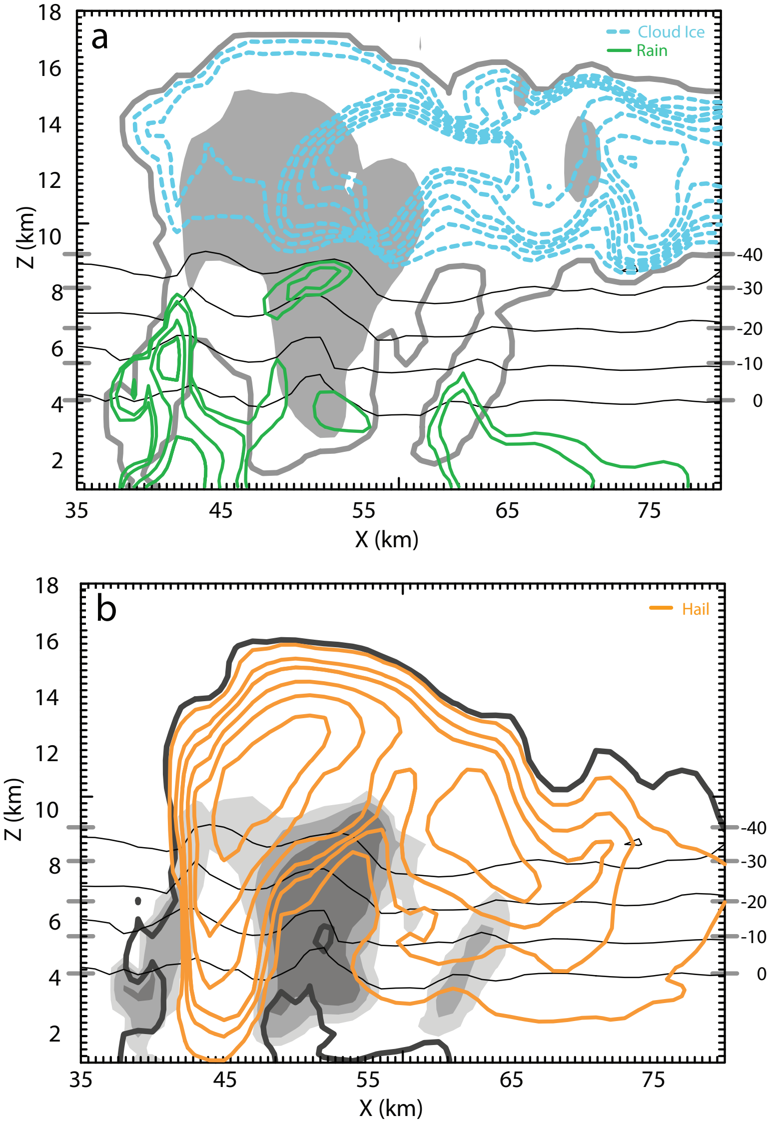

Figure 5.9: Cross-section through member 1 at 0018 UTC (same as shown in Fig. 5.8). (a) Mixing ratio contours of rain (0.5, 1.0, 3.0, 5.0, 9.0, 13.0 g kg^{-1}) and cloud ice (0.5, 1.0, 1.5, 2.0, 4.0 g kg^{-1}). Gray fill indicates areas of updraft $> 15 m\, s^{-1}$). Cloud outline is gray contour. (b) Mixing ratio contours of hail (1.0, 3.0, 5.0, 9.0, 13.0, 17.0 g kg^{-1}). Gray fill is cloud water content (0.1, 0.5, and 1.5 g m^{-3}). 20 dBZ outline is dark gray contour.

contain negative charge instead. Thus, the resulting charge structure at middle levels of the main updraft region cannot be be described as inverted or normal polarity, as inverted and normal polarity structures both exist side by side in parts of the updraft region.

It is the complexity of the charge structure that supports CG flashes of both polarities, as both positive and negative charge regions also exist in different areas of the lowest levels of the storm. Because of this evolving complex charge structure it is quite apparent that the polarity of a particular ground flash depends directly on to the the time and location at which it is initiated. Once electrification was turned on in the simulation, pockets of negative charge consistently existed at lower levels of the storm on the north side, with regions of positive charge just above them. Several studies have suggested that such a charge configuration is conducive to +CG production (e.g., Mansell et al. 2002; MacGorman et al. 2005; Wiens et al. 2005). All CG flashes produced by the simulation between 45 and 70 min were +CG flashes and occurred where this configuration existed. From 75 to 105 min, most CG flashes were -CG flashes, and all -CG flashes occurred within the hook echo and RFD region of the storm through 105 min. At low levels (below 4 km), the majority of the RFD and hook echo region contained positive charge throughout the simulation (Figs. 5.8d, 5.10d, 5.12d), and this is where the −CG flashes connected with ground.

Most simulated flashes were initiated at altitudes between 8 and 11 km, in regions of active charging immediately surrounding the updraft region, with leaders extending out mainly through regions of graupel and hail mixing ratios greater than 1 kg m^3 and very few leaders travel into the ice anvil region. All flashes remained in relatively close proximity to the storm core. As noted by Mansell et al. (2002), MacGorman et al. (2001), and Williams (1985), most lightning propagation is restricted to regions of substantial charge density. Thus, the limited extent of the simulated lightning is consistent with substantial charge densities extending only approximately 30 km from the updraft region in the simulated storm. In order to replicate the anvil lightning seen in the observed storm, an additional charging parameterization, possibly involving ice-ice particle interaction in regions of supersaturation with respect to ice (i.e., Mitzeva et al. 2006), is likely needed.

Occasionally, a secondary region of charging (and lightning activity) occurred, separate from the main updraft region. One example occurred at 0018 UTC and (x, y) = (65 km, 60 km); active charging was at altitudes between 6-8 km, and lightning leaders travelled within an altitude range of 4-10 km (Fig. 5.8f). This secondary region of charging was not located in an updraft region, but occurred within the FFD. During the periods of active charging, a higher concentration of cloud water existed in this region in addition to the large mixing ratios of hail and graupel (Fig. 5.9). This additional region of charging was not common and appeared intermittently in the simulation.

Even though reflectivity values at altitudes between 5 and 7 km were consistently between 30 and 50 dBZ, there was very little to no lightning below 7 km on the southeast side of the storm. As noted above, lightning tends to be restricted to regions of substantial charge density, and the lack of lightning in this region was due to the relative lack of charge in this region. Charging rates on this side of the main updraft core were much lower to non-existent compared to the charging northwest of the main updraft and extending downshear to the northeast. The southeast part of the storm lacked the higher concentrations of water vapor and cloud ice that were present on the northwest side and are necessary for noninductive charging in the model parameterization and in laboratory experiments, as has been discussed previously. At altitudes above 9 km, there was an increase in charge density and lightning activity, though the majority of flash initiations still occurred on the north and northeast side of the updraft core. The distribution of lightning in the observed storm had a similar deficit below 7 km on the south side of storm though not a

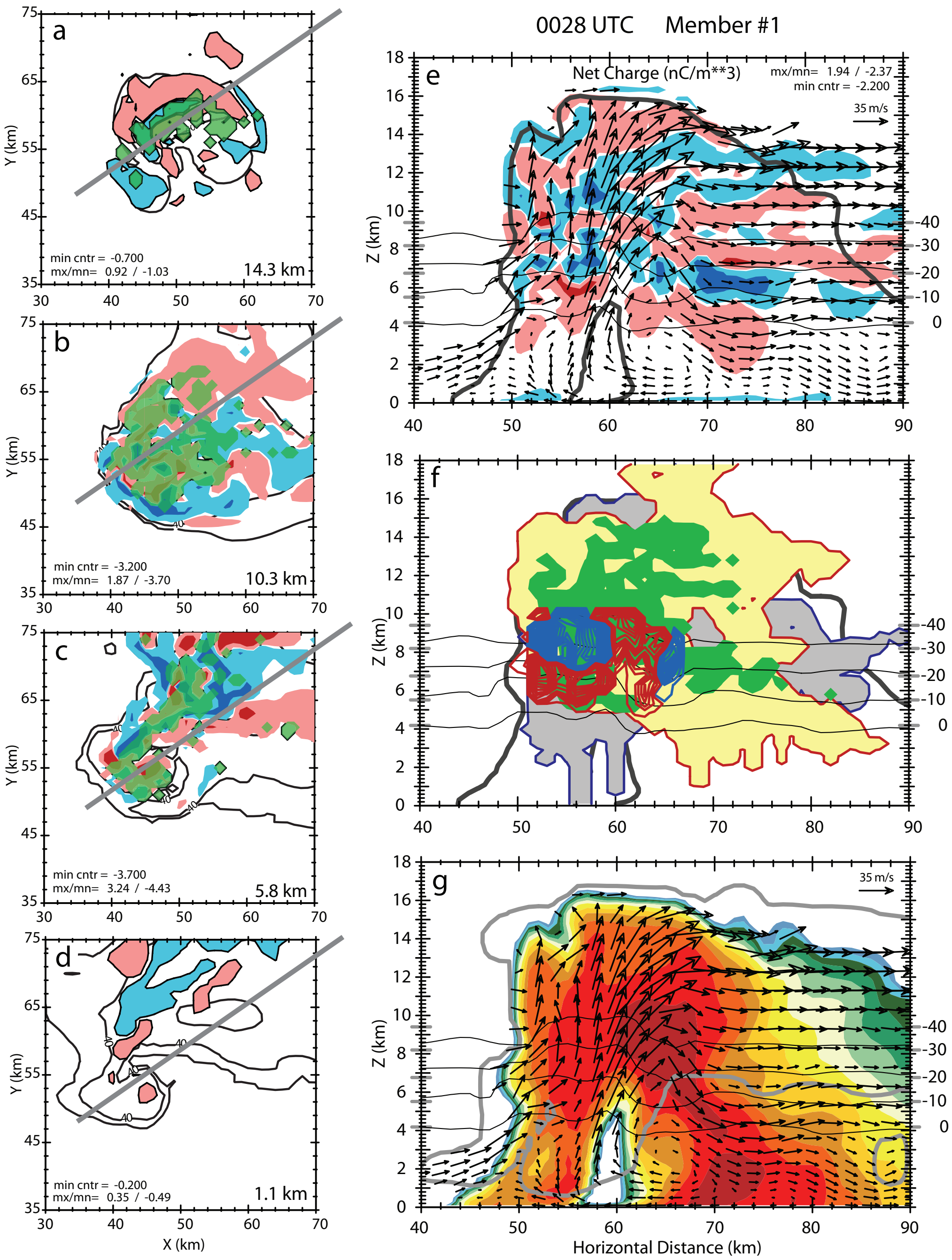

Figure 5.10: Data from ensemble member 1 at 0028 UTC. (a-d) Net charge ($nC\,m^{-3}$) positive(red), negative (blue) and reflectivity contours at 20, 40 and 60 dBZ. Lightning initiation locations surrounding slice in green fill. (a) z=14.3 km (b) z=10.3 km (c) z=5.8 (d) z=1.1 km. (e-g) Cross section through storm at y=60 km. (e) Storm charge ($nC\,m^{-3}$) positive(red), negative (blue)). (f) Charging rate, lightning inititation regions (green), ($nC\,m^{-3}$) positive(red), negative (blue)), and 20 dBZ reflectivity contour. (g) Reflectivity and wind vectors, cloud boundary (gray contour).

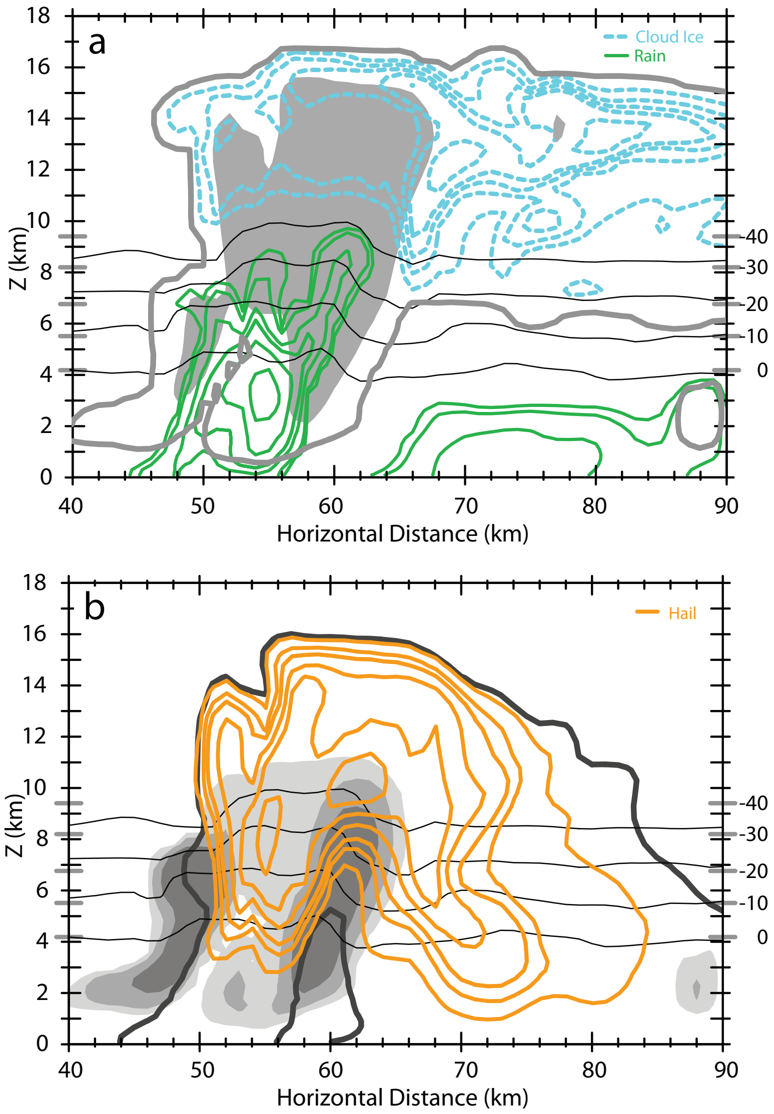

Figure 5.11: Cross-section through member 1 at 0028 UTC (same as shown in Fig. 5.10). (a) Mixing ratio contours of rain (0.5, 1.0, 3.0, 5.0, 9.0, 13.0 g kg^{-1}) and cloud ice (0.5, 1.0, 1.5, 2.0, 4.0 g kg^{-1}). Gray fill indicates areas of updraft $> 15m\,s^{-1}$). Cloud outline is gray contour. (b) Mixing ratio contours of hail (1.0, 3.0, 5.0, 9.0, 13.0, 17.0 g kg^{-1}). Gray fill is cloud water content (0.1, 0.5, and 1.5 g m^{-3}). 20 dBZ outline is dark gray contour.

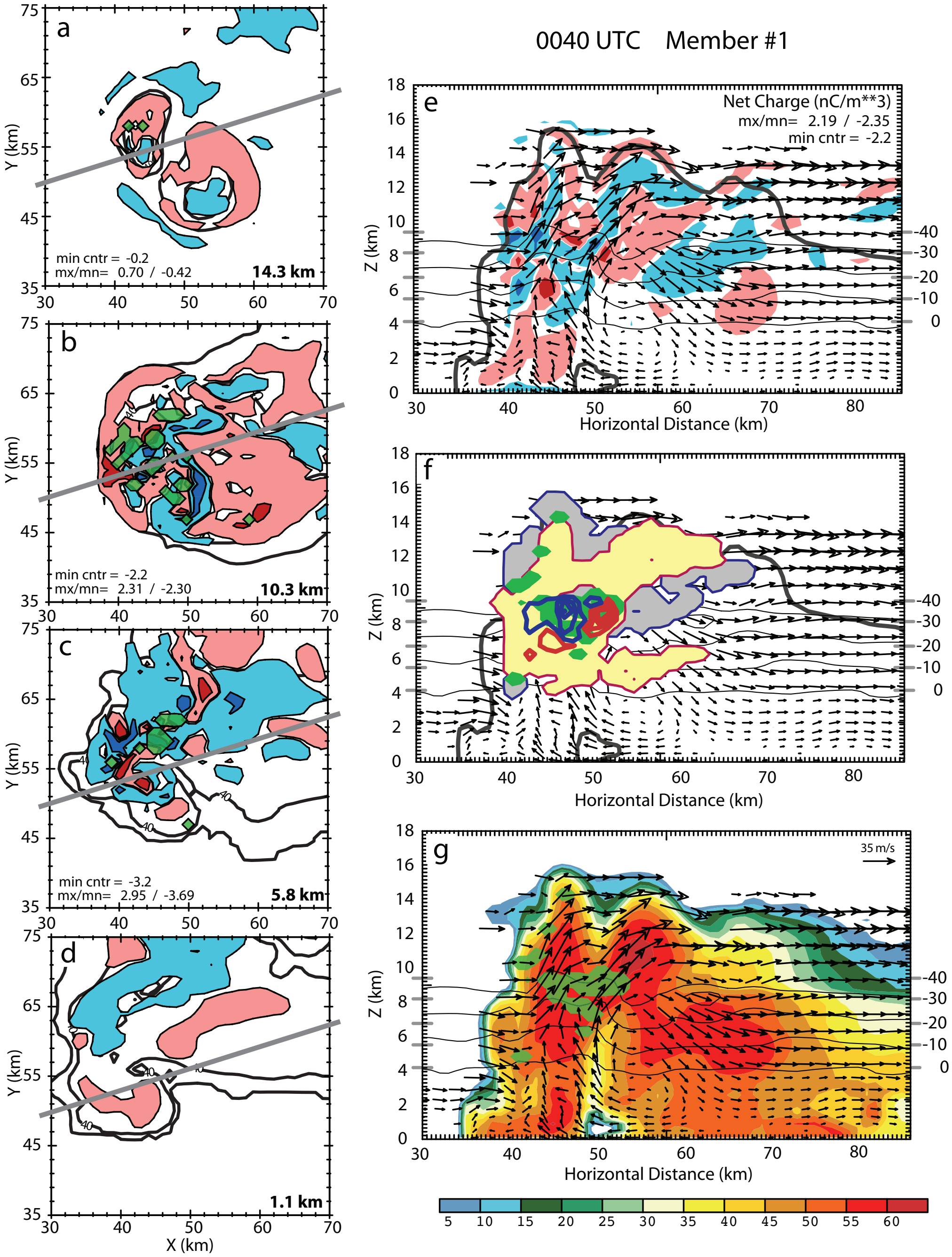

Figure 5.12: Data from ensemble member 1 at 0040 UTC. (a-d) Net charge ($nC\,m^{-3}$) red is positive, blue negative and reflectivity contoured at 20, 40, 60 dbZ. Lightning initiation locations surrounding slice in green fill. (a) 14.3 km (b) 10.3 km (c) 5.8 (d) 1.1 km. (e-g) Cross section through storm at y=60 km. (e) Storm charge (f) Charging rate, lightning inititation regions, 20 dBZ reflectivity contour (g) Reflectivity and wind vectors, cloud boundary.

complete absence as mentioned above. The increase in lightning activity between 9-11 km in the observation was much greater than what was produced within the simulations. It is possible that both discrepancies were a consequence of the model tracking only the mean motion of each particle category and so missing trajectories of larger and smaller particles. The lack of a lightning maximum at higher altitudes may also have been caused by charging under some conditions of low-liquid water content not accounted for in the noninductive charging parameterization, as noted previously.

Because lightning channels propagate mainly in regions of larger charge density, the structure of individual flashes tends to mirror the appearance of the charge structure. The majority of both observed and simulated flashes were small and were contained within the region of the main updraft core. More than 65% of the flashes were less than 10 km in total channel length, and more than 55% spanned 5 km or less. Less than 3% of simulated flashes were connected more than 200 grid points along the total lightning branches contained within an individual flash and so might correspond to the extra long category of observed flashes. Though these extra long flashes were relatively rare and there was some scatter in where they were initiated, the majority were initiated in the north-to-northeast part of the storm within reflectivity of 55-60 dBZ at roughly 9-12 km in height. Like the region with predominately smaller flashes, the region with very large flashes tended to receive a continuous influx of charge from the active charging surrounding the main updraft. However, unlike the small pockets of opposing charge in the updraft region, this region of the storm contained larger, more continuous horizontal regions of each charge polarity that allowed flash leaders to propagate farther before terminating.

As in the observed storm, a transient lightning hole was present in all electrified members of the simulations. The lightning hole appeared at similar times in the different members, generally within 2-3 minutes of each other. However, some members contained larger and more persistent holes than other members. A lightning hole type feature first appeared around 2355-0010 UTC in a couple of the members, with another short lived one appearing around 0015-0023 in almost all of the electrified members. The feature was not seen again until 0038 UTC in member 1 and then appears again in all the members around 0048-0054 UTC.

The lightning hole produced by Member 1 near the end of the simulation at 0049-0052 UTC corresponded with the BWER (on the southeast edge) and with the main updraft core (Fig. 5.14), as was noted in the dual-Doppler and LMA analysis in Chapter 3. The charge density in the lightning hole, while not zero, was smaller during this time frame than during periods not containing a lightning hole. There was a complete absence of charge and active noninductive charging below 8 km through the region where the updraft was greater that 40 ms^{-1} (Fig. 5.15). The central region of the lightning hole lacked significant concentrations of large ice particles; mixing ratios for hail were below 2 g kg^{-1} in the center of the hole.

The height of flash initiations in the simulations were similar to those in the observed storm. Throughout the simulation, the peak activity remains around 10 km (maxima typically at the 9.8 and 10.3 km grid heights) (Fig. 5.13), roughly the same height as for the majority of lightning activity in the observed storm. This height also marks the boundary between large concentrations of cloud ice (above) and regions of rain and cloud vapor below (Fig. 5.11a). During the time of early electrification (prior to 60 min), this region above 10 km consisted primarily of positive lightning breakdown through regions of negative charge attached to the cloud ice. As the simulations progressed, the majority of initiations remained near 10 km, though, as mentioned previously, depending on the specific region of the updraft, cloud ice gained either positive or negative charge so the region above 10 km did not consist of primarily positive or negative charge (e.g., Fig. 5.10e). More importantly than the specific charge attached to the hydrometeors, the region of peak initiations was

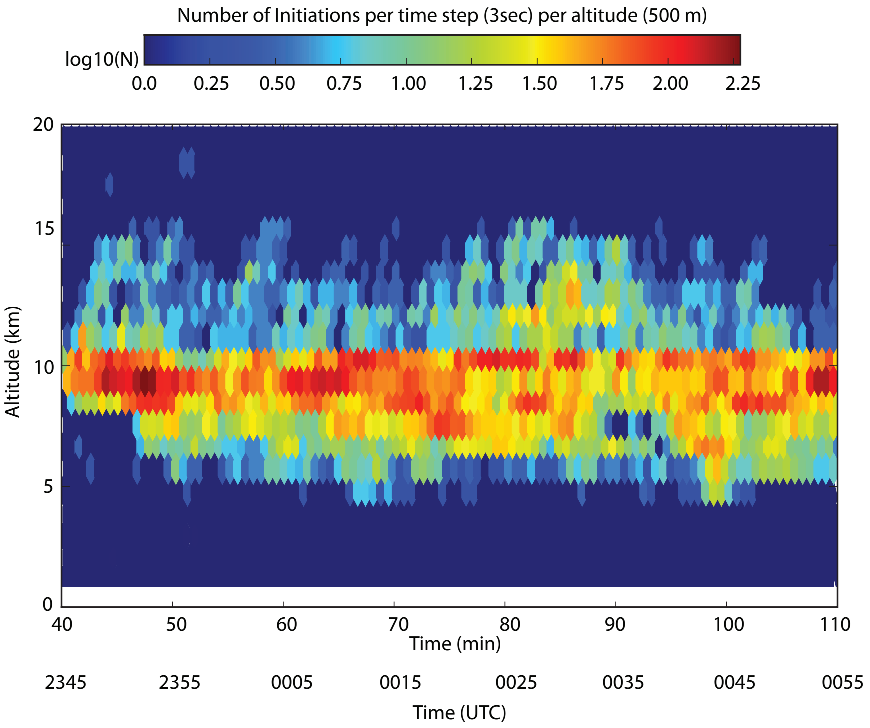

Figure 5.13: Log density plot of initiations per time step (3 sec) per grid height (500 m) over the time of active electrification in Member 1.

specifically on the boundary between cloud ice (above) and within the region of highest mixing ratios of graupel and hail around -30 to -40°C in the storm core within and just above the region of highest charging rates.

High-altitude lightning, though usually infrequent, did occur in the simulations, as in the observed storm. Less than 3% of the total flashes began at heights greater than 13 km. Above 15 km, the percentage was even smaller, 0.3% of all flashes in the storm. Lightning initiations at these heights were directly above the main updraft region, with velocities greater than 35 $m\,s^{-1}$ reaching at least 13 km in the overshooting top, where these lightning initiations occurred. However, unlike the uniformly small flashes actually observed in the overshooting storm top, the simulated high-altitude flashes varied quite a bit in size: the smallest had only 2-3 km in total leader length (adding together the length of all channel steps, including those in all branches) and the largest covered over 150 km by the total leader propagation. The size of the majority of high-altitude flashes was somewhere in the middle, typically less than 45 km of total leader channel length. After initiation, leaders normally followed the cloud boundary directly down shear from the overshooting top and tapped the charge regions advected downshear from the main updraft. It appears that the lightning in this region was most commonly initiated between charge regions of opposite polarity created within the the updraft core at temperatures warmer than -40 C. The charge was lofted above 14 km due to the size and strength of the updraft at the time. Occasionally, the lightning was possibly initiated between the screening layer charge at the cloud boundary and upper charge transferred by the noninductive mechanism to cloud particles, though this was quite rare.

5.3.2.2 Flash rates, microphysics, and charge generation

The pattern of evolution of flash rates in the simulated storm had features similar to those of the observed storm. As in the observed storm, the simulations, did not maintain uniformly high flash rates continuously. Instead flash rates had similar episodic behaviour in each simulation, with smaller flash rates between 2355 and 0000 UTC and again from 0030-0040 UTC. The second period of smaller flash rates occurred during the same period as a decrease in updraft mass flux and graupel volume in the simulation (Fig. 5.18). However, the correspondence with kinematic properties was not as clear for the first period of smaller flash rates. Although updraft mass flux decreased slightly during the period of the first decrease in flash rate, the flash rate increases quickly between 0000 and 0005 UTC without a corresponding response in mass flux or graupel volume.

The simulations also captured an increase in the rate of flash initiations at lower elevations and an increase in $-$CG flash rates, both of which occurred in the observed storm around 0040 UTC. In the simulations, these flash rate increases occurred at about the same time as updraft mass flux and graupel volume began to increase

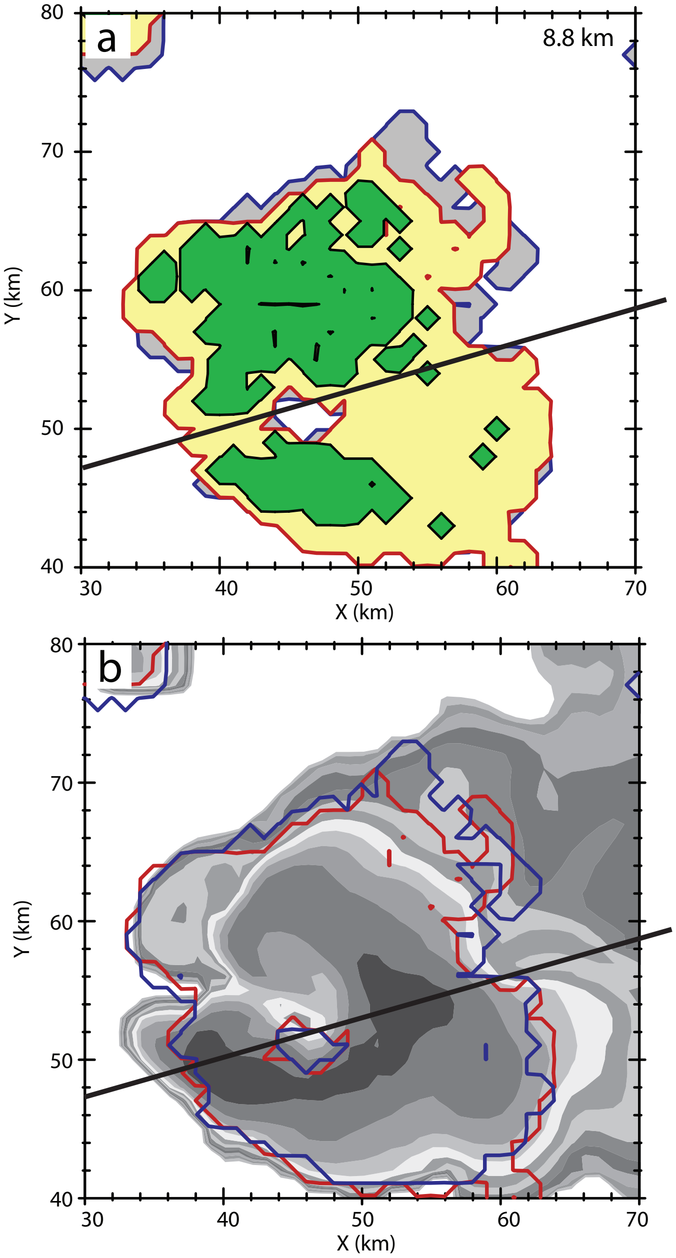

Figure 5.14: Data from ensemble member 1 at 0050 UTC or 72 min into simulation. (a) Composite of lightning initiations (green), positive leaders (yellow fill, red contour), and negative leaders (gray fill, blue contour) within 2.5 km from 8.8 km. (b) Reflectivity at 8.8 km (grayscale) with positive (red) and negative (blue) leaders contoured.

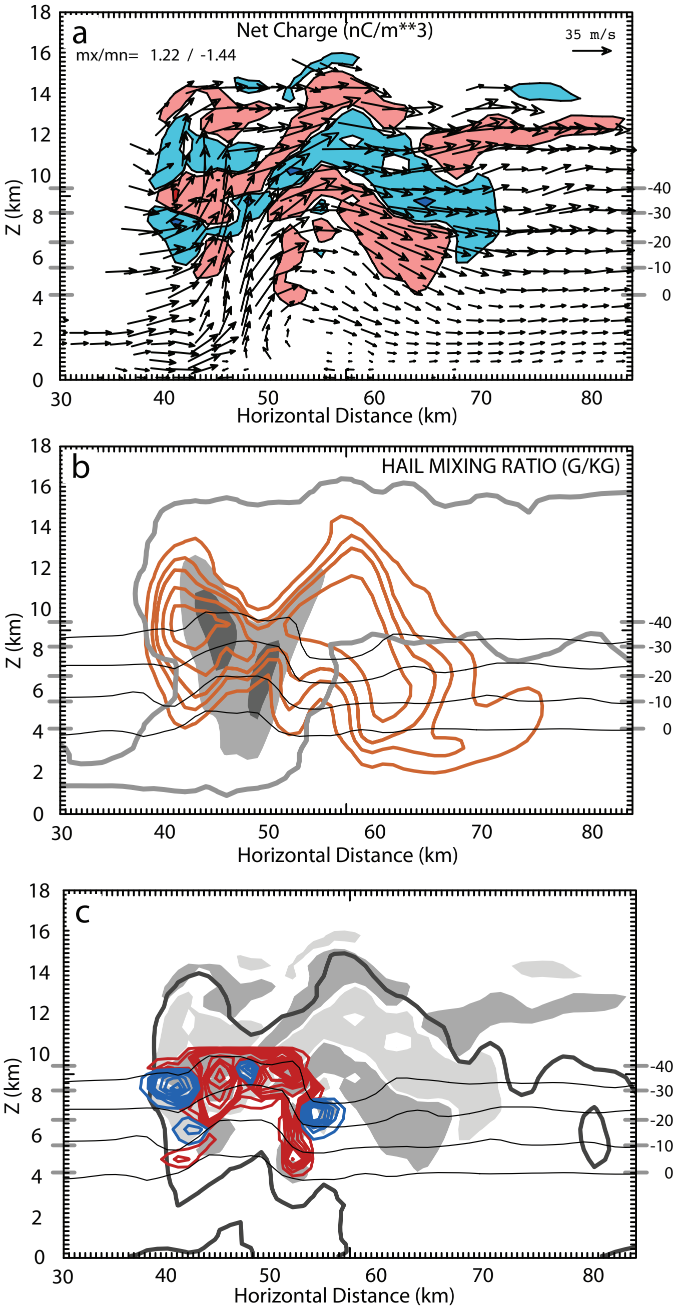

Figure 5.15: Data from ensemble member 1 at 0050 UTC or 72 min into simulation. (a) Net Charge density, positive (red) and negative (blue) and wind vectors. (b) Contours of hail mixing ratio (orange), cloud outline (gray) and gray fill of vertical velocity at 25 and 40 ms^{-1} (light and dark gray, respective). (c) Contours of noninductive charging rate of graupel/hail, positive (red) and negative (blue) and 20 dBZ reflectivity (dark gray). Gray fill of negative (light) and positive (dark gray) charge density. Cross-section for all panels is along solid black line in Fig. 5.14.

again, though the increase was not to the levels seen earlier in the simulations. Note, however, that the CG lightning rate of the simulations is hampered by the parameterization as there is a known lack of CG lightning that the parameterizations are able to produce (Mansell et al. 2002). So, while the −CG rate for the observed storm at this time was 10-15 per min, the simulations never produced more than 3 CG flashes per minute.

Being a high precipitation supercell, this storm simulation had quite high concentrations of large ice hydrometeors (Fig. 5.9 and 5.11), considerably higher than produced by our previous simulations of classic supercells. The large concentratons of precipitating ice contributed to a larger noninductive charging rate (Figs. 5.8f and 5.10f), ultimately providing the the large rate of charge replenishment needed to maintain the extremely large flash rates produced – both in the simulations (all electrified members) and the observed storm (Fig. 5.16). Throughout the analyzed period, flash rates remain above 200 per minute and at times peaked at 400-600 flashes per minute. (Note, however, that the first peak near 700 flashes per minute occurred at the beginning of the analyzed period, between 2345-2355 UTC, shortly after electrification was turned on, and so may have been inflated by artifacts relating to the sudden start of electrification.) Peak flash rates in the observed storm were 450-500 per minute. Peaks in simulated flash rates of 400-600 flashes per minute have not been common for this parameterization during simulations of other supercell storms. In previous supercell simulations, the maximum flash rate has been closer to 200 flashes per minute with mean levels around 75 flashes per minute (e.g., Kuhlman et al. 2006b). The difference from previous simulations. and the probable cause of large flash rates in the present simulations, were the very large amount of precipitating ice in the mixed phase region and the very large updraft mass flux.

As mentioned in the previous section, the majority of flashes in the simulated storm had relatively small total channel lengths per flash, a result of the complex charge structure and small pockets of charge limiting the leader length for a flash. The combination of the small amount of charge neutralized by each of these flashes, the large noninductive charging rates, and the rapid charge replenishment provided by the large updraft mass flux were what enabled such high flash rates to continue throughout the simulation in a manner similar to that of the observed storm.

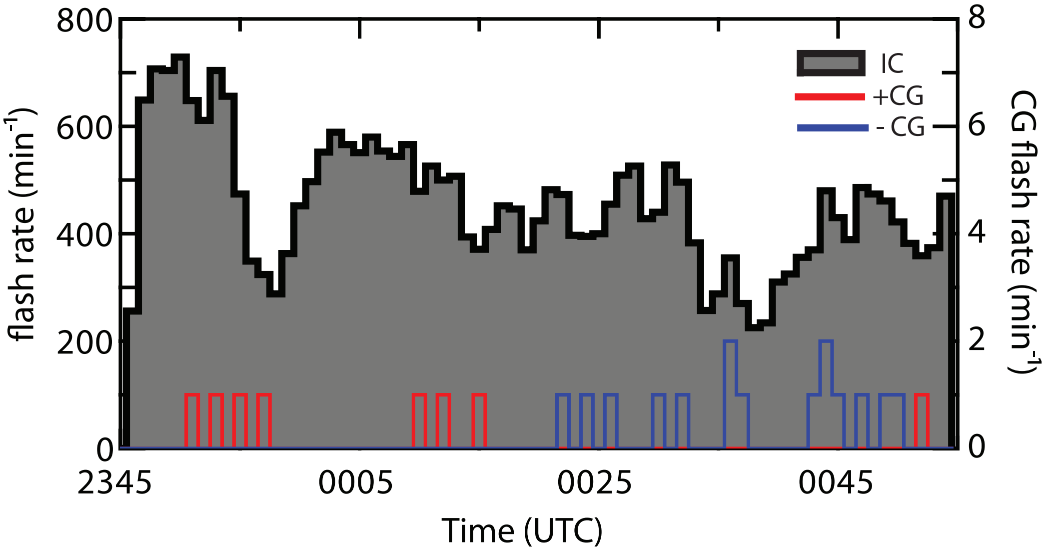

Figure 5.16: Flash rate from member 1. Note: electrification not turned on until 2345 UTC.

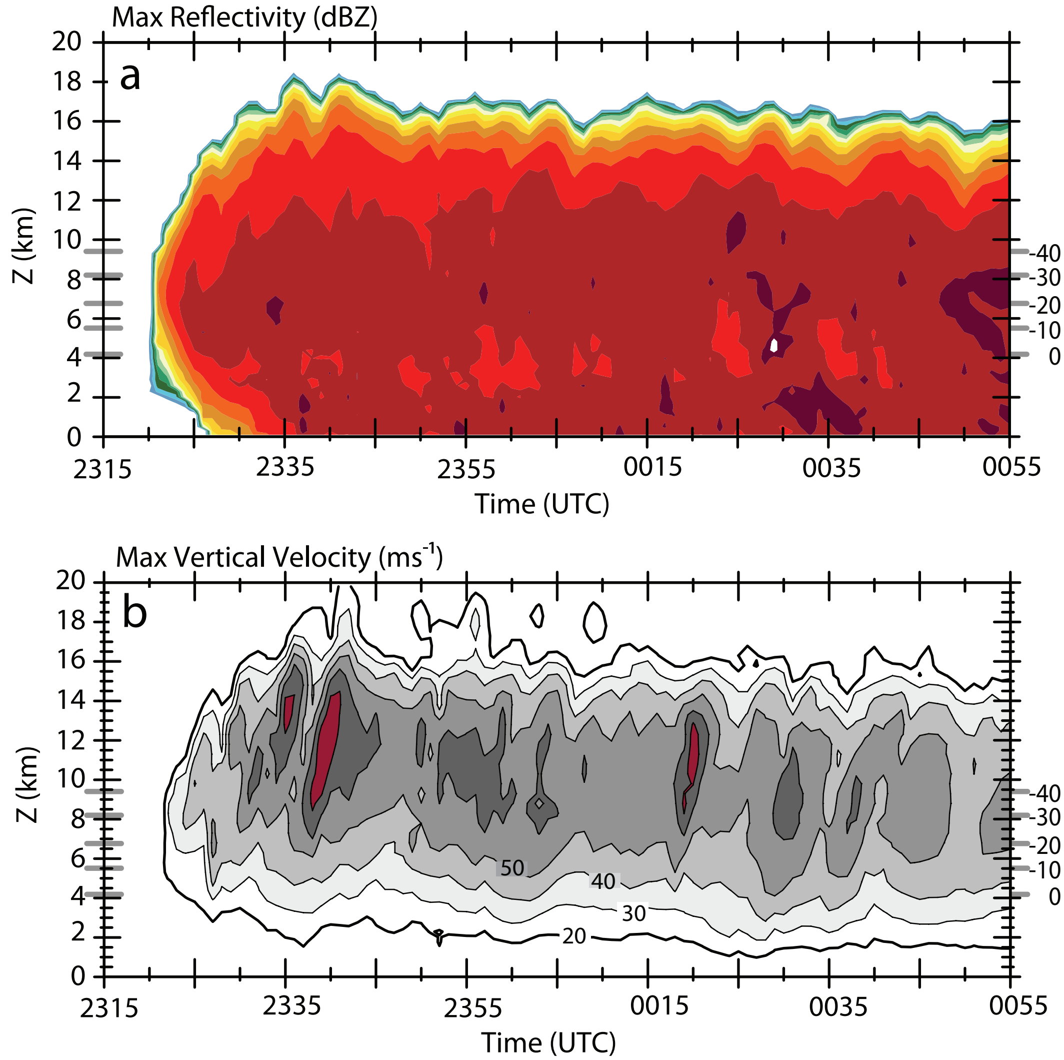

Figure 5.17: Time-height plots of maximum reflectivity every 5 dBZ through 75 dBZ (top) and vertical velocity contoured every 10 ms^{-1} beginning at 20 ms^{-1} (bottom).

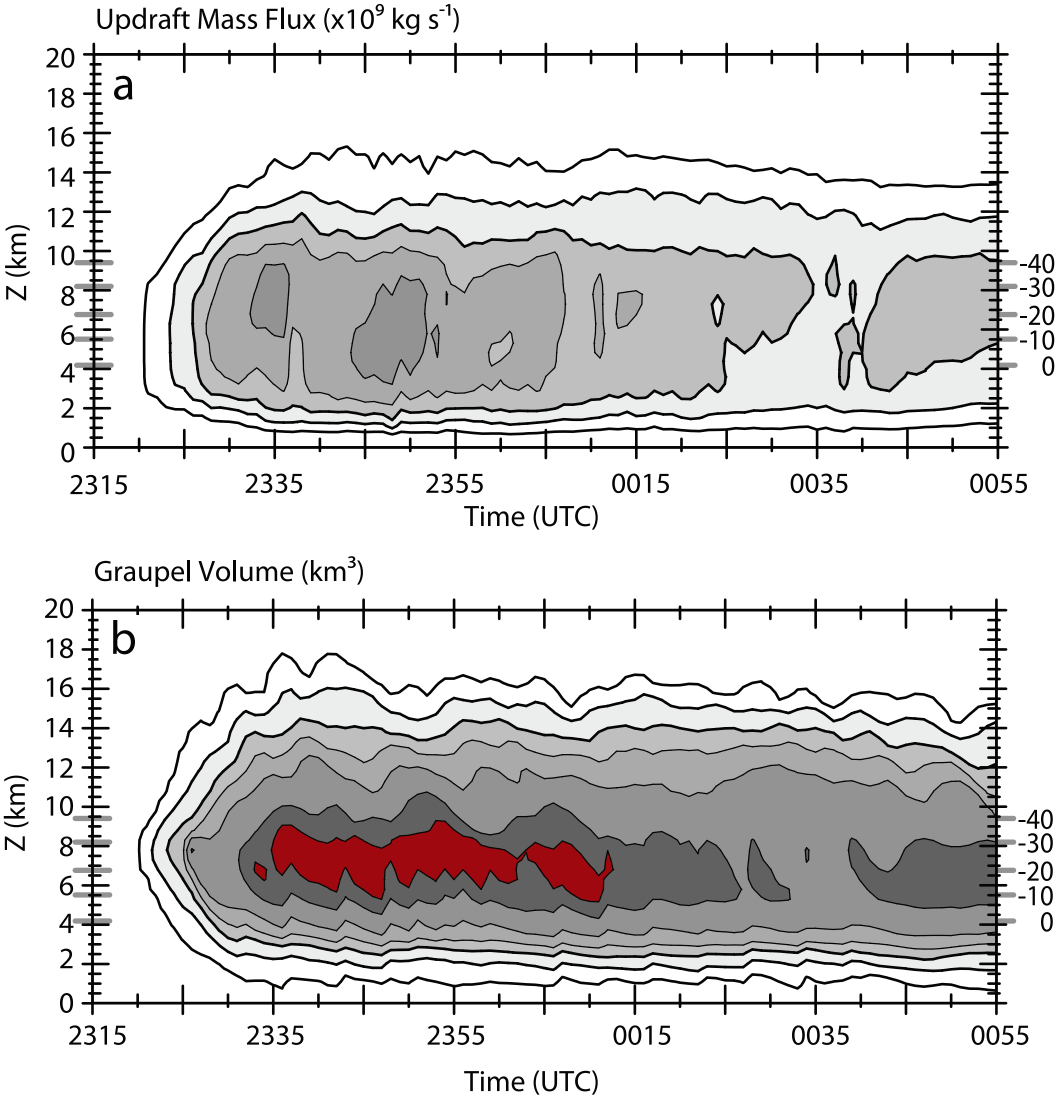

Figure 5.18: Time-height plots of updraft mass flux every 1×10^9 $kg\,s^{-1}$ beginning at 1×10^9 $kg\,s^{-1}$ (top) and graupel volume contoured at 5, 50, 125, 200, 300, 450 and 550 km^3 (bottom) .

Chapter 6

Summary and Conclusions

Analysis has been presented of both the observations and simulations of a long-lived, high-precipitation supercell that occurred on 29-30 May 2009. The observational study employed measurements from a lightning mapping array, an in situ electric field sounding, and two C-band mobile radars. The simulations employed an ensemble Kalman filter method for data assimilation of reflectivity and velocity of one of the mobile radars and a cloud model with parameterizations for electrification and lightning. The results from the simulations were compared with analyses of dual-Doppler and lightning observations. (For the reader's convenience, the results are also summarized relative to the hypotheses stated in Chapter 1 in a table included at the end of this chapter.)

As seen in previous simulations and discussed throughout this dissertation, the dipole or tripole charge structure may work for a small single cell storm, but it is much too simple to describe the actual charge structure of a supercell storm. The charge structure seen in the simulations of this storm depicted small regions of opposite charge tightly packed in the storm core, where the maxima of lightning initiations took place. Areas downshear contained larger, more continuous, horizontal regions of each charge polarity. This complex charge structure, created primarily through noninductive charging modified by the frequent lightning was responsible for many of the electrical features seen during the evolution of the supercell.

As noted in both the observations and the simulations, this supercell produced extremely large flash rates, dominated by flashes in the inner core of the storm that were small in overall leader extent. The updraft core was the predominant region of active charging and when combined with the turbulence due to updraft/downdraft interaction led to small pockets of high charge density of opposite sign in close proximity to each other. The resultant strong electric fields allowed frequent flash initiation, but the leaders in these flashes had little room to travel before reaching an area of unfavorable charge. Moving away from the storm core and into the anvil region, regions of charge were larger with greater areal extent, and this allowed flashes to travel farther without termination.

It is this region of maximum flash rate, surrounding and just downshear from the updraft core in both the observed and simulated storms, that is representative of the region of maximum charge replenishment. Due to the strong, persistent and sizable updraft, the peak region of flash initiations in both the observed and simulated storms was centered near 10 km, higher in altitude than observed or simulated for less severe storms. In the simulations, this region contained of the highest concentrations of large ice hydrometeors (graupel and hail) overlapping the edge of the cloud ice concentrations just above. The highest noninductive charging rates occurred coincident with or immediately below this region, in and surrounding the main updraft, in regions of high liquid water contents. Noninductive charging led to both positive (negative) and negative (positive) charging of graupel (cloud ice) in and around the main updraft, with the polarity depending on the temperature and liquid water content of the region. Due to the decidedly high concentrations of ice hydrometeors and cloud water content, combined with the large, steady updraft for this HP supercell (reflected in the large values of updraft mass flux), the charging rates maintained throughout the simulations were at a consistently high level.

These high noninductive charging rates of both polarities for large ice hydrometeors, combined with the added complexity of hydrometeors moving away from the updraft core, turbulence with updraft/downdraft interaction, lightning activity neutralizing pockets of charge, and some charged hydrometeors recycling through the updraft, produced a highly complex charge structure, which could not be characterized simply as having normal or inverted vertical polarity. The presence of both −CG and +CG flashes in both the observations and simulations is a direct result: different regions had different polarities of charge at the lowest levels; −CG flashes occurred in regions having a lower positive charge and +CG flashes occurred in regions with a the lower negative charge.

A lightning hole was noted in both the observations and simulations of the 29-30 May 2004 supercell. In both cases, the lightning hole was co-located with the BWER and maxima of the updraft, though not taking on the same exact shape of either. The dual-Doppler analyses depicted divergence and circulation around the lightning hole, suggesting that charged hydrometeors were actually being swept out from and around this area. Though the lightning hole in the simulations was not as consistently present as in the observations, during the times that it was present there was a complete absence of charge and active noninductive charging through the region of the main updraft core below the hole. Vertical velocity in the region of the lightning hole in the simulations was generally greater than 40 ms^{-1}.

Directly above the main updraft core, there was evidence of high-altitude lightning in the overshooting top within both the observations and the simulations. The observational data from the LMA contained a distinct signature of consistent, singular, VHF sources that were too far apart in time and space to be associated as a single flash. These VHF sources above 16 km did not correspond systematically to flashes lower in the storm. Thus, it appears that flashes contained in the overshooting top were a separate entity from those in the storm core just below. A comparison with dual-doppler data indicated that these isolated points were concentrated directly above the main updraft and BWER. Typically between 16 and 18 km, the region containing these upper LMA points took on a rounded-cap appearance in the overshooting top, with the highest point directly above the region of largest, most vertical updraft, then tilting downward east of the overshooting top, along the vertical gradient in reflectivity. The breakeven electric field was lower at the altitude of these continual VHF emissions (15-18 km), and therefore, combined with the lofted charge from the updraft core into the overshooting top and possible interaction with the screening layer charge, likely allowed the high discharges that produced the high VHF sources to occur there. The simulations reproduced the high-altitude lightning seen in the observations, though its nature was slightly different from what was observed. The simulated flashes were typically of greater temporal extent than the singular VHF emissions seen by the LMA (note: simulated flashes are at least 1 km in length due to grid resolution) – simulated flashes were generally around 45 km in total leader length, though they ranged as small as 2-3 km or as large as 150 km in total branching length. What simulated high flashes did have in common with observed flashes, however, was being initiated at similar altitudes directly above the main updraft region, here velocities greater than 35 $m\,s^{-1}$, reached at least 13 km. Consistent with the distribution of mapped VHF sources, simulated leaders typically followed the reflectivity gradient downward east-northeast from the overshooting top.

Previous studies of lightning of thunderstorm anvils have reported that flashes began in or near the storm core and propagated downwind into the anvil. It had been thought that flashes could not be initiated far downwind in the anvil, because anvil charge was thought to be produced mainly in the storm's deep updraft and to decrease with distance into the anvil. However, the observations from 29-30 May 2004 depicted many flashes originating in the anvil region and propagating back towards the storm core. The earliest anvil-initiated flashes in the analyzed period were likely caused by the confluence of charge of opposite polarity from the two anvils. However, converging anvils cannot explain initiation in the anvil at earlier or later times, as occurred in the distant northern anvil before it was influenced significantly by the southern storm, and also occurred in the distant southern anvil long after the northern storm stopped producing lightning and had completely dissipated. In both situations, it was observed that lightning can occur farther from deep convection and more frequently than would be expected from charge transport alone: either each flash removed relatively little charge from those regions of the anvil, or the charge was replenished within roughly 10-30 s, which is too little time for charge transport from the storm updraft core across the region of anvil lightning activity. The storm simulations did not contain any type of charge in the anvil region beyond 30 km from the storm core and thus did not reproduce any of the anvil lightning seen in the observations. It seems likely that some charging mechanism besides the included noninductive graupel-ice mechanism was active inside the anvil, such as charging by ice-ice particle interactions in regions of supersaturation with respect to ice, as discussed by Mitzeva et al. (2006) and Dye and Willett (2007). Table 6.1 (below) summarizes those findings of this study which addressed questions raised in the introductory section of this dissertation.

Table 6.1: Questions posed in this Dissertation

Question	**Answered?**
Trends in charge generation are reflected by the magnitudes and trends of flash rates?	Yes. Both the observed and simulated storms produced and maintained flash rates of several hundred per minute. The simulations contained extremely large noninductive charging rates that allowed charge to be replenished rapidly after it was neutralized by lightning.
Lightning in supercell storms is dominated by flashes that are shorter in time and horizontal extent?	Yes. Flashes in the inner core were the most frequent and these also had the smallest duration and spatial extent. Typically, the flash duration and horizontal extent increased as distance increased from the updraft core.
Do updraft strength and size control the overall polarity of the storm and the polarity of ground flashes?	Somewhat. From the simulations, it was seen that the continuous presence of a large, strong updraft in this storm allowed a large, continuous rate of noninductive charging. It also contributed to the high water contents in the updraft core, which caused positive charging to graupel, while lower rime accretion rates on the periphery of the updraft caused negative charging to graupel. This created a complex charge structure that allowed both negative and positive CG flashes to be produced by the storm.

Continued on next page

Question	**Answered?**
Lightning holes are caused by the lack of charged hydrometeors?	Yes. Both the observations and simulations showed the lightning hole was co-located with the main updraft core and BWER. The simuations further showed the larger concentrations of large ice particles were surrounding and at higher altitudes of the most intense section of the updraft and were in areas of convergence downshear. Lightning was more frequent in these regions of charge and avoided regions having little or no net charge.
Discharges above the equilibrium level are caused by updraft impulses.	Mostly. It seems like that updraft impulses play an important role, but in both the observed and simulated storm, the updraft consistently was strong and lofted charge to at least 16 km. At these upper levels, charge in the updraft may have interacted with screening layer charge produced at the cloud boundary, and the threshold for the breakeven electric field magnitude is smaller; both factors likely contributed to the continual discharges in this region of this storm.

Continued on next page

Question	**Answered?**
How, why, and what type of lightning is initiated in supercell anvils?	Yes. Unlike the anvil lightning flashes reported previously, which were initiated in or near the storm core and propagated farther into the anvil, many flashes observed in our study were initiated in the anvil and propagated back towards the core. Roughly half of the flashes in this region were −CG flashes. Anvil-initiated flashes were likely casued by (1) convergence of two charge regions of opposite polarity at the same altitude from two converging anvils or by (2) additional charging in the anvil (away from the updraft core).

Bibliography

Adlerman, E. J. and K. K. Droegemeier, 2002: The sensitivity of numerically simulated cyclic mesocyclogenesis to variations in model physical and computational parameters. *Mon. Wea. Rev.*, **130**, 2671–2691.

Baker, H. B., H. J. Christian, and J. Latham, 1995: A computational study of the relationships linking lightning frequency and other thundercloud parameters. *Quart. J. Roy. Meteor. Soc.*, **99**, 10627–10632.

Biagi, C. J., K. L. Cummins, K. E. Kehoe, and E. P. Krider, 2007: National lightning detection network NLDN performance in southern Arizona, Texas, and Oklahoma in 2003-2004. *J. Geophys. Res.*, **112**, doi:10.1029/2006JD007341.

Biggerstaff, M. I., L. J. Wicker, J. Guynes, C. L. Ziegler, J. M. Straka, E. N. Rasmussen, A. Doggett, L. D. Carey, J. L. Schroeder, and C. Weiss, 2005: The Shared Mobile Atmospheric Research and Teaching radar: A collaboration to enhance research and teaching. *Bull. Amer. Meteor. Soc.*, **86**, 1263–1274.

Bluestein, H. B. and D. R. MacGorman, 1998: Evolution of cloud-to-ground lightning characteristics and storm structure in the Spearman, Texas, tornadic supercells of 31 May 1990. *Mon. Wea. Rev.*, **126**, 1451–1461.

Bluestein, H. B. and C. R. Parks, 1983: A synoptic and photographic climatology of low-precipitation severe thunderstorms in the Southern Plains. *Mon. Wea. Rev.*, **111**, 2034–2046.

Boccippio, D. J., K. L. Cummins, H. J. Christian, and S. J. Goodman, 2001: Combined satellite- and surface-based estimation of the intracloud-cloud-to-ground lightning ration over the continental United States. *Mon. Wea. Rev.*, **129**, 108–122.

Brandes, E. A., 1977: Flow in severe thunderstorms observed by dual-Doppler radar. *Mon. Wea. Rev.*, **105**, 113–120.

Branick, M. L. and C. A. Doswell, III, 1992: An observation of the relationship between supercell structure and lightning ground strike polarity. *Wea. Forecasting*, **7**, 143–149.

Bridenstine, P. V., C. B. Darden, J. Burks, and S. J. Goodman, 2005: The application of total lightning data in the warning decision making process. *First Conference* *on Meteorological Applications of Lightning Data*, Amer. Meteor. Soc., San Diego, CA, P1.2, 3 pp.

Brooks, I. M. and C. P. R. Saunders, 1994: An experimental investigation of the inductive mechanism of thunderstorm electrification. *J. Geophys. Res.*, **99**, 10627–10632.

— 1995: Thunderstorm charging: Laboratory experiments clarified. *Atmos. Res.*, **39**, 263–273.

Brooks, I. M., C. P. R. Saunders, R. P. Mitzeva, and S. L. Peck, 1997: The effect on thunderstorm charging of the rate of rime accretion by graupel. *Atmos. Res.*, **43**, 277–295.

Browning, K. A., 1964: Airflow and precipitation trajectories within severe local storms which travel to the right of the winds. *J. Atmos. Sci.*, **21**, 634–639.

Bruning, E. C., 2008: *Charging regions, regions of charge, and storm structure in a partially inverted supercell thunderstorm.* Ph.D. thesis, University of Oklahoma, Norman, OK.

Bruning, E. C., W. D. Rust, T. J. Schuur, D. R. MacGorman, P. R. Krehbiel, and W. Rison, 2007: Electrical and polarimetric radar observations of a multicell storm in TELEX. *Mon. Wea. Rev.*, **135**, 2525–2544.

Bryan, G. H., 2005: Spurious convective organization in simulated squall lines owing to moist absolutely unstable layers. *Mon. Wea. Rev.*, **133**, 1978–1997.

Burgess, D. W. and L. R. Lemon, 1976: Chapter 5, union city storm history. *The Union City, Oklahoma Tornado of 24 May 1973*, R. A. Brown, ed., NOAA Tech. Memo, ERL NSSL-80, 33–51.

Byrne, G. J., A. A. Few, and M. F. Stewart, 1989: Electric field measurements within a severe thunderstorm anvil. *J. Geophys. Res.*, **94**, 6297–6307.

Carey, L. D., W. A. Peterson, and S. A. Rutledge, 2003a: Evolution of cloud-to-ground lightning and storm structure in the Spencer, South Dakota, tornadic supercell of 30 May 1998. *Mon. Wea. Rev.*, **131**, 1811–1831.

Carey, L. D. and S. A. Rutledge, 1996: A multiparameter radar case study of the microphysical and kinematic evolution of a lightning producing storm. *J. Meteor. and Atmos. Phys.*, **59**, 33–64.

Carey, L. D., S. A. Rutledge, and W. A. Peterson, 2003b: The relationship between severe storm reports and cloud-to-ground lightning polarity in the contiguous United States from 1989 to 1998. *Mon. Wea. Rev.*, **131**, 1211–1228.

Coniglio, M. C., D. J. Stensrud, and L. J. Wicker, 2006: Effects of upper-level shear on the structure and maintenance of strong quasi-linear mesoscale convective systems. *J. Atmos. Sci.*, **63**, 1231–1252.

Cummins, K., M. Murph, E. Bardo, W. Hiscox, R. Pyle, and A. Pifer, 1998: A combined TOA/MDF technology upgrade of the U.S. National Lightning Detection Network. *J. Geophys. Res.*, **103**, 9035–9044.

Curran, E. B. and W. D. Rust, 1992: Positive ground flashes produced by low-precipitation thunderstorms in Oklahoma on 26 April 1984. *Mon. Wea. Rev.*, **120**, 544–553.

Deierling, W., J. Latham, W. A. Petersen, S. M. Ellis, and H. J. Christian, 2005: On the relationship of thunderstorm ice hydrometeor characteristics and total lightning measturements. *Atmos. Res.*, **76**, 114–126.

Doswell, C. A., III and D. W. Burgess, 1993: Tornadoes and tornadic storms: A review of conceptual models. *The Tornado: Its Structure, Dynamics, Prediction, and Hazards. Geophys. Monogr.*, Amer. Geophys. Union, 161–172.

Dotzek, N., R. M. Rabinb, L. D. Carey, D. R. MacGorman, T. L. McCormick, N. W. Demetriades, M. J. Murphy, and R. L. Holle, 2005: Lightning activity related to satellite and radar observations of a mesoscale convective system over Texas on 78 April 2002. *Atmos. Res.*, **76**, 127–166.

Dowell, D. C. and H. B. Bluestein, 1997: The Arcadia, Oklahoma, storm of 17 May 1981: Analysis of a supercell during tornadogenesis. *Mon. Wea. Rev.*, **125**, 2562–2582.

Dowell, D. C. and L. J. Wicker, 2009: Additive noise for storm-scale ensemble data assimilation. *J. Atmos. Oceanic Tech.*, **26**, 911–927.

Dowell, D. C., F. Zhang, L. J. Wicker, C. Synder, and N. A. Crook, 2004: Wind and temperature retrievals in the 17 May 1981 Arcadia, Oklahoma, supercell: Ensemble Kalman filter experiments. *Mon. Wea. Rev.*, **132**, 1982–2005.

Dwyer, J. R., 2003: A fundamental limit on electric fields in air. *Geophys. Res. Lett.*, **30**, doi:10.1029/2003GL017781.

Dye, J. E., M. G. Bateman, H. J. Christian, E. Defer, C. A. Grainger, W. D. Hall, E. P. Krider, S. A. Lewis, D. M. Mach, F. J. Merceret, J. C. Willett, and P. T. Willis, 2007: Electric fields, cloud microphysics, and reflectivity in anvils of Florida thunderstorms. *J. Geophys. Res.*, **112**, doi:10.1029/2006JD007550.

Dye, J. E. and J. C. Willett, 2007: Observed enhancement of reflectivity and the electric field in long-lived florida anvils. *Mon. Wea. Rev.*, **135**, 3362–3380.

Emanuel, K. A., 1994: *Atmospheric Convection.* Oxford University Press, 580 pp.

Finley, C. A., W. R. Cotton, and R. A. Pielke, Sr., 2001: Numerical simulation of tornadogenesis in a high-precipitation supercell. Part I: Storm evolution and transition into a bow echo. *J. Atmos. Sci.*, **58**, 1597–1629.

Gish, O. H., 1944: Evaluation and interpretation of the columnar resistance of the atmosphere. *Terr. Magn. Atmos. Electr.*, **49**, 159–168.

Goodman, S. J., R. Blakeslee, H. Christian, W. Koshak, J. Bailey, J. Hall, E. McCaul, D. Buechler, C. Darden, J. Burks, T. Bradshaw, and P. Gatlin, 2005: The north Alabama lightning mapping array: Recent severe storm observations and future prospects. *Atmos. Res.*, **76**, 423–437.

Hamlin, T. D., 2004: *The New Mexico Tech Lightning Mapping Array*. Ph.D. thesis, New Mexico Institute of Mining and Technology, Socorro, NM.

Helsdon, J. H., Jr. and R. D. Farley, 1987: A numerical modeling study of a montana thunderstorm: 2. model results versus observations involving electrical aspects. *J. Geophys. Res.*, **92**, 5661–5675.

Heymsfield, A. J., 1986: Ice particle evolution in the anvil of a severe thunderstorm during CCOPE. *J. Atmos. Sci.*, **43**, 2463–2478.

Jacobson, E. A. and E. P. Krider, 1976: Electrostatic field changes produced by Florida lightning. *J. Atmos. Sci.*, **33**, 103–117.

Johnson, E. V. and E. R. Mansell, 2006: Three-dimensional lightning mapping of the central Oklahoma supercell on 26 May 2004. *Preprints, 2nd Conf. on Meteor. Appl. of Lightning Data*, Amer. Meteor. Soc., Atlanta, GA.

Kasemir, H., 1960: A contribution to the electrostatic theory of a lightning discharge. *J. Geophys. Res.*, **65**, 1873–1878.

Kessinger, C. J., P. S. Ray, and C. E. Hane, 1987: The Oklahoma squall line of 19 May 1977. Part I: A multiple Doppler analysis of convective and stratiform structure. *jas*, **44**, 2840–2864.

Klemp, J. B., 1987: Dynamics of tornadic thunderstorms. *Annu. Rev. Fluid Mech.*, **19**, 369–402.

Klemp, J. B. and R. B. Wilhelmson, 1978: Simulations of right- and left-moving storms produced through storm splitting. *J. Atmos. Sci.*, **35**, 1097–1110.

Koch, S. E., M. desJardins, and P. J. Kocin, 1983: An interactive Barnes objective map analysis scheme for use with satellite and conventional data. *J. Climate Appl. Meteor.*, **130**, 1487–1503.

Krehbiel, P. R., J. A. Riousset, V. P. Pasko, R. J. Thomas, W. Rison, M. A. Stanley, and H. E. Edens, 2008: Upward electrical discharges from thunderstorms. *Nature Geosci.*, **1**, 233–237.

Krehbiel, P. R., R. J. Thomas, W. Rison, T. Hamlin, J. Harlin, and M. Davis, 2000: GPS-based mapping system reveals lightning inside storms. *Eos, Trans. Amer. Geophys. Union*, **81**, 21–32.

Kuhlman, K. M., D. R. MacGorman, M. I. Biggerstaff, W. D. Rust, T. J. Schuur, C. L. Ziegler, and P. Krehbiel, 2006a: Lightning and radar observations of the 29 May 2004 tornadic HP supercell during TELEX. *Preprints, 2nd Conf. on Meteorological Applications of Lightning Data*, Amer. Meteor. Soc., Atlanta, GA.

Kuhlman, K. M., C. L. Zielger, E. R. Mansell, D. R. MacGorman, and J. M. Straka, 2006b: Numerically simulated electrification and lightning of the 29 June 2000 STEPS supercell storm. *Mon. Wea. Rev.*, **134**, 2734–2757.

Lang, T. J., L. J. Miller, M. Weisman, S. A. Rutledge, L. J. Barker, V. N. Bringi, V. Chandrasekar, A. Detwiler, N. Doesken, J. Helsdon, C. Knight, P. Krehbiel, W. A. Lyons, D. R. MacGorman, E. Rasmussen, W. Rison, W. D. Rust, and R. J. Thomas, 2004: The severe thunderstorm electrification and precipitation study. *Bull. Amer. Meteor. Soc.*, 1107–1125.

Lemon, L. R., 2009: Supercell collapse. *34th Conf. on Radar Meteor.*, Amer. Meteor. Soc., Williamsburg, VA.

Lemon, L. R. and C. A. Doswell, III, 1979: Severe thunderstom evolution and mesocyclone structure as related to tornadogenesis. *Mon. Wea. Rev.*, **107**, 1184–1197.

Loney, M. L., D. S. Zrnic, J. M. Straka, and A. V. Ryzhkov, 2002: Enhanced polarimetric radar signatures above the melting level in a supercell storm. *J. Appl. Meteor.*, **41**, 1179–1194.

Lund, N., 2008: *Relationships between lightning location and polarimetric radar signatures in a small mesoscale convective system*. Master's thesis, University of Oklahoma, Norman, OK.

MacGorman, D., J. M. Straka, and C. L. Ziegler, 2001: A lightning parameterization for numerical cloud models. *J. Appl. Meteor.*, **40**, 459–478.

MacGorman, D. R., 1993: Lightning in tornadic storms: A review. *The Tornado: Its Structure, Dynamics, Prediction, and Hazards, Geophys. Monogr.*, Amer. Geophys. Union, volume 79, 173–182.

MacGorman, D. R. and D. W. Burgess, 1994: Positive cloud-to-ground lightning in tornadic storms and hailstorms. *Mon. Wea. Rev.*, **122**, 1671–1697.

MacGorman, D. R., D. W. Burgess, V. Mazur, W. D. Rust, W. L. Taylor, and B. C. Johnson, 1989: Lightning rates relative to tornadic storm evolution on 22 May 1981. *J. Atmos. Sci.*, **46**, 221–250.

MacGorman, D. R., A. A. Few, and T. L. Teer, 1981: Layered lightning activity. *J. Geophys. Res.*, **86**, 9900–9910.

MacGorman, D. R., K. M. Kuhlman, E. C. Bruning, W. D. Rust, P. R. Krehbiel, and M. I. Biggerstaff, 2008a: Small, continual lightning activity in the overshooting turret of supercell storms. *3rd Conf. on Meteor. App. of Lightning Data*, Amer. Meteor. Soc., New Orleans, LA.

MacGorman, D. R. and K. E. Nielsen, 1991: Cloud-to-ground lightning in a tornadic storm on 8 May 1986. *Mon. Wea. Rev.*, **119**, 1557–1574.

MacGorman, D. R. and W. D. Rust, 1998: *The electrical nature of storms*. Oxford University Press, 422 pp.

MacGorman, D. R., W. D. Rust, P. R. Krehbiel, E. C. Bruning, and K. C. Wiens, 2005: The electrical structure of two supercell storms during STEPS. *Mon. Wea. Rev.*, **133**, 2583–2607.

MacGorman, D. R., W. D. Rust, T. Schuur, M. E. Biggerstaff, J. Straka, C. L. Ziegler, E. R. Mansell, , E. C. Bruning, K. M. Kuhlman, N. Lund, J. Helsdon, L. Carrey, K. Eack, W. H. Beasley, P. R. Krehbiel, and W. Rison, 2008b: TELEX: The thunderstorm electrification and lightning experiment. *Bull. Amer. Meteor. Soc.*, **89**, 9971013.

MacGorman, D. R., W. L. Taylor, and A. A. Few, 1983: Some spatial and temporal relationships between lighting and storm structure and evolution. *FAA 8th Intern. Aero. and Ground Conf. on Lightning Static Elec*, Fed. Aviat. Admin., United States, 7pp.

Maier, L., C. Lennon, T. Britt, and S. Schaefer, 1995: Ldar system performance and analysis,. *Intl. Conf. on Cloud Physics*, Amer. Meteor. Soc., Dallas, TX.

Majcen, M., P. Markowski, Y. Richardson, D. Dowell, and J. Wurman, 2008: Multipass objective analyses of doppler radar data. *J. Atmos. Oceanic Technol.*, **25**, 1845–1858.

Mansell, E. R., 2000: *Electrification and lightning in simulated supercell and nonsupercell thunderstorms*. Ph.D. thesis, University of Oklahoma, Norman, OK.

Mansell, E. R., D. R. MacGorman, J. M. Straka, and C. L. Ziegler, 2003: Recent results from thunderstorm electrification modeling. *Proceedings, 12th Int. Conf. on Atmospheric Electricity*, ICAE, Versailles, France, 119–122.

Mansell, E. R., D. R. MacGorman, C. L. Ziegler, and J. M. Straka, 2002: Simulated three-dimensional branched lightning in a numerical thunderstorm model. *J. Geophys. Res.*, **107**, 2–1.

— 2005: Charge structure and lightning sensitivity in a simulated multicell thunderstorm. *J. Geophys. Res.*, **110**.

Mansell, E. R., C. L. Ziegler, and E. C. Bruning, 2010: Simulated electrification of a small thunderstorm with two-moment bulk microphysics. *J. Atmos. Sci.*, **67**.

Marshall, T. C., M. P. McCarthy, and W. D. Rust, 1995: Electric field magnitudes and lightning initiation in thunderstorms. *J. Geophys. Res.*, **100**, 7097–7103.

Marshall, T. C., W. D. Rust, W. P. Winn, and K. E. Gilbert, 1989: Electrical structure in two thunderstorm anvil clouds. *J. Geophys. Res.*, **94**, 2171–2181.

Marshall, T. C., M. Stolzenburg, C. R. Maggio, L. M. Coleman, W. Rison, P. R. Krehbiel, T. Hamlin, R. J. Thomas, and W. Rison, 2005: Observed electric fields associated with lightning initiation. *Geophys. Res. Lett.*, 2004GL021802.

Mason, B. J., 1988: Ther generation of electric charges and fields in thunderstorms. *Proc. R. Soc. London, Ser. A*, **415**, 303–315.

Mazur, V. and L. Ruhnke, 1993: Common physical processes in natural and artificially triggered lightning. *J. Geophys. Res.*, **98**, 913–930.

McCarthy, M. P. and G. K. Parks, 1992: On the modulation of X ray fluxes in thunderstorms. *J. Geophys. Res.*, **97**, 5857–5864.

McCaul, E. W., Jr., D. E. Buechler, S. Hodanish, and S. J. Goodman, 2002: The Almena, Kansas, tornadic storm of 3 June 1999: A long-lived supercell with very little cloud-to-ground lightning. *Mon. Wea. Rev.*, **130**, 407–415.

Milbrandt, J. A. and M. K. Yau, 2005: A multimoment bulk microphysics parameterization. Part II: A proposed three-moment closure and scheme description. *J. Atmos. Sci.*, **62**, 3065–3081.

Mitzeva, R., C. Saunders, and B. Tsenova, 2006: Parameterisation of non-inductive charging in thunderstorm regions free of cloud droplets. *Atmos. Res.*, **82**, 102–111.

Moller, A. R., C. A. Doswell, III, M. P. Foster, and G. R. Woodall, 1994: The operational recognition of supercell thunderstorm environments and storm structures. *Wea. Forecasting*, **9**, 327–347.

Murphy, M. J., 2006: When flash algorithms go bad. *Proceedings, 19th Int. Lightning Detection Conf. and 1st Int. Lightning Meteorlogy Conf.*, Vaisala Inc., Tucson, AZ, 6 pp.

Musil, D. J., A. J. Heymsfield, and P. L. Smith, 1986: Microphysical characteristics of a well-developed weak echo region in a high plains supercell thunderstorm. *J. Climate Appl. Meteor.*, **25**, 1037–1051.

Oye, R., C. Mueller, and S. Smith, 1995: Software for the radar translation, visualization, editing and interpolation. *Preprints, 27th Conf. on Radar Meteor.*, Amer. Meteor. Soc., Vail, CO, 359–361.

Pereyra, R. G., E. E. Avila, N. E. Castellano, and C. Saunders, 2000: A laboratory study of graupel charging. *J. Geophys. Res.*, **105**, 20803–20812.

Perez, A. H., L. J. Wicker, and R. E. Orville, 1997: Characteristics of cloud-to-ground lightning associated with violent tornadoes. *Wea. Forecasting*, **12**, 428–437.

Proctor, D. E., 1991: Regions where lightning flashes began. *J. Geophys. Res.*, **96**, 5099–5112.

Rasmussen, E. N. and J. M. Straka, 1998: Variations in supercell morphology. Part I: Observations of the role of upper-level storm-relative flow. *Mon. Wea. Rev.*, **126**, 2406–2421.

Ray, P. S., R. J. Doviak, G. B. Walker, D. Sirmans, J. Carter, and W. Bumgarner, 1975: Dual-Doppler observation of a tornadic storm. *J. Appl. Meteor.*, **14**, 1521–1530.

Ray, P. S., D. R. MacGorman, W. D. Rust, W. L. Taylor, and L. W. Rasmussen, 1987: Lightning location relative to storm structure in a supercell storm and a multicell storm. *J. Geophys. Res.*, **92**, 5713–5724.

Ray, P. S., C. L. Ziegler, and W. Bumgarner, 1980: Single- and multiple-Doppler radar observations of tornadic storms. *Mon. Wea. Rev.*, **108**, 1607–1625.

Riousset, J. A., V. P. Pasko, P. R. Krehbiel, R. J. Thomas, and W. Rison, 2007: Three-dimensional fractal modeling of intracloud lightning discharge in a New Mexico thunderstorm and comparison with lightning mapping observations. *J. Geophys. Res.*, **112**, doi:10.1029/2006JD007621.

Rison, W., R. J. Thomas, P. R. Krehbiel, T. Hamlin, and J. Harlin, 1999: A GPS-based three-dimensional lightning mapping system: Initial observations in central New Mexico. *Geophys. Res. Lett.*, **26**, 3373–3576.

Rust, W. D. and D. R. MacGorman, 2002: Possibly inverted-polarity electrical structures in thunderstorms during STEPS. *Geophys. Res. Lett.*, **29**, 12–1.

Rust, W. D., D. R. MacGorman, and R. T. Arnold, 1981: Positive cloud-to-ground lightning flashes in severe storms. *Geophys. Res. Lett.*, **8**, 791–794.

Rust, W. D., D. R. MacGorman, E. C. Bruning, S. A. Weiss, P. R. Krehbiel, R. J. Thomas, W. Rison, T. Hamlin, and J. Harlin, 2005: Inverted-polarity electrical structures in thunderstorms in the Severe Thunderstorm Electrification and Precipitation Study (STEPS). *Atmos. Res.*, **76**, 247–271.

Rust, W. D. and T. C. Marshall, 1996: On abandoning the thunderstorm tripole-charge paradigm. *J. Geophys. Res.*, **101**, 23499–23504.

Saunders, C. P. R., 1993: A review of thunderstorm electrification processes. *J. Appl. Meteor.*, **32**, 642–654.

Saunders, C. P. R., H. Bax-Norman, C. Emerisic, E. E. Avila, and N. E. Castellano, 2006: Laboratory studies of the effect of cloud conditions on graupel/crystal charge transfer in thunderstorm electrification. *Quart. J. Roy. Meteor. Soc.*, **132**, 2653–2673.

Saunders, C. P. R. and S. L. Peck, 1998: Laboratory studies of the influence of the rime accretion rate on charge transfer during crystal/graupel collisions. *J. Geophys. Res.*, **103**, 13949–13956.

Schuur, T. J. and S. A. Rutledge, 2000: Electrification of stratiform regions in mesoscale convective systems. Part I: An observational comparison of symmetric and asymmetric MCSs. *J. Atmos. Sci.*, **57**, 1961–1982.

Shafer, M. A., D. R. MacGorman, and F. H. Carr, 2000: Cloud-to-ground lightning throughout the lifetime of a severe storm system in Oklahoma. *Mon. Wea. Rev.*, **128**, 1798–1816.

Shao, X. M. and P. R. Krehbiel, 1996: The spatial and temporal development of intracloud lightning. *J. Geophys. Res.*, **101**, 26641–26668.

Smith, S. B., J. G. LaDue, and D. R. MacGorman, 2000: The relationship between cloud-to-ground lightning polarity and surface equivalent potential temperature during three tornadic outbreaks. *Mon. Wea. Rev.*, **128**, 3320–3328.

Snyder, C. and F. Zhang, 2003: Assimilation of simulated Doppler radar observations with an ensemble Kalman filter. *Mon. Wea. Rev.*, **131**, 1663–1677.

Solomon, R. and M. Baker, 1998: Lightning flash rate and type in convective storms. *J. Geophys. Res.*, **103**, 14041–14057.

Steiger, S. M., R. E. Orville, and L. D. Carey, 2007: Total lightning signatures of thunderstorm intensity, Part 1: Supercells. *Mon. Wea. Rev.*, **135**, 3281–3302.

Stolzenburg, M. and T. C. Marshall, 2008: Charge structure and dynamics in thunderstorms. *Space Sci. Rev.*, **137**, 355–372.

Stolzenburg, M., T. C. Marshall, W. D. Rust, and B. F. Smull, 1994: Horizontal distribution of electrical and meteorological conditions across the stratiform region of a mesoscale convective system. *Mon. Wea. Rev.*, **122**, 1777–1797.

Stolzenburg, M., W. D. Rust, and T. C. Marshall, 1998: Electrical structure in thunderstorm convective regions 3. Synthesis. *J. Geophys. Res.*, **103**, 14097–14108.

Straka, J. M. and E. R. Mansell, 2005: A bulk microphysics parameterization with multiple ice precipitation categories. *J. Appl. Meteor.*, **44**, 445–466.

Sun, J. and N. A. Crook, 1998: Dynamical and microphysical retrieval from Doppler radar observations using a cloud model and its adjoint. Part II: Retrieval experiments of an observed Florida convective storm. *J. Atmos. Sci.*, **55**, 835–852.

Takahashi, T., 1978: Riming electrification as a charge generation mechanism in thunderstorms. *J. Atmos. Sci.*, **35**, 1536–1548.

Takahashi, T. and K. Miyawaki, 2002: Reexamination of riming electrification in a wind tunnel. *J. Atmos. Sci.*, **59**, 10181025.

Tan, Y., S. Tao, and B. Zhu, 2006: Fine-resolution simulation of the channel structures and propagation features of intracloud lightning. *Geophys. Res. Lett.*, **33**, doi:10.1029/2005GL025523.

Taylor, W. L., E. A. Brandes, W. D. Rust, and D. R. MacGorman, 1984: Lightning activity and severe storm structure. *Geophys. Res. Lett.*, **11**, 545548.

Tessendorf, S. A., S. A. Rutledge, and K. C. Wiens, 2007a: Radar and lightning observations of normal and inverted polarity multicellular storms from STEPS. *Mon. Wea. Rev.*, **135**, 3682–3706.

— 2007b: Radar and lightning observations of the 3 June 2000 electrically inverted storms from STEPS. *Mon. Wea. Rev.*, **135**, 3665–3691.

Thomas, R., P. Krehbiel, W. Rison, J. Harlin, T. Hamlin, and N. Campbell, 2003: The LMA flash algorithm. *Proceedings, 12th International Conference on Atmospheric Electricity*, Inter. Commis. Atmos. Elec., Versailles, France, 3 pp.

Thomas, R., P. Krehbiel, W. Rison, S. Hunyady, W. Winn, T. Hamlin, and J. Harlin, 2004: Accuracy of the lightning mapping array. *J. Geophys. Res.*, **109**, doi:10.1029/2004JD004549.

Trapp, R. J. and C. A. Doswell, III, 2000: Radar data objective analysis. *J. Atmos. Ocean. Technol.*, **17**, 105–120.

Weiss, S. A., W. D. Rust, D. R. MacGorman, E. C. Bruning, and P. R. Krehbiel, 2008: Evoloving complex electrical structures of the STEPS 25 June 2000 multicell storm. *Mon. Wea. Rev.*, **136**, 741–756.

Whitaker, J. S. and T. M. Hamill, 2002: Ensemble data assimilation without perturbed observations. *Mon. Wea. Rev.*, **130**, 1913–1924.

Wicker, L. J. and W. C. Skamarock, 2002: Time-splitting methods for elastic models using forward time schemes. *Mon. Wea. Rev.*, **130**, 2088–2097.

Wiens, K. C., S. A. Rutledge, and S. A. Tessendorf, 2005: The 29 June 2000 supercell observed during STEPS. Part 2: Lightning and charge structure. *J. Atmos. Sci.*, **62**, 4151–4177.

Williams, E. R., 1985: Electrical discharge propagation in and around space charge clouds. *J. Geophys. Res.*, **90**, 6059–6070.

— 2001: The electrification of severe storms, Severe Convective Storms. *Meteor. Monogr.*, C. A. Doswell, III, ed., Amer. Meteor. Soc., volume 50, 527–561.

Williams, E. R., V. Mushtak, D. Rosenfeld, S. Goodman, and D. Boccippio, 2005: Thermodynamic conditions favorable to superlative thunderstorm updraft, mixed phase microphysics and lightning flash rate. *Atmos. Res.*, **76**, 288–306.

Williams, E. R., M. E. Weber, and R. E. Orville, 1989: The relationship between lightning type and convective state of thunderclouds. *J. Geophys. Res.*, **94**, 213–220.

Winn, W. P. and L. G. Byerley, III, 1975: Electric field growth in thunderclouds. *Quart. J. Roy. Meteor. Soc.*, **101**, 979–994.

Wurman, J., Y. Richardson, C. Alexander, S. Weygandt, and P. F. Zhang, 2007: Dual-Doppler and single-Doppler analysis of a tornadic storm undergoing mergers and repeated tornadogenesis. *Mon. Wea. Rev.*, **135**, 736–758.

Zhang, Y., Q. Meng, P. R. Krehbiel, X. Liu, and X. Zhou, 2004: Spatial and temporal characteristics of VHF radiation source produced by lightning in supercell thunderstorms. *Chinese Science Bull.*, **49**, 624–631.

Ziegler, C. L., 1985: Retrieval of thermal and microphysical variables in observed convective storms. Part I: Model development and preliminary testing. *J. Atmos. Sci.*, **42**, 1487–1509.

Ziegler, C. L., D. R. MacGorman, J. E. Dye, and P. S. Ray, 1991: A model evaluation of non-inductive graupel-ice charging in the early electrification of a mountain thunderstorm. *J. Geophys. Res.*, **96**, 12833–12855.

Appendix A

Acronyms

Table A.1: Acronyms used in this Dissertation

Acronym	Term
AGL	Above Ground Level
AMS	American Meteorological Society
BWER	Bounded Weak Echo Region
CAPE	Convective Available Potential Energy
CCN	Cloud Condensation Nuclei
CEDRIC	Custom Editing and Display of Reduced Information in Cartesian Space (software)
CG	Cloud-to-Ground (Lightning)
CIMMS	Cooperative Institute for Mesoscale Meteorological Studies
COMMAS	Collaborative Model for Multiscale Atmospheric Simulation

Continued on next page

Acronym	Term
dBZ	Decibel scale for the Reflectivity Field
DD	Dual-Doppler
EFM	Electric Field Meter
EnKF	Ensemble Kalman Filter
EnSRF	Ensemble Square Root Filter
FFD	Forward Flank Downdraft
GPS	Global Positioning System
IC	In-Cloud (Lightning)
HP	High Precipitation (Supercell)
$J\,kg^{-1}$	Joules per Kilogram
LDAR	Lightning Detection and Ranging
LCL	Lifted Condensation Level
LMA	Lightning Mapping Array
LP	Low Precipitation (Supercell)
LWC	Liquid Water Content
mb	Millibars
MSL	Mean Sea Level
NASA	National Aeronautics and Space Administration
NLDN	National Lightning Detection Network
NOAA	National Oceanic and Atmospheric Administration

Continued on next page

Acronym	Term
NSSL	National Severe Storms Laboratory
NWS	National Weather Service
OKLMA	Oklahoma Lightning Mapping Array
RAR	Rime Accretion Rate
REORDER	Software for coordinate translation of radar data from radar space to cartesian grids
RFD	Rear Flank Downdraft
SMART-R	Shared Mobile Atmospheric Research and Teaching - Radar
SOLO	Software for display and editing of radar data
SP98	Results from Saunders and Peck (1998)
SPC	Storm Prediction Center
SR1, SR2	SMART-R mobile radars
STEPS	Severe Thunderstorm Electrication and Precipitation Study
TELEX	Thunderstorm Electrification and Lightning Experiment
UTC	Coordinated Universal Time
VHF	Very High Frequency
WSR-88D	Weather Surveillance Radar-1988 Doppler